In Situ X-Ray Photoelectron Spectroscopy of Ionic Liquids at Polarized Metal Electrodes

In Situ Röntgenphotoelektronenspektroskopie

von Ionischen Flüssigkeiten

an Polarisierten Metallelektroden

Der Naturwissenschaftlichen Fakultät der

Friedrich-Alexander-Universität Erlangen-Nürnberg

zur Erlangung des Doktorgrades

Dr. rer. nat.

vorgelegt von

Francesco Greco

aus Pinerolo

Table of Contents

1. Introduction

Climate change induced by the combination of fossil fuels utilization and greenhouse gases emission highlights the need to switch from conventional energy production to renewable and more sustainable sources. As "green" sources, solar and wind plants are becoming extremely popular, but their intermittent energy outputs rely on the time of the day and local weather conditions. This emphasizes the need for a compelling development of more efficient energy storage devices. Among various technologies used to store energy, electrochemical energy storage (EES) devices, such as supercapacitors and batteries, provide long cycle life, low maintenance and pollution free operations.[1]

Amid EESs devices, supercapacitors can store energy by charge accumulation at the electrode/electrolyte interface forming an electrical double layer (EDL) of charges, in which the storing mechanism is dominated by electrostatic interactions. Supercapacitors offer energy in short times (up to few seconds), fast discharge/charge rates and long cycles lifetime.[2] Although supercapacitors provide high power densities, they are not comparable to batteries in terms of energy densities and therefore improving this parameter would provide a broader range of application of such devices. The energy density in a supercapacitor is proportional to the capacitance of the cell multiplied by the square of the operative potential; thus, expanding the capacitance and the operative potential window of the device can provide higher energy densities. Given that the capacitance is directly proportional to the area of the electrode, a viable route to increase the capacitance is to use carbonaceous materials characterized by high surface area.[3, 4] Furthermore, the operative potential at which a supercapacitor can be used is generally limited by electro-decomposition; therefore, using solvents or electrolytes with high electrochemical stability allows for operations at higher voltages. In this regard, organic electrolyte-based supercapacitors are broadly used due to their larger operative potential window (2.5-2.7 V) in comparison with aqueous electrolytes (1.0-1.3 V). However, organic electrolytes have some drawbacks such as toxicity flammability and volatility.[5]

A large class of compounds to which interest is growing is ionic liquids (ILs). These molten salts offer a broad range of properties that can be tuned through the almost countless combination of different cations and anions. Furthermore, often low flammability, low melt-

ing points, negligible vapor pressure and large operative potential window (3.5-4.0 V) make them suitable candidates to overcome few of the challenges related to EES.

In order to optimize the applicability of ILs in EES, it is of primary importance to study the physicochemical properties of such systems with a specific focus on the nature of their interfaces at charged electrodes. Although there is already a well-established knowledge of the liquid/electrode interface for inorganic aqueous electrolyte, it cannot be used for ILs. The complications arise from the fact that ILs do not have a solvent, they are highly concentrated ionic media, and the properties of the constituting ions are often different as compared to inorganic cations and anions in conventional electrolytes, in terms of asymmetric shapes of the IL ions or different size of cation and anion. For instance, the high ionic density of ILs results in unique features of the differential capacitance (C_d) curves in impedance spectroscopy measurements such as the bell or camel shape.[6-10] These distinctive features of the C_d curves of ILs cannot be simply described with the classical models adopted for aqueous electrolytes, such as the Helmholtz or Gouy-Chapman-Stern models. In this regard, a successful interpretation was given by Kornyshev[11] through a modified mean-field theory approach (an overview of these models is given in Chapter 2.1). Moreover, the different sizes and shapes of the counterions lead to an asymmetric shape of the C_d curves, which has been studied by impedance measurements, molecular dynamic simulations, and mean-field calculations.[6, 12, 13] Other characteristic features, such as strong interfacial layering, including oscillation of the ion concentrations and overscreening of the charged layers, have been found by atomic force microscopy[14-17] and X-ray reflectivity experiments[18] of IL/electrode interfaces and also by computational studies.[19-21]

Due to the novelty and very specific characteristics of ILs at electrified interfaces, the aim of this thesis is to provide a new approach to study the interfacial properties of such systems under the well-defined conditions of ultra-high vacuum (UHV) with X-ray photoelectron spectroscopy (XPS). XPS has been increasingly used to study surface/interface-related phenomena in ILs, which is possible due to their negligible vapor pressure.[22, 23] With variable depth information in the nm range, angle-resolved XPS has been successfully utilized to characterize solid/liquid and liquid/vacuum interfaces including chemical reactions within these interface regions.[24-29] In this thesis, it will be demonstrated that monitoring the binding energy shifts (ΔBE) at the IL/vacuum interface with XPS provides information on the potential screening (PS) at the IL/electrode interface. While the relation between ΔBE and PS is discussed in Chapter 2.1.1, in Chapter 3 it is demonstrated that PS measurements can be indeed used to obtain infor-

mation on the interfaces of various neat ILs and metal electrodes. In such measurements, the shape of the PS curves obtained following the *ΔBE* at the IL/vacuum interface for various applied voltages is characteristic for the combination of electrode and ions of the ILs. These different PS behaviors are attributed to the nature of the interactions at the IL/electrode interface. For instance, PS curves of imidazolium-based ILs on Pt electrodes are characterized by strong interactions between the aromatic imidazolium ring and the *d* orbitals of the metal. While in the absence of specific ion/electrode interaction, such as on the more inert Au electrode, the shape of the PS curves is influenced by the size difference of the cations and anions of the ILs.

In the field of supercapacitors, mixing different ILs has been used to achieve high energy densities or large operative windows.[30, 31] Therefore, the characteristic shape of the PS curves of $[C_8C_1Im][Tf_2N]$ and $[C_8C_1Im]Cl$ on Pt and Au electrodes is used as a fingerprint to determine the nature of the IL/electrode interfaces of binary mixtures of those two ILs in Chapter 4. By comparing the fingerprint-type behavior of the PS curves of neat ILs with the PS curves of binary IL mixtures, a very pronounced enrichment of Cl^- anions at the IL mixture/Au interface even down to a 0.1 mol% content of $[C_8C_1Im]Cl$ is deduced while $[Tf_2N]^-$ anions enrich at the IL mixture/Pt interface down to 10 mol% $[C_8C_1Im][Tf_2N]$. These mixture studies demonstrate that even small concentrations of another IL can strongly influence the situation at charged IL interfaces.

The strong enrichments of minority components observed in binary mixtures of $[C_8C_1Im][Tf_2N]$ and $[C_8C_1Im]Cl$ on Pt and Au electrodes raise the question on the role of contaminations at the IL/electrode interface. When ILs are used under ambient conditions, they can take up contaminations from the surrounding atmosphere. Therefore, in Chapter 5, we investigate the influence of ambient conditions on the PS at the interfaces of Au and Pt electrodes with $[C_8C_1Im][Tf_2N]$ and $[C_8C_1Im]Cl$. This study is based on a proof-of-principle experiment, which demonstrates that in UHV, PS measurements performed by XPS provide the same results as measurements recorded using a very characteristic 3-electrode setup. Based on this result, PS measurements under ultraclean conditions by XPS are compared to PS measurements with a 3-electrode setup in N_2 and air. Ambient conditions can lead to a pronounced influence on the PS for both $[C_8C_1Im][Tf_2N]$ and $[C_8C_1Im]Cl$ on Pt electrodes, while for Au electrodes hardly any influence is observed. These results demonstrate that the effect of ambient contaminants at the interface depends on the joint interplay of electrode material, ions of the IL and contaminants, and PS measurements can be employed as a reliable tool to detect these interfacial alterations due to ambient conditions.

As mentioned above, one of the goals of EES IL-based devices is to expand their operative voltage window. In this framework, using two different electrode materials in an asymmetric cell showed that the stability of the electrolytes can be extended beyond their decomposition voltage limit.[32] The PS behavior of this so-called asymmetric cell is explored in Chapter 6 by following the *BE* shifts with *in-situ* XPS in UHV for various IL and Au/Pt electrodes.

2. Fundamentals and Techniques

2.1. The Electrode / Liquid Interface

Electrochemical phenomena take place at the interface of an electron conductor, the electrode, and an ion conductor, the electrolyte. According to the processes happening at the interface two distinct phenomena can be distinguished. The first is named as *faradaic* and it occurs when in response to an applied voltage an electron transfer takes place at the interface. According to the direction of the flow of electrons, the species in the electrolyte can be reduced or oxidized. Notably, the charge passing through the interface for 1 mole of electrons is equal to 96485.3 C, which is known as the Faraday constant.

The second type of phenomenon is called *non-faradaic* and it is characterized by the absence of electron transfer at the interface. In this case, charges rearrange at the interface in order to screen the excess charges by the formation of an electrical double layer (EDL). One of the most common ways to study the properties of the EDL is measuring the differential capacitance,

$$C_d = \frac{dQ}{d\varphi} \tag{1}$$

which is defined as the dependence of the surface charge (Q) on the electrode potential (φ). In the following C_d is used as a parameter to give an overview of the EDL.

The EDL was first described by **Helmholtz,** more than a century ago,[33, 34] as a simple plate dielectric capacitor in which the only interactions at the interface and in the electrolyte are of electrostatic nature. In this model, the metal is one plate of the capacitor; the second plate is given by the counter charged ions layering at the interface. The EDL is restricted to only one layer of the electrolyte at the interface, within this layer the entire potential drop takes place, which decays linearly with the distance from the plate (Figure 1). In this model C_d can be described as:

$$C_d = C_H = \frac{\varepsilon \varepsilon_0}{d} \tag{2}$$

where d is the distance between the plates (size of the ions), ε is the relative permittivity of the medium between the two plates, ε_0 is the permittivity of free space (vacuum). Since the distance between the plates (d) of the capacitor is given by the size of the counterions in the Helmholtz model, the capacitance itself is inversely proportional to the size of the counterions. In this model, C_d is independent on the applied potential, that is, C_d is independent of electrode polarization.
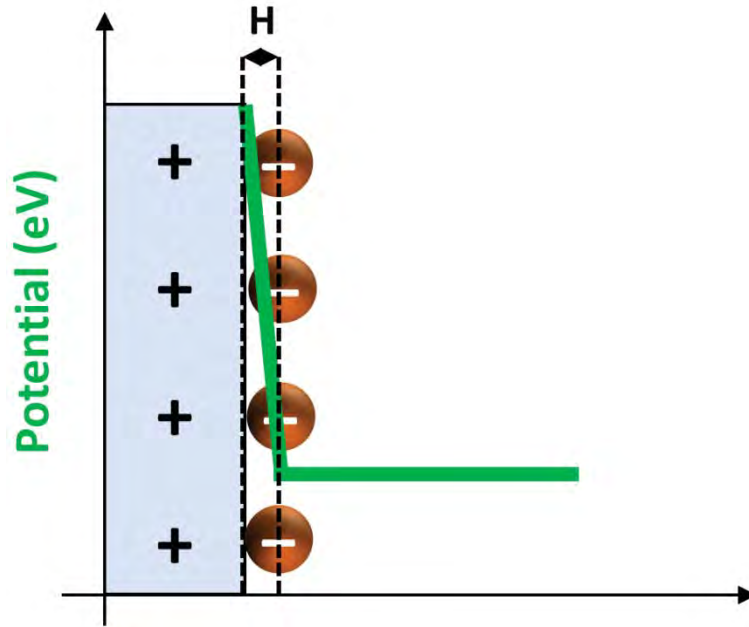
Figure 1 Schematic representation of the Helmholtz EDL model and the variation in potential according to the distance from the electrode.

In the **Gouy Chapman** model, the counterions are not forming a compact layer at the electrode;[35, 36] on the contrary, they are distributed over a large diffuse layer. The C_d in this model is given by the following equation:

$$C_d = C_{GC} = \frac{\varepsilon \varepsilon_0 A}{\lambda_D} \tag{3}$$

in which λ_D is the Debye length and gives the size of the diffuse layer following the Boltzmann statistics. The potential drop takes place within λ_D and decreases exponentially tending to a bulk solution value (Figure 2).
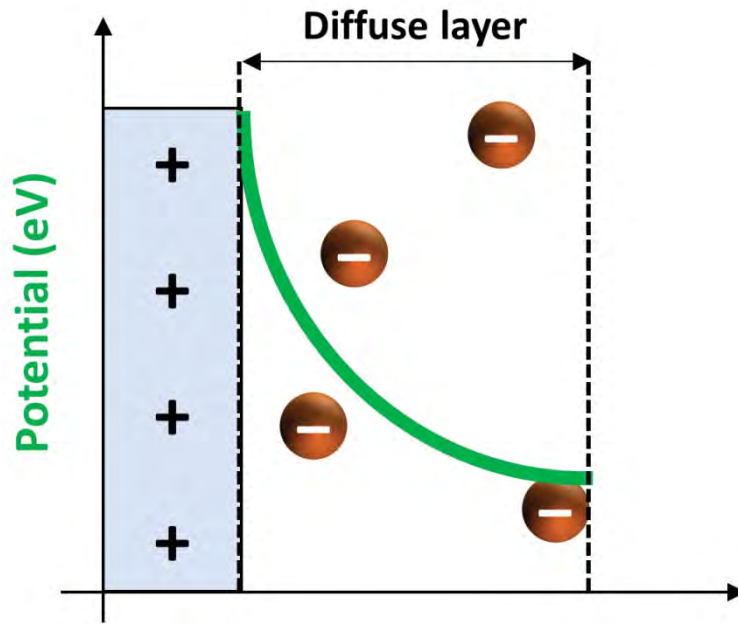
Figure 2 Schematic representation of the Gouy Chapman EDL model and the variation in potential according to the distance from the electrode.

In this model, C_d as a function of the voltage applied is described by a "U-shape" curve and is predicted to grow unlimitedly with increasing electrode polarization. The limitation of this model is the assumption that the charges are point charges which can approach the electrode surface arbitrarily close without any limitation. In reality, charges are stopped by approaching the surface at distances that correspond to their ionic radii, which means that for higher voltages applied, a second layer should be formed and C_d should decrease.

In order to overcome the limitation of considering point charges, **Stern** introduced in his model a compact layer at the solid-liquid interface, the analog of the Helmholtz model and a diffuse layer that is from the Gouy-Chapman model.[37] In this way, the EDL capacitance is given by the sum in series of the capacitance of this compact layer (C_H) and of the diffuse layer (C_{GC}).

$$\frac{1}{C_d} = \frac{1}{C_H} + \frac{1}{C_{GC}} \tag{4}$$

In such model, the potential drop goes down linearly within the compact layer and then it decays quasi-exponentially within the diffuse layer (Figure 3). However, the ions outside the Helmholtz layer are still treated as point charges which occupy no volume and therefore this model is still only accurate for low concentrations of ions or low potentials applied.
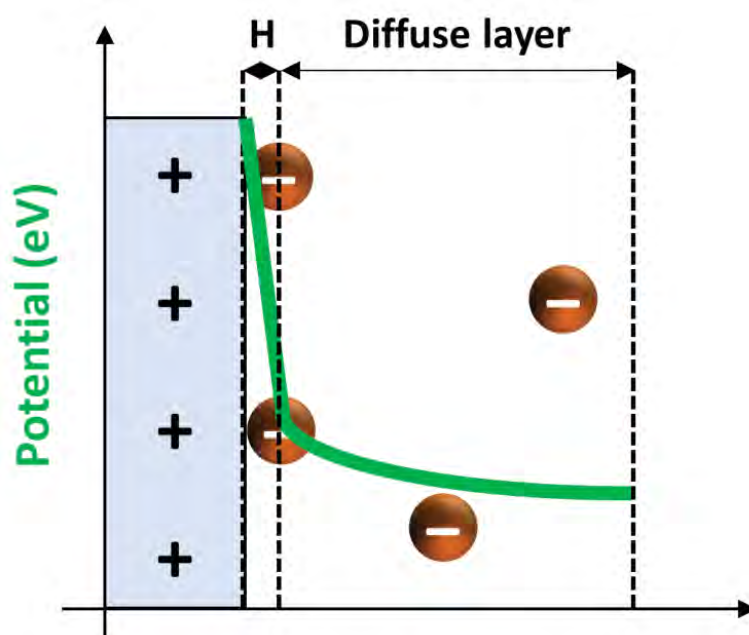
Figure 3 Schematic representation of the Gouy Chapman-Stern EDL model and the variation in potential according to the distance from the electrode.

In regard to high ionic concentrations, such as in ILs, an important breakthrough was made by **Kornishev**, who introduced in his model a mean field theory based on the Poisson-Boltzmann lattice gas model.[11] In this model, ions are not considered as point charges and they cannot layer at the interface unlimitedly but they will reach *lattice saturation*. This behavior is described through a lattice saturation parameter (γ) (Figure 4), which is expressed as the ratio between the total number of cations and anions in the bulk $\bar{N}$ and the total number of sites available for them N:

$$\gamma = \frac{\bar{N}}{N} \tag{5}$$

$\gamma = 1$ means that the ions are densely packed and the counterions will start to accumulate at the electrodes for increasing $U_{applied}$ values giving a thicker EDL and consequently decreasing C_d values ("bell shape" of C_d curve).

When γ is small, the ions are not densely packed, which gives some space to increase the density of counterions at the EDL with increasing $U_{applied}$. According to this situation, the C_d curves will have a "U shape" at low voltages (Figure 5a), while at higher voltages the electrode interface is saturated with counterions and C_d decreases, resulting in an overall "camel shape" of the C_d curves (Figure 5b).

γ = 1   γ < 1
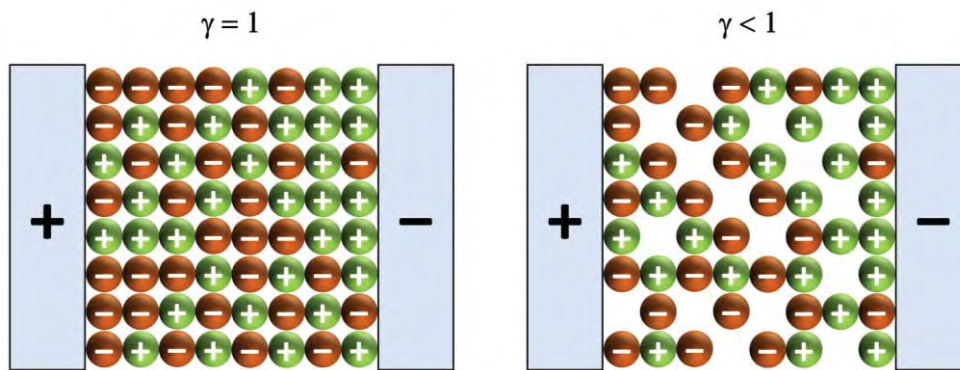
Figure 4 Schematic representation of the lattice saturation parameter for an IL between two polarized electrodes. (Adapted with permission from M. V. Fedorov, A. A. Kornyshev, Ionic liquids at electrified interfaces. *Chem. Rev.* **2014**, 114, 2978-3036. *Copyright 2014 American Chemical Society).*
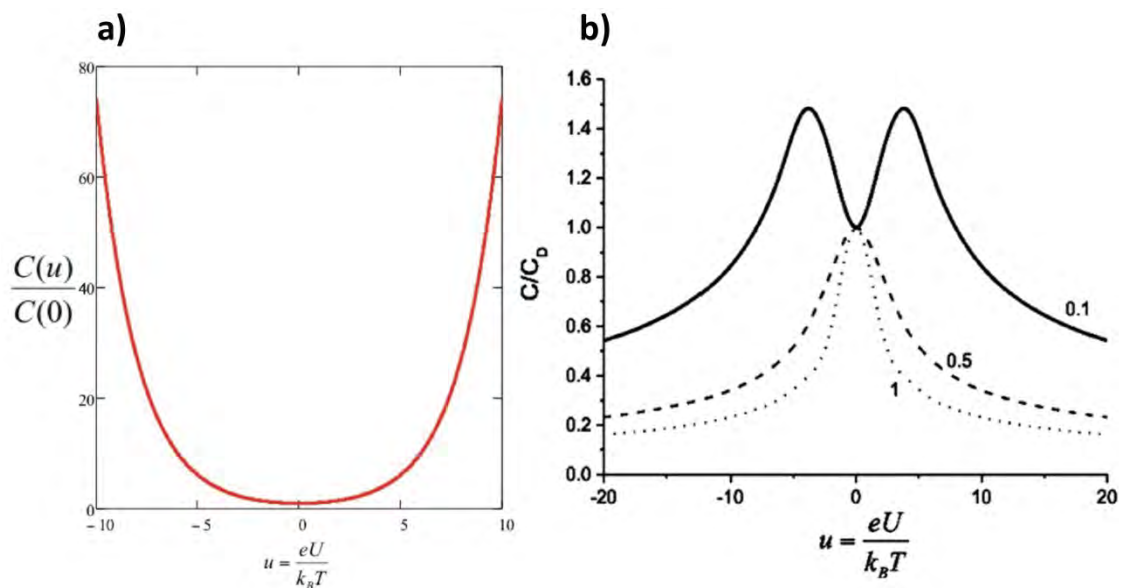
Figure 5 a) U-shape capacitance curve predicted by the Gouy-Chapman EDL model; b) Capacitance curves predicted by the Kornyshev EDL model showing bell and camel shapes for large and small values of γ respectively. (Adapted with permission from M. V. Fedorov, A. A. Kornyshev, Ionic liquids at electrified interfaces. *Chem. Rev.* **2014**, 114, 2978-3036. *Copyright 2014 American Chemical Society).*

2.1.1. Potential Screening Measurements

In order to study ILs at polarized electrode interfaces, a voltage ($U_{applied}$) is applied to the electrolyte through two identical (same materials and contact area) counter and working electrodes (CE and WE), as sketched in Figure 6. The nomenclature of the electrodes is taken from a potentiostatic arrangement in which the $U_{applied}$ is always applied against the CE.
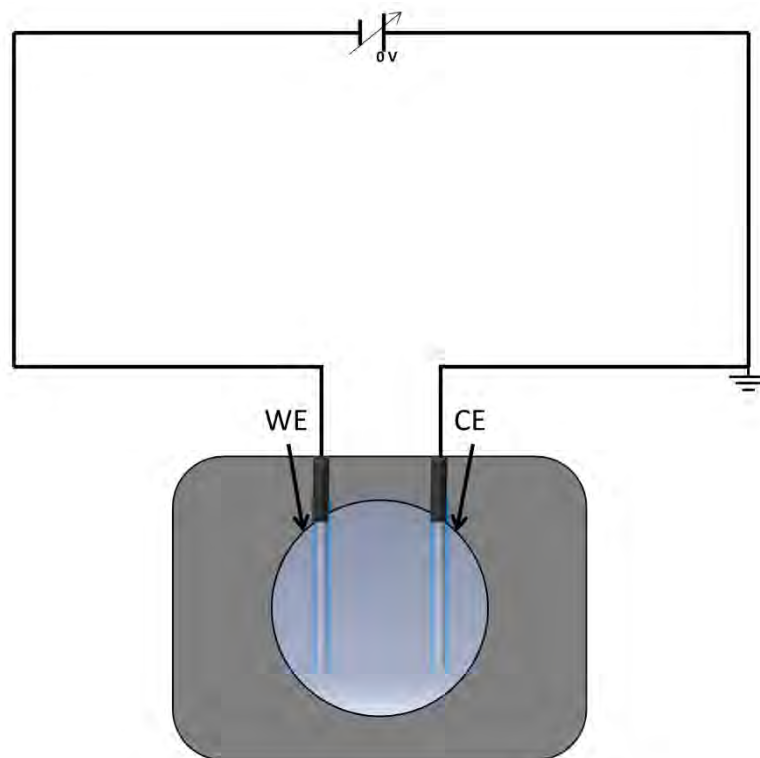
Figure 6 Sketch of the electrochemical cell used for PS measurements.

This means that for negative voltages applied to WE, the CE is positively polarized and attracts the anions of the IL to the interface, it therefore is termed as anode. Note that the position of the ground is not particularly relevant in standard electrochemical measurements; in order to perform PS measurements with XPS, the ground has to be indicated to identify the interface under study. In the configuration shown in Figure 6, XPS probes the interface at the CE acting as anode.

XPS is an ultra-high vacuum (UHV) technique that exploits the photoelectric effect,[38-40] which occurs, when an electromagnetic radiation (hv) hits a material and photoelectrons with defined kinetic energy (KE^{CE}) are emitted from this material.
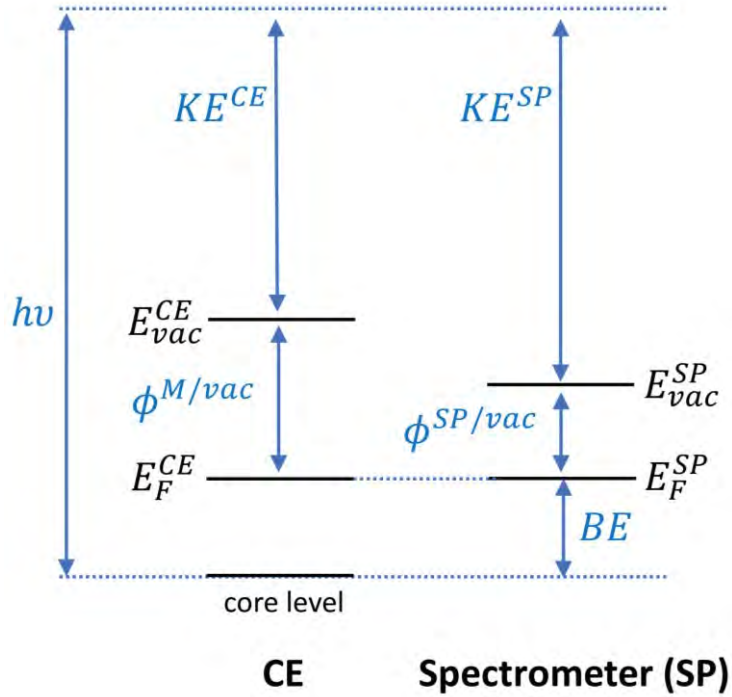
Figure 7 Energy diagrams depicting the potential of metallic CE and spectrometer.

In the case of CE grounded, that is, the Fermi levels of spectrometer (E_F^{SP}) and CE (E_F^{CE}) are in equilibrium, the kinetic energy of the photoelectrons (KE^{SP}) is measured at a spectrometer with a defined work function ($\phi^{SP/vac}$). Since the energy of the irradiating photons ($h\nu$) is known, the binding energy (BE) of the photoelectrons is given by the following equation:

$$BE = h\nu - KE^{SP} - \phi^{SP/vac} \tag{6}$$

When an IL is in contact with the grounded CE in the electrochemical cell, the intrinsic binding energy (BE_{int}) of the IL can be defined as:

$$BE_{int} = h\nu - KE^{SP} - \phi^{SP/vac} + (E_{vac}^{IL} - E_{vac}^{CE}) + \phi^{CE/vac} \tag{7}$$

where $\phi^{CE/vac}$ is the work function of the CE and $E_{vac}^{IL} - E_{vac}^{CE}$ is the vacuum level difference between the IL and the CE.

Note that, due to the difficulty to define the Fermi level of ILs, we here define the BE_{int} of the IL as the energy difference between the core orbital level of atoms in the IL and the vacuum level of the IL, similar to the convention of gas phase XPS.
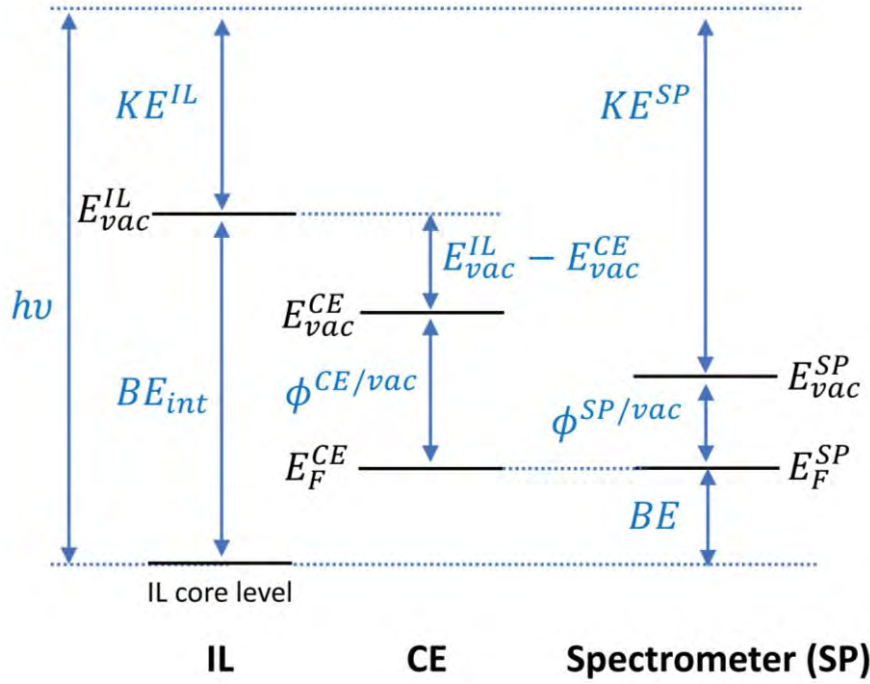
Figure 8 Energy diagrams depicting the potential of IL, metallic CE and spectrometer.

In this experiment, the *BE* was defined and reported based on the convention of a metallic sample measured by XPS as in equation (6) and the *BE* is related to BE_{int} as

$$BE = BE_{int} - (E_{vac}^{IL} - E_{vac}^{CE}) - \phi^{CE/vac} \tag{8}$$

Note that BE_{int}, E_{vac}^{CE}, and $\phi^{CE/vac}$ are not affected by the applied potential, thus the *BE* is shifted as the amount of ΔE_{vac}^{IL}.

In the case of the CE grounded, the potential of the IL is shifted by the amount of the potential screening of CE ($e\varphi^{CE/IL}$) and the vacuum level difference between the IL and CE, $E_{vac}^{IL} - E_{vac}^{CE}$, is changed by the amount of this screening. This relation can be verified by the following cycle: (A) an electron is brought from the Fermi level of the electrode to its vacuum level, this costs the work function $\phi^{CE/vac}$; (B) the electron is taken from the vacuum level of CE to that of the IL, this costs the difference in vacuum levels, $E_{vac}^{IL} - E_{vac}^{CE}$; (C) the electron is brought from the vacuum level of the IL to inside the IL, this costs the electrolyte surface potential (or the electric potential difference between the vacuum and the IL) $e\varphi^{vac/IL}$; (D) the electron is brought across the double layer to the metal Fermi level, this costs the electric

potential difference between the IL and CE with the negative chemical potential of the electron in the metal ($e\varphi^{IL/CE} + \mu^{CE}$).

From this cycle, we can derive

$$\phi^{CE/vac} + (E_{vac}^{IL} - E_{vac}^{CE}) + e\varphi^{vac/IL} + e\varphi^{IL/CE} + \mu^{CE} = 0 \tag{9}$$
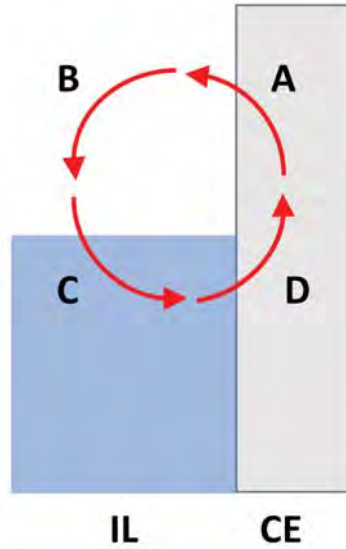
Figure 9 Schematic representation of solid/vacuum, vacuum/liquid, liquid/solid interface and the energies involved to move an electron across them (letters, see text).

Since $\phi^{CE/vac}$, $e\varphi^{vac/IL}$, and μ^{CE} are not depending on the applied potential, this implies that changes in the vacuum level difference between the electrode and the IL are equal to changes in the EDL potential:

$$\Delta(E_{vac}^{IL} - E_{vac}^{CE}) = e\Delta\varphi^{CE/IL} \tag{10}$$

Therefore, the shift of BE of the IL is proportional to the difference of the potential screening at the CE/IL interface.

$$\Delta BE = e\Delta\varphi^{CE/IL} \tag{11}$$

Since in this example the CE was positively polarized and therefore the anode, $e\Delta\varphi^{CE/IL}$ can be defined as potential screening at the anode or anodic voltage ($e\Delta\varphi_{anodic}$).

2.1.2.　State of the Art of Studies on ILs at Polarized Interfaces

As discussed in Chapter 2.1, the EDL structure of ILs is typically investigated by measuring the differential capacitance (C_d) in electrochemical impedance spectroscopy (EIS) and the unique features of the resulting C_d curves, such as the bell or camel shape,[7-9, 41-43] can be successfully interpreted through the Kornyshev model[11, 44] as well as by computer simulations.[12, 20, 45-48] In addition, the interfacial properties of ILs at electrified interfaces have been addressed by cyclic voltammetry (CV),[49, 50] sum-frequency generation (SFG),[51, 52] X-ray reflectivity,[18, 53, 54] scanning tunneling microscopy (STM),[55-57] atomic force microscopy (AFM),[14, 15, 57, 58] infrared,[59-62] Raman,[63] and nuclear magnetic resonance (NMR) spectroscopy.[64] Some of these studies reveal various unique properties of the EDL at the IL/electrode interface, e.g., the slow response of ions,[42, 47] hysteresis behavior,[54, 61] and layering.[57, 58] Furthermore, SFG,[51] infrared spectroscopy,[62] surface-enhanced Raman spectroscopy,[63] STM,[56, 65] together with computational methods,[21, 66] have provided information on the adsorption geometry and the reorientation of ILs in response to the applied potential. Moreover, the effect of specific adsorption between aromatic imidazolium-rings and a graphite electrode surface, which causes a shorter adsorption distance and a high surface charge density has been addressed by EIS[43] and computational methods.[48]

2.1.3.　State of the Art of Electrochemical XPS

XPS can be used as an excellent tool to characterize the electrolyte/electrode interface due to its ability to gain information on the chemical composition and the potential drop at electrified interfaces. Electrochemical studies and XPS were combined for the first time by Hansen et al.[67, 68] In these studies, the authors demonstrated that a polarized electrode can be removed from the electrolyte solution in non-faradaic conditions keeping the EDL intact. This so-called "emersed EDL" can be subsequently studied by XPS analyzing signal intensities and *BE* shifts. Although the emersion procedure was performed in ambient atmosphere (*ex-situ*), these pioneering experiments showed that the properties of the EDL at different external voltages applied can be successfully studied by means of XPS. Furthermore, this *ex-situ* emersed electrode technique was successfully employed to study anodic oxidation of iridium electrodes,[69] EDL formation of aqueous electrolytes containing Cs^+,[70] specific adsorption of chloride anions on Ag electrodes.[71]

Later, Hecht and Strehblow studied the EDL formation on emersed Ag electrodes in acidic and alkaline aqueous solutions by XPS.[72, 73] In both studies, the emersion procedure of the electrodes under potential control was performed under argon atmosphere in a chamber attached to the UHV system. This methodology avoided intermediate exposition of the sample to ambient atmosphere and can be defined as *quasi in-situ*. Additionally, *quasi in-situ* XPS studies provided information on the structure and electrochemistry of self-assembled-monolayers on Au(111),[74, 75] electrochemically formed oxide layers on metallic electrodes,[76-79] interfacial structures and reactions of Li-ion battery materials,[80] intercalation processes and stability of HOPG electrodes in an IL electrolyte.[81, 82]

In contrast to the volatile nature of aqueous electrolytes used in these early studies, ILs have a negligible vapor pressure, which unlocks the possibility to study them by UHV techniques as XPS.[22-29] In this regard, an electrochemical cell, comprised of electrodes and electrolyte (IL), can be introduced in UHV system and electrochemical phenomena caused by electrical stimuli can be studied *in-situ* with XPS. With *in-situ* XPS, faradaic phenomena in ILs were successfully studied such as reduction of Fe(III) to Fe(II)[83] electrochemical dissolution of copper,[84] electrodeposition of potassium and rubidium at electrodes[85, 86] and electro-degradation of ILs induced by the applied voltage.[87] *In-situ* XPS also provided information on charged IL/electrodes interfaces in non-faradaic conditions, monitoring the charging shifts at the IL/vacuum interface. This approach can visualize the potential screening (PS) across the electrode/IL interface with the slow dynamic response of ILs to an applied voltage.[88, 89]

2.2. Experimental Apparatus

Figures 10 and 11 show the UHV system used in this thesis to measure PS of ILs at polarized electrode interfaces with XPS. This so-called Dual Analyzer System for Surface Analysis (DASSA) was developed in cooperation with Omicron NanoTechnology to study macroscopic amount of liquid samples in UHV. The chamber is composed of an analysis chamber, a preparation chamber and a load lock. The preparation chamber is equipped with a sputter gun, a quadrupole mass spectrometer (QMS) and low energy electron diffraction (LEED). Two identical hemispherical ARGUS electron analyzers are mounted in the analysis chamber with an emission angle of 0° and 80° relative to the surface normal. This geometry allows to record XP spectra in normal (0°) and grazing (80°) emission simultaneously keeping the sample in horizontal position, which avoids dripping of macroscopic liquid samples.
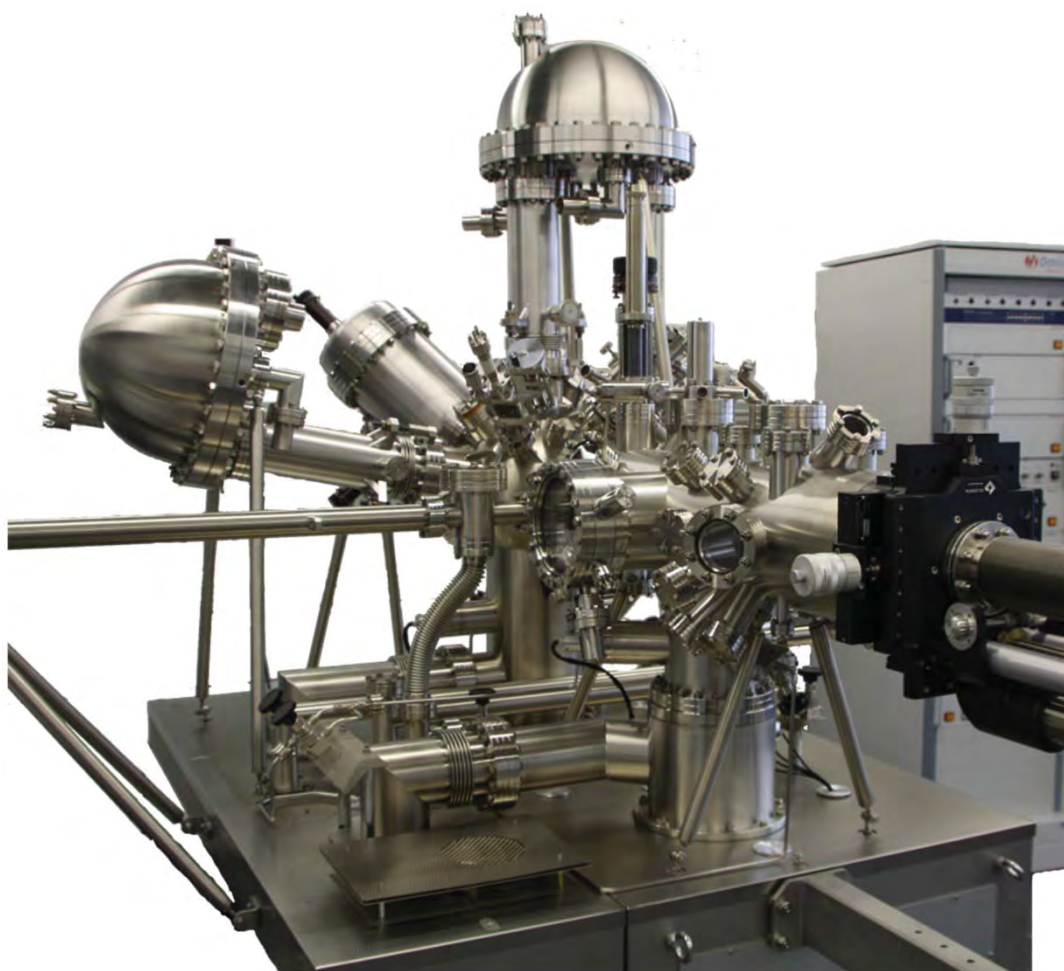
Figure 10 Photo of the UHV-based XPS chamber (DASSA) used in this thesis.
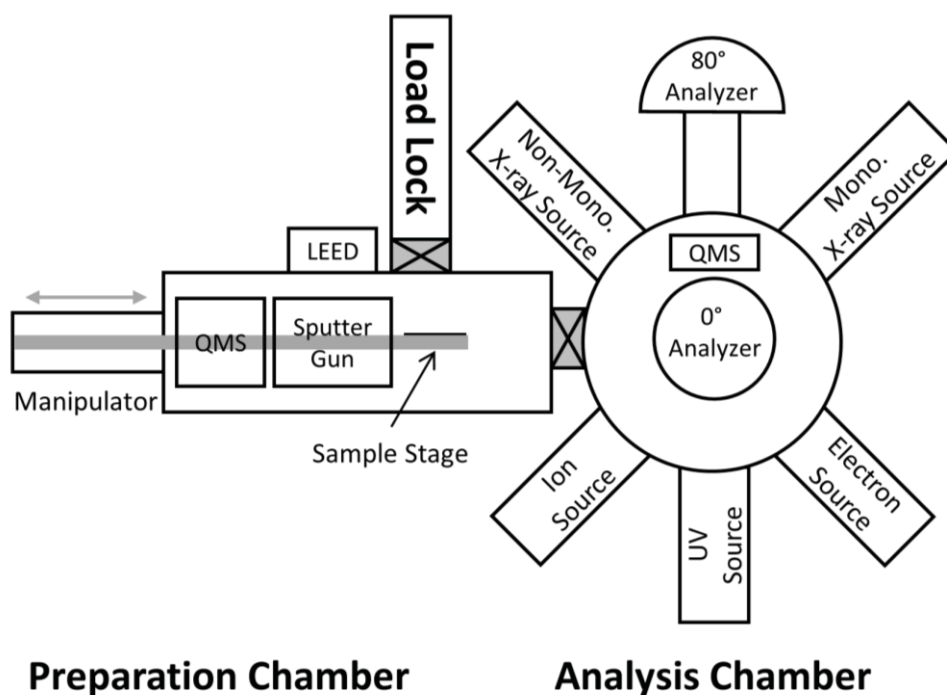
Figure 11 Schematic representation of DASSA.

A monochromated Al K_{α} source is mounted to the analysis chamber in a "magic angle configuration" with respect to the 0° and 80° analyzer. Furthermore, a non-monochromated dual anode X-ray gun, generating either Al K_{α} or Mg K_{α} radiation, an electron source, an ion source, an ultraviolet source (UV source) and a QMS are mounted to the analysis chamber. More details about the general setup of the chamber can be found in Ref. 90, while the following part of this section will focus on the features of the chamber used to perform the electrochemical XPS measurements presented in this work.

The **electrochemical cell** used for the measurements described in the following (Figure 12) was developed during this thesis and consists of a molybdenum sample holder (3) mounted to a standard Omicron tantalum sample plate (2) through four conic tantalum screws (1); two metal wires (5) are used as WE and CE electrodes mounted to a ceramic block (4) via two molybdenum screws; polytetrafluoroethylene spacers (6) are used to avoid contact between the molybdenum sample holder and electrodes and are fixed through four cylindrical molybdenum screws (7). The metal wires are flame annealed prior to mounting and paced in the molybdenum sample holder (3) in such a way that their contact areas with the ILs are identical. The electrochemical cell after assembling is filled with ~ 0.2 mL of IL and introduced in the load lock of the chamber where it can be degassed for at least 12 hours.
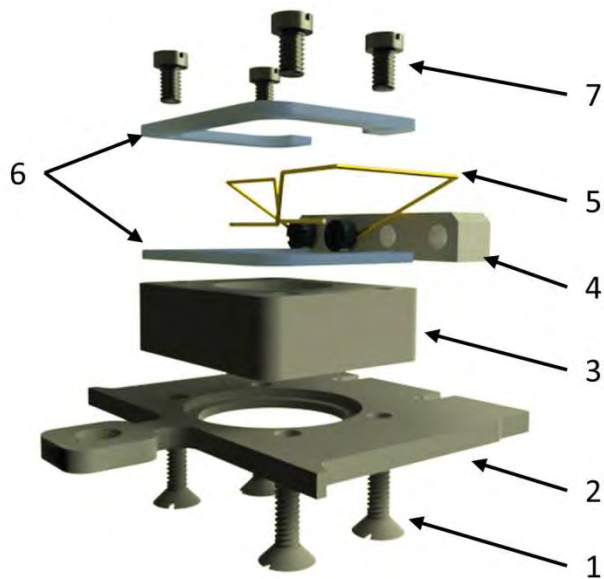
Figure 12 (left) Photo of the electrochemical cell used in this thesis; (right) Explosion drawing of the electrochemical cell showing all its components (numbers, see text).

After degassing, the cell is transferred to the preparation chamber of the DASSA system and slid in the **sample stage** (Figure 13 left) so that the molybdenum screws mounted on the ceramic block (5) are connected to the potentiostat (Keithley 2450) through two electrical contact springs (Figure 13 right).
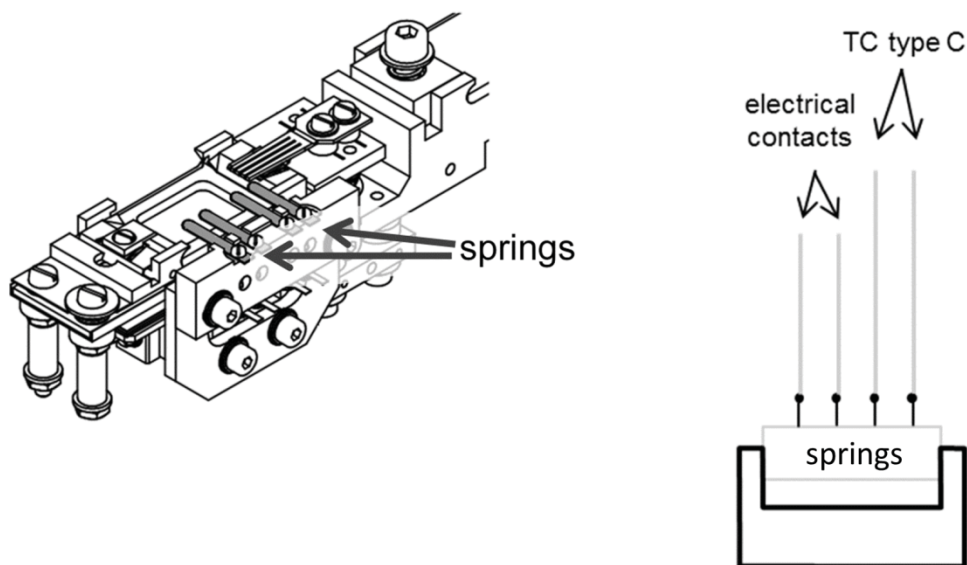
Figure 13 (left) Sketch of the sample stage of DASSA instrument with its four contact springs; (right) sketch of electrical contacts and thermocouples springs.

Subsequently, the electrochemical cell is transferred to the analysis chamber where the purity of the IL is checked with wide scan spectra (pass energy: 150 eV; dwell time: 0.5 s) and region spectra (pass energy: 35 eV; dwell time: 1.5 s) with the above mentioned mono-chromated Al K_α source and 0° ARGUS electron analyzer (spectra and quantitative analysis for all the ILs used in this thesis are reported in Chapter 2.3). The PS measurements are per-formed recording the *BE* shift of a core level of the IL while voltage steps are applied with the potentiostat. The voltage steps have duration of 139 s; simultaneously, the current flow be-tween WE and CE is recorded. After applying a certain voltage and waiting for 60 s to ensure stable conditions, region spectra of one of the core levels of the IL are acquired with a pass energy of 35 eV (spectra vs $U_{applied}$ and experimental aspect can be found in Chapter 3).

2.3. Ionic Liquids

An overview of the ILs used in this work is given in Table 1 including the abbreviations used throughout this thesis, the IUPAC names and the molecular structures.

1,3-dimethylimidazolium bis[(trifluoromethyl)sulfonyl]imide, $[C_1C_1Im][Tf_2N]$, 1-methyl-3-octylimidazolium bis[(trifluoromethyl)sulfonyl]imide, $[C_8C_1Im][Tf_2N]$, and 1-methyl-3-octylimidazolium chloride, $[C_8C_1Im]Cl$, were synthesized under ultrapure conditions according to previous publications;[91, 92] 1-butyl-1-methylpyrrolidinium bis[(trifluoromethyl)sulfonyl]imide, $[C_4C_1Pyrr][Tf_2N]$, was purchased from IoLitech with a purity >99%.

Table 1 Cations and anions of ILs investigated in this study.

Abbreviation	Structure	Name
$[C_1C_1Im]^+$		1,3-dimethylimidazolium
$[C_8C_1Im]^+$		1-methyl-3-octylimidazolium
$[C_4C_1Pyrr]^+$		1-butyl-1-methylpyrrolidinium
$[Tf_2N]^-$		bis[(trifluoromethyl)sulfonyl]imide
Cl^-		chloride
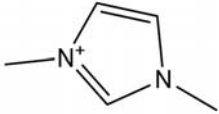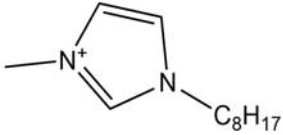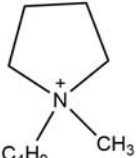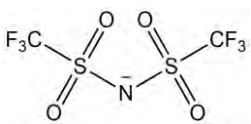
In the following, the XP spectra of the neat ILs will be discussed. Wide scan spectra of the different ILs are shown in Figures 14-17 with only the expected signals observed, which reveals the absence of major IL contaminations. In particular, no Si signals at *BE*

(Si 2p) ~ 100 eV are visible, which indicates a common surface-active contamination of ILs with polysiloxanes.[93]

Figure 14 XP wide spectrum of [C₁C₁Im][Tf₂N].
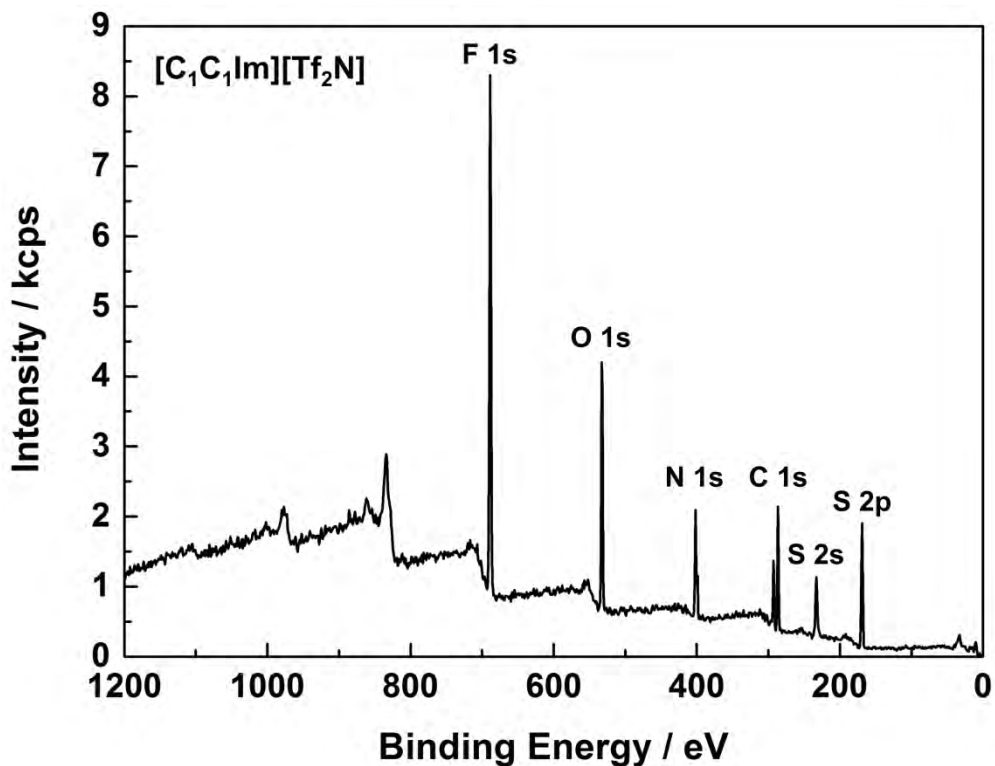
Figure 14 XP wide spectrum of $[C_1C_1Im][Tf_2N]$.
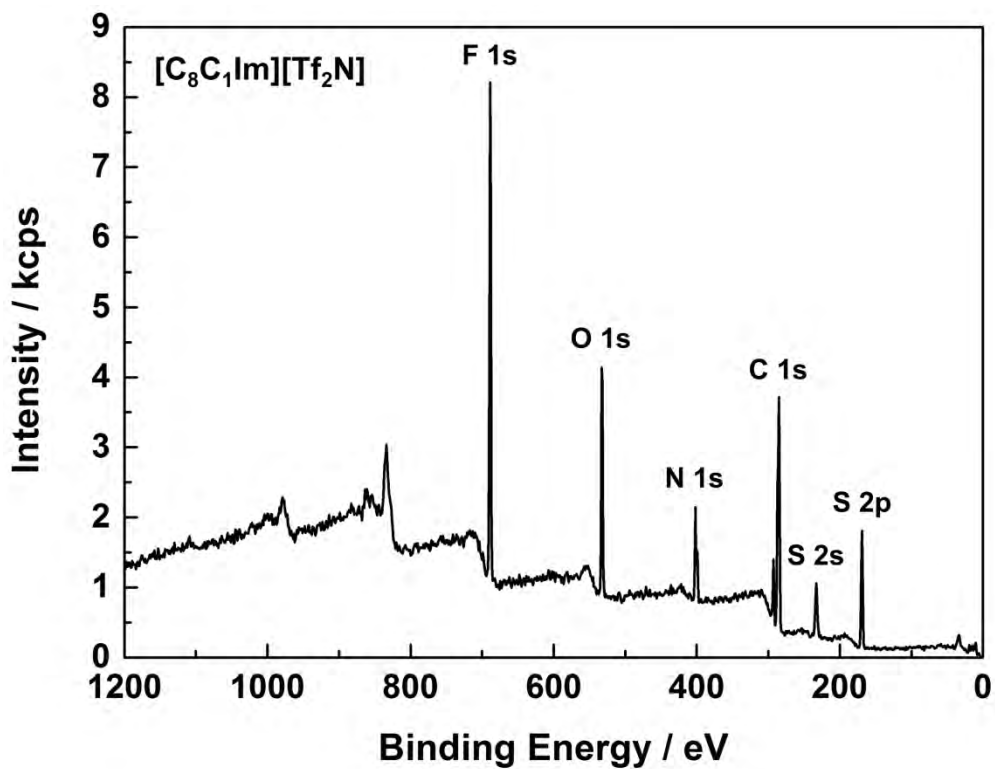
Figure 15 XP wide spectrum of $[C_8C_1Im][Tf_2N]$.
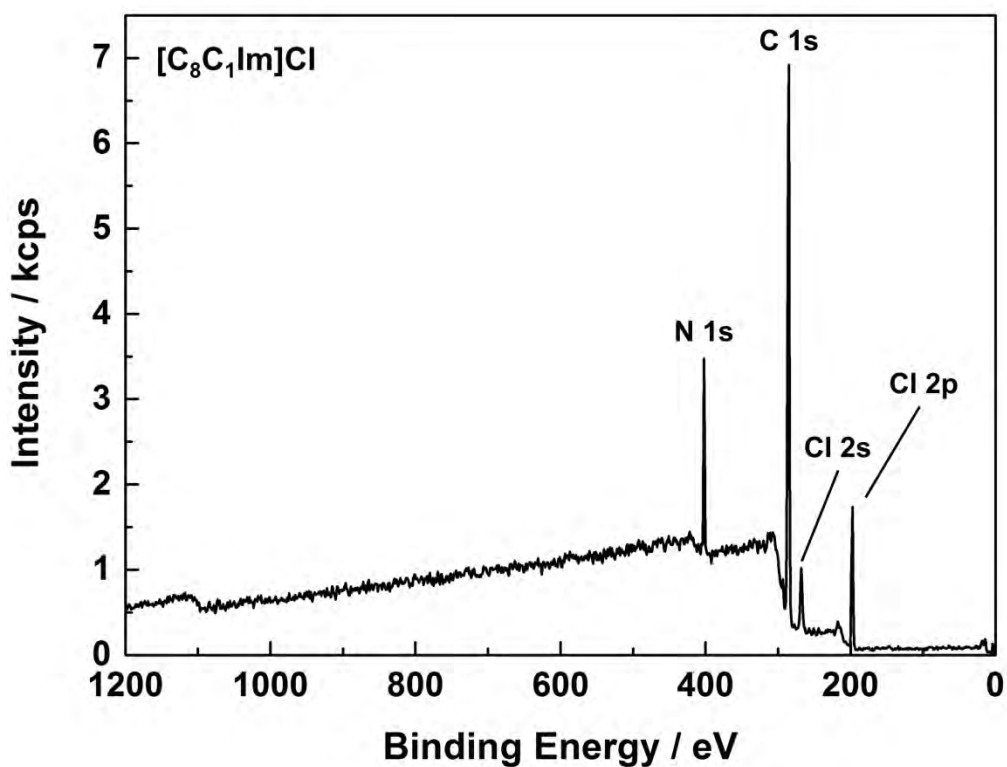
Figure 16 XP wide spectrum of [C₈C₁Im]Cl.
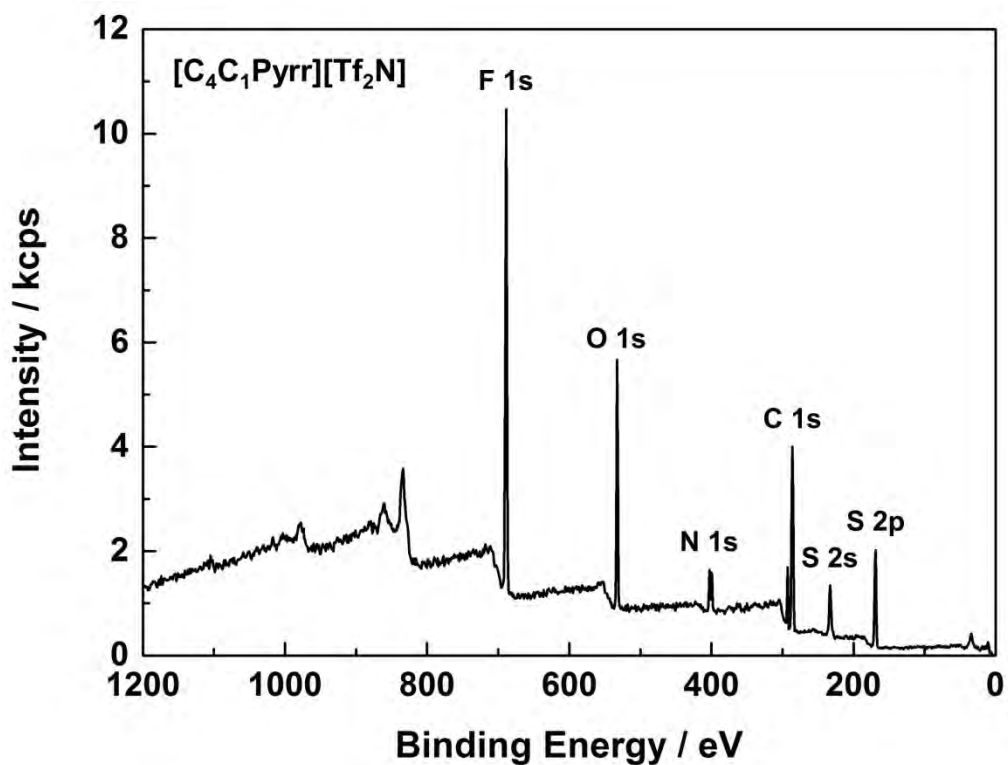
Figure 17 XP wide spectrum of [C₄C₁Pyrr][Tf₂N].

In a detailed and quantitative analysis, region spectra of the C 1s, N 1s, F 1s, O 1s, S 2p and Cl 2p are shown in Figures 18-21 along with the corresponding XP peaks fitting. In Tables 2-5, the experimental atomic composition of each IL derived from XPS is then compared with the nominal one expected from the molecular structures (note that all binding energy values in the tables are given as measured without any *BE* corrections; hence, values for identical species may vary by ± 0.35 eV).

The XP spectra of $[C_1C_1Im][Tf_2N]$ in Figure 18 show single peaks in the O 1s and F 1s regions of the four oxygen atoms and six fluorine atoms, respectively, of the $[Tf_2N]^-$ anion. The two peaks in the N 1s region are attributed to the two nitrogen atoms of the cation (401.8 eV) and to the nitrogen atom of the anion (399.2 eV). The 2:1 intensity is in accordance with the stoichiometry of $[C_1C_1Im][Tf_2N]$ (see molecular structure in Figure 18 and Table 2). The C 1s region is more complicated due to the presence of several chemically inequivalent species. The component at highest *BE* (292.6 eV) results from the two chemically equivalent carbon atoms of $[Tf_2N]^-$. The larger peak at lower *BE* can be deconvoluted in two components: C_2 at 287.3 eV and C_{het} at 286.4 eV. The intensity ratio between the C_2 and the C_{het} components is 1:4 in accordance with the stoichiometry of the $[C_1C_1Im]^+$ (see molecular structure in Figure 18). The S 2p region shows an asymmetric peak which stems from the two chemically equivalent sulfur atoms of $[Tf_2N]^-$. The asymmetry of the S 2p peak is related to spin-orbit-splitting into the $2p_{1/2}$ and $2p_{3/2}$ components, which have a ratio of 1:2 and are separated by 1.21 eV to each other.

The XP region spectra of $[C_8C_1Im][Tf_2N]$ in Figure 19 can be described as for $[C_1C_1Im][Tf_2N]$ except for the C 1s region. In the C 1s region, a fourth component (C_{alkyl}) has to be added at lower *BE* (284.8 eV) to take into account the seven carbon atoms of the alkyl side chain (see molecular structure in Figure 19).

Figure 20 shows the XP region spectra of $[C_8C_1Im]Cl$ with similar cation signals as for $[C_8C_1Im][Tf_2N]$. The Cl^- anion leads to a Cl 2p signal at around 197.4 eV *BE* with two spin-orbit-split components $2p_{1/2}$ and $2p_{3/2}$ (intensity ratio 1:2 and 1.60 eV separation).

The XP region spectra of $[C_4C_1Pyrr][Tf_2N]$ are shown in Figure 21. All signals related to $[Tf_2N]^-$ are as for $[C_8C_1Im][Tf_2N]$ and $[C_1C_1Im][Tf_2N]$. The N 1s peak at higher *BE* (402.6 eV) is due to the $[C_4C_1Pyrr]^+$ cation and shows an intensity ratio of ~1:1 with the N 1s peak of the $[Tf_2N]^-$ as expected (see molecular structure in Figure 21). The C 1s region shows three distinguishable components. The one at highest *BE* (292.9 eV) originates from the CF_3-

groups of $[Tf_2N]^-$ as observed for $[C_8C_1Im][Tf_2N]$ and $[C_1C_1Im][Tf_2N]$. The main peak at lower *BE* values can be consistently deconvoluted with two components related to five alkyl carbon atoms (C_{alkyl}) and the four carbon atoms directly bound to the nitrogen atom (C_{het}) (see molecular structure in Figure 21).
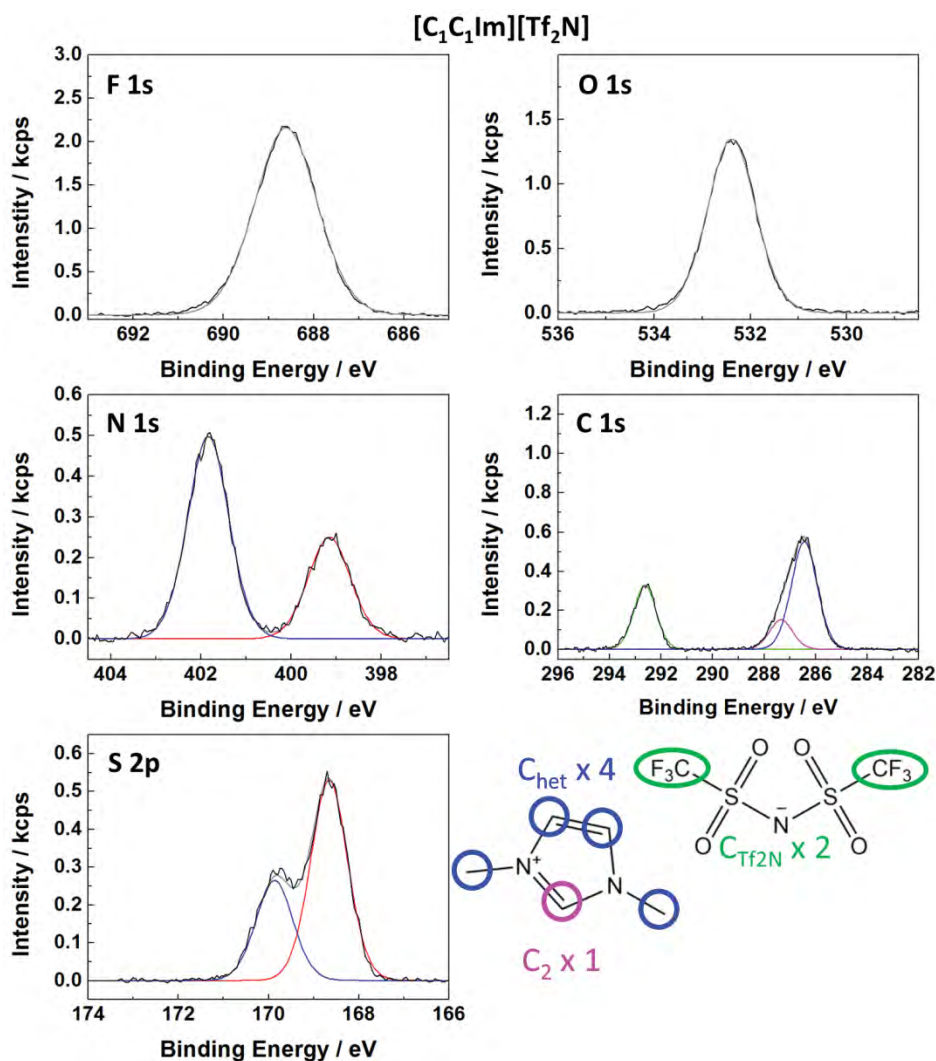
Figure 18 F 1s, O 1s, N 1s, C 1s and S 2p spectra of [C₁C₁Im][Tf₂N] recorded in normal emission. The peak fitting used for quantitative analysis is also shown.

Table 2 Quantitative analysis of the XP spectra of [C₁C₁Im][Tf₂N].

	[C₁C₁Im][Tf₂N]								
Ions	**[C₁C₁Im]⁺**				**[Tf₂N]⁻**				
XPS regions	**N 1s** N_{Im}	**C 1s** C_2	**C 1s** C_{het}	**C 1s** C_{alk}	**F 1s** F_{Tf2N}	**O 1s** O_{Tf2N}	**N 1s** N_{Tf2N}	**C 1s** C_{Tf2N}	**S 2p** S_{Tf2N}
BE / eV	401.8	287.3	286.4	-/-	688.6	532.4	399.2	292.6	168.7
Nominal ratio	2.0	1.0	4.0	-/-	6.0	4.0	1.0	2.0	2.0
Exp. ratio	2.0	0.9	3.7	-/-	6.1	4.1	1.0	1.9	2.1
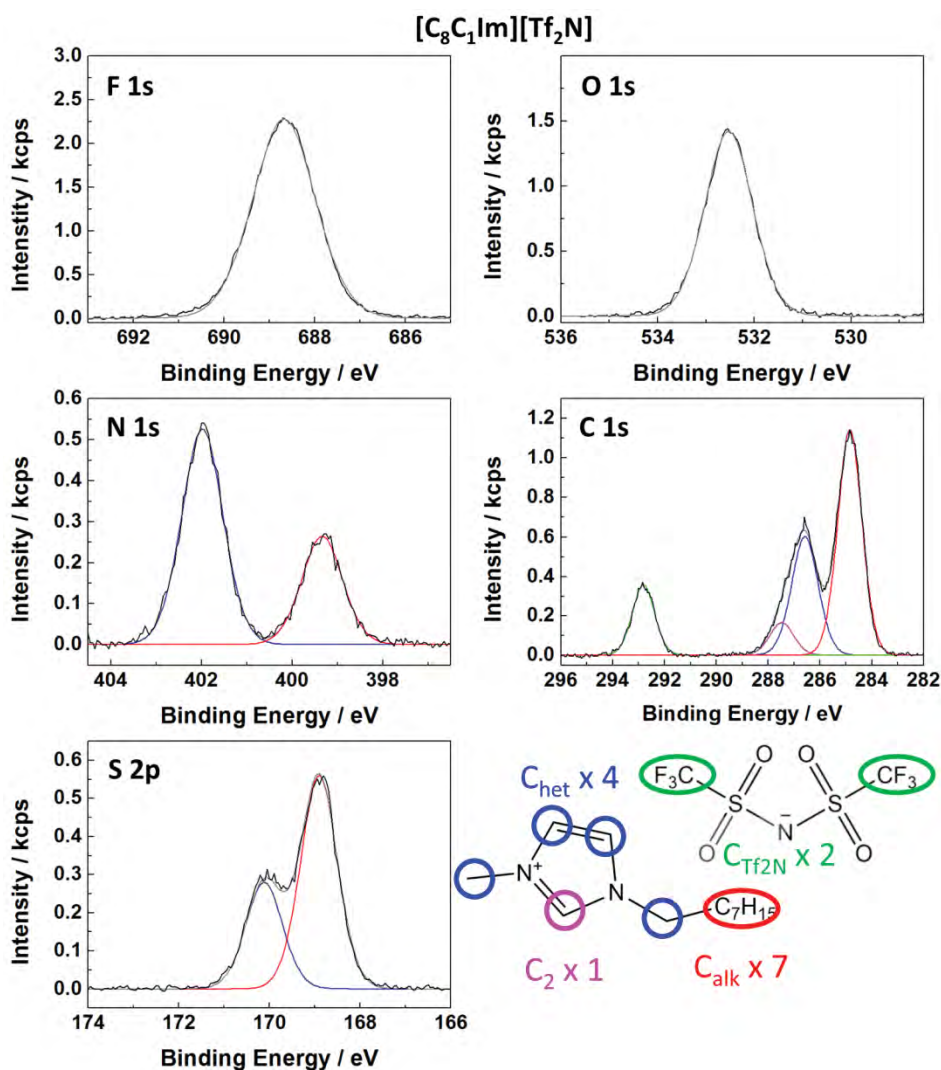
Figure 19 F 1s, O 1s, N 1s, C 1s and S 2p spectra of [C$_8$C$_1$Im][Tf$_2$N] recorded in normal emission. The peak fitting used for quantitative analysis is also shown.

Table 3 Quantitative analysis of the XP spectra of [C$_8$C$_1$Im][Tf$_2$N].

	[C$_8$C$_1$Im][Tf$_2$N]								
Ions	[C$_8$C$_1$Im]$^+$				[Tf$_2$N]$^-$				
XPS regions	N 1s N$_{Im}$	C 1s C$_2$	C 1s C$_{het}$	C 1s C$_{alk}$	F 1s F$_{Tf2N}$	O 1s O$_{Tf2N}$	N 1s N$_{Tf2N}$	C 1s C$_{Tf2N}$	S 2p S$_{Tf2N}$
BE / eV	402.0	287.5	286.6	284.8	688.7	532.5	399.3	292.8	168.9
Nominal ratio	2.0	1.0	4.0	7.0	6.0	4.0	1.0	2.0	2.0
Exp. ratio	2.0	1.0	4.0	6.8	6.1	4.1	1.0	2.0	2.1
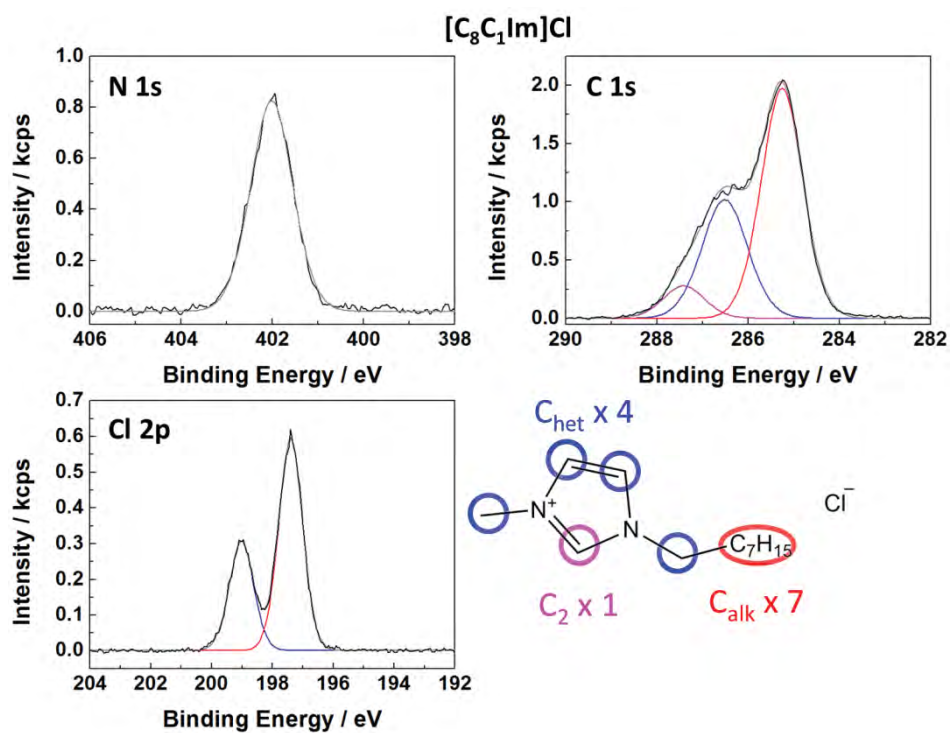
Figure 20 N 1s, C 1s and Cl 2p spectra of [C₈C₁Im]Cl recorded in normal emission. The peak fitting used for quantitative analysis is also shown.

Table 4 Quantitative analysis of the XP spectra of [C₈C₁Im]Cl.

	[C₈C₁Im]Cl				
Ions	[C₈C₁Im]⁺				Cl⁻
XPS regions	N 1s N_{Im}	C 1s C_2	C 1s C_{het}	C 1s C_{alk}	Cl 2p
BE / eV	402.0	287.5	286.6	285.3	197.4
Nominal ratio	2.0	1.0	4.0	7.0	1.0
Exp. ratio	1.9	1.0	4.0	7.1	1.0
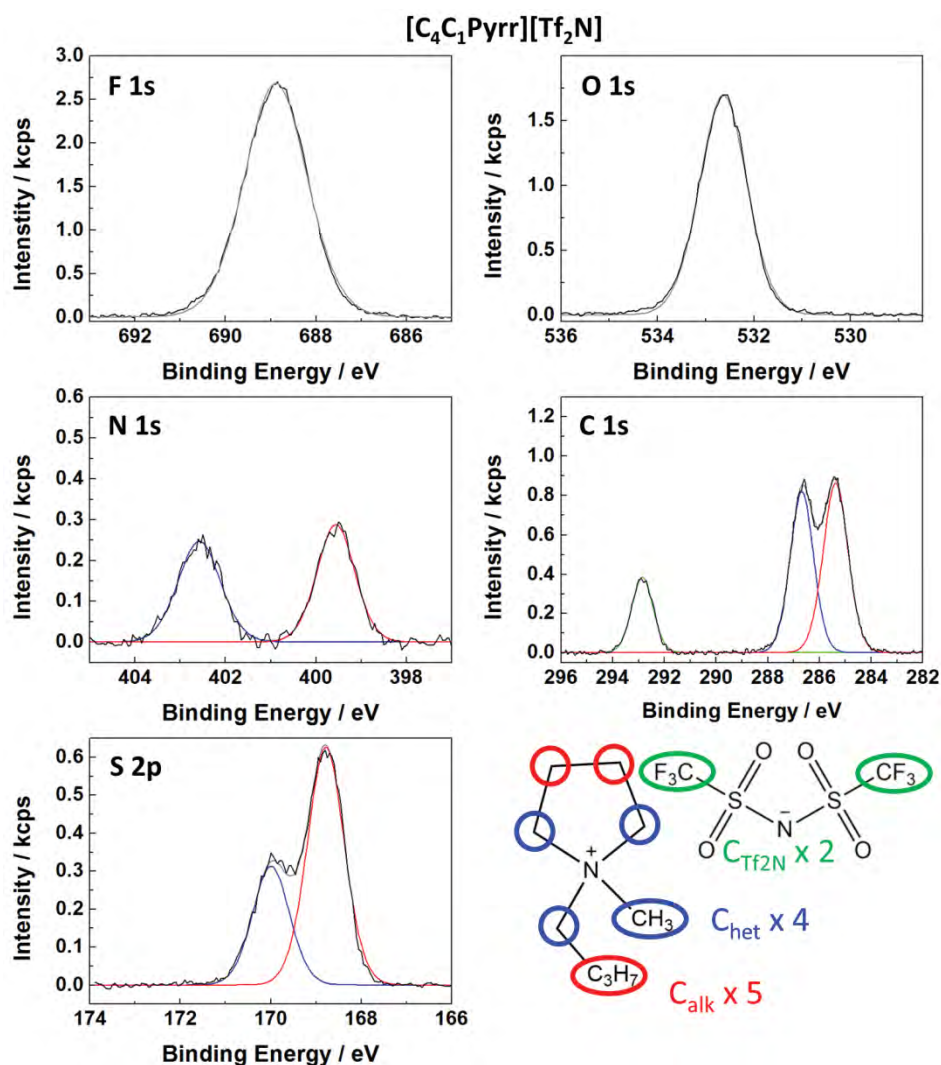
Figure 21 F 1s, O 1s, N 1s, C 1s and S 2p spectra of [C$_4$C$_1$Pyrr][Tf$_2$N] recorded in normal emission. The peak fitting used for quantitative analysis is also shown.

Table 5 Quantitative analysis of the XP spectra of [C$_4$C$_1$Pyrr][Tf$_2$N].

	[C$_4$C$_1$Pyrr][Tf$_2$N]								
Ions	[C$_4$C$_1$Pyrr]$^+$				[Tf$_2$N]$^-$				
XPS regions	N 1s N_{Pyr}	C 1s C_2	C 1s C_{het}	C 1s C_{alk}	F 1s F_{Tf2N}	O 1s O_{Tf2N}	N 1s N_{Tf2N}	C 1s C_{Tf2N}	S 2p S_{Tf2N}
BE / eV	402.6	-/-	286.7	285.4	688.9	532.6	399.6	292.9	168.8
Nominal ratio	1.0	-/-	4.0	5.0	6.0	4.0	1.0	2.0	2.0
Exp. ratio	0.9	-/-	4.2	4.7	6.3	4.2	0.9	1.8	2.0

3. Electrode / Neat Ionic Liquid Interfaces

The content of this chapter is based and adapted from the following publication:[94]

Potential Screening at Electrode/Ionic Liquid Interfaces from In Situ X-ray Photoelectron Spectroscopy

F. Greco, S. Shin, F. J. Williams, B. S. J. Heller, F. Maier and H.-P. Steinrück

ChemistryOpen, 2019, **8**, 1365-1368

3.1. Introduction

As mentioned in the introductory Chapter 1, ILs have drawn significant interest in electrochemistry due to their enormous potential as solvent-free electrolytes.[95] ILs can be successfully used for applications in batteries,[96] supercapacitors,[97] and electrodeposition.[98] Understanding their properties at charged interfaces is crucial for applications because many physicochemical phenomena occur at the interface like capacitance charging and redox reactions.

The electrical double layer (EDL) structure and properties at charged IL/electrode interfaces are influenced by properties of cations and anions, such as size, shape, dipole moments, and specific interactions with the electrode. In addition, the polarity of the electrode can affect the EDL, due to different counterions at anode and cathode. Recently, the reliability of experimental observations of charged IL interfaces by electrochemical impedance spectroscopy (EIS) and cyclic voltammetry (CV) has been discussed. These techniques often yield inconsistent/irreproducible results due to impurities, neglect of the slow kinetic response, and questionable data analysis in EIS.[41, 44, 49, 99]

In this chapter, the properties of the EDLs are systemically studied with *in situ* XPS measurements, which provide complementary and reliable information on the potential screening (PS) at various IL/electrode interfaces (ILs studied, see Table 1 in Chapter 2.3). Our approach has various advantages: (1) we measure PS in an equilibrium state after the formation of the EDL, thus slow kinetics of ion displacement is not affecting our results. (2) We measure under ultra-high vacuum (UHV) condition with very clean ILs, as was carefully

checked by XPS.[91, 92, 100] (3) XPS provides direct access to the PS under DC conditions, without having to assume an equivalent circuit in EIS, which has been questioned in literature.[99] The properties of the EDLs can be directly studied by comparing the PS on anode and cathode via binding energy shifts of IL signals in XPS. We believe that these advantages open a new route to address IL/electrode interfaces by systemically studying various ILs and electrodes.

3.2.　Methods and Materials

The PS measurements were performed using the UHV system and the electrochemical cell described in Chapter 2.2. The Pt (99.99 %) and Au (99.995 %) electrodes with a diameter of 0.30 and 0.25 mm, respectively, were purchased from MaTeck and flame annealed prior to use. The electrodes were connected to the potentiostat (Keithley 2450) through two contact springs located at the head of the manipulator of the UHV system (see Chapter 2.2 for more details). $[C_1C_1Im][Tf_2N]$, $[C_8C_1Im][Tf_2N]$ and $[C_8C_1Im]Cl$ were synthesized according to previous publications;[91, 92] $[C_4C_1Pyrr][Tf_2N]$ was purchased from IoLitech with a purity >99%. The purities of the ILs were carefully checked by XPS (see Chapter 2.3). For each combination of IL and metal, the electrodes were carefully mounted on the electrochemical cell in such a way that their contact areas with the ILs were identical (±5%) to avoid geometry effects on the PS (see Appendix, Figure A3). XPS was carried out using a monochromated Al Kα source and a hemispherical ARGUS analyzer (See Chapter 2.2). High-resolution scans were recorded with a pass energy of 35 eV and a dwell time of 0.5 s with an overall energy resolution of 0.4 eV (see Chapter 2.2). Potential sweep measurements and chronoamperometry were performed using the Keithley 2450 source meter. The potential sweep measurement scan rate was 50 mV/s.

3.3.　Experimental Aspects

Figure 22a shows the electrochemical setup used to measure PS in XPS at the IL/vacuum interface. The external voltages ($U_{applied}$) are applied to the ILs through identical (same material and contact area) working and counter electrodes (WE and CE), of which one was connected to ground together with the electron analyzer (see also Chapter 2.1.1). The applied voltage is screened by the counterions of the IL through the formation of EDLs at

both IL/electrode interfaces. Hence, the potential of the IL, that is, all core levels and the vacuum level, shifts by the amount of PS at the grounded electrode; see Figure 22b.
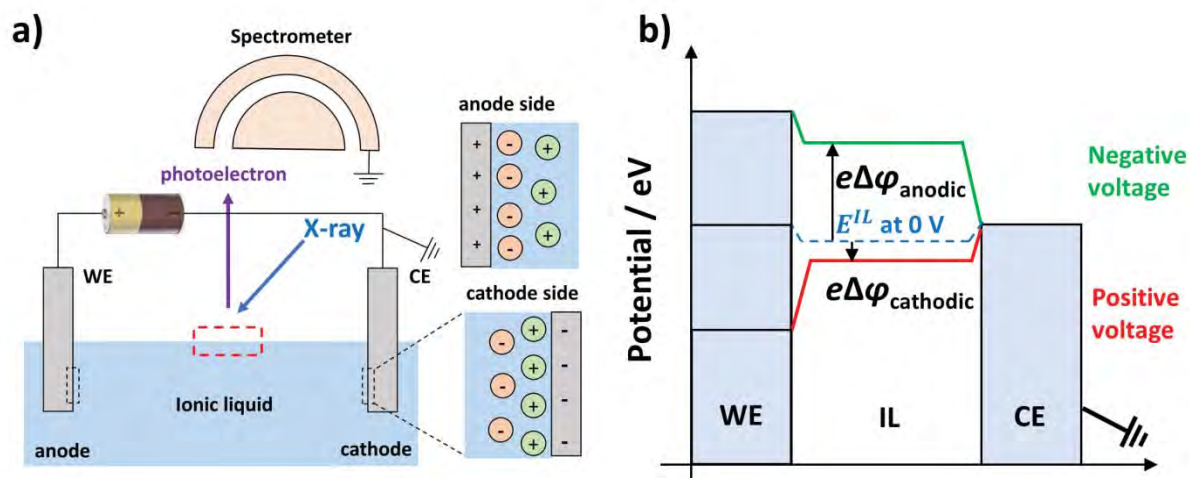
Figure 22 a) Schematic figure of our experimental setup and the charged interfaces with the CE grounded. b) Potential diagram of IL and electrodes with an applied positive (red) or negative (green) potential. The potential drops at the WE/IL and CE/IL interfaces are indicated as Δφ$_{anodic}$ and Δφ$_{cathodic}$, respectively, according to the polarity of the electrodes.

In the following, we first discuss a typical measurement using the example of [C$_8$C$_1$Im][Tf$_2$N] with Pt electrodes, to explain our experimental approach in more detail. Thereafter, in Chapter 3.4 we present the data for all systems studied along with a detailed discussion.

The XP spectra were measured once the PS reached a steady-state, as verified by chronoamperometry (CA) measurements. As shown in Figure 23 for constant $U_{applied}$ steps of 0 V, −1 V and −2 V, the charging currents decrease rapidly to zero within the first second, which indicates that already after this time, the EDL is formed under non-faradaic conditions to screen the potential in a steady state. For larger applied voltages (−3 V and −4 V in Figure 23), the current change mainly takes place within the first minute. XP spectra were thus recorded after at least one minute waiting time. Note that the remaining currents even after 140 s indicate a faradaic situation for the voltage values of −3 and −4V in Figure 23.

The measured binding energy (*BE*) of the IL XPS peaks is defined based on the usual convention as:

$$BE = h\nu - KE^{SP} - \phi^{SP}$$

where $h\nu$ is the photon energy and KE^{SP} is the electron kinetic energy at the spectrometer with the work function (ϕ^{SP}). With the CE grounded, BE is affected by the vacuum level of the IL and thus the amount of PS $\Delta\varphi^{CE/IL}$ between CE and IL can be determined by the BE shift (ΔBE):

$$\Delta BE = e\Delta\varphi^{CE/IL}$$

Detailed relations are described in Chapter 2.1.1.
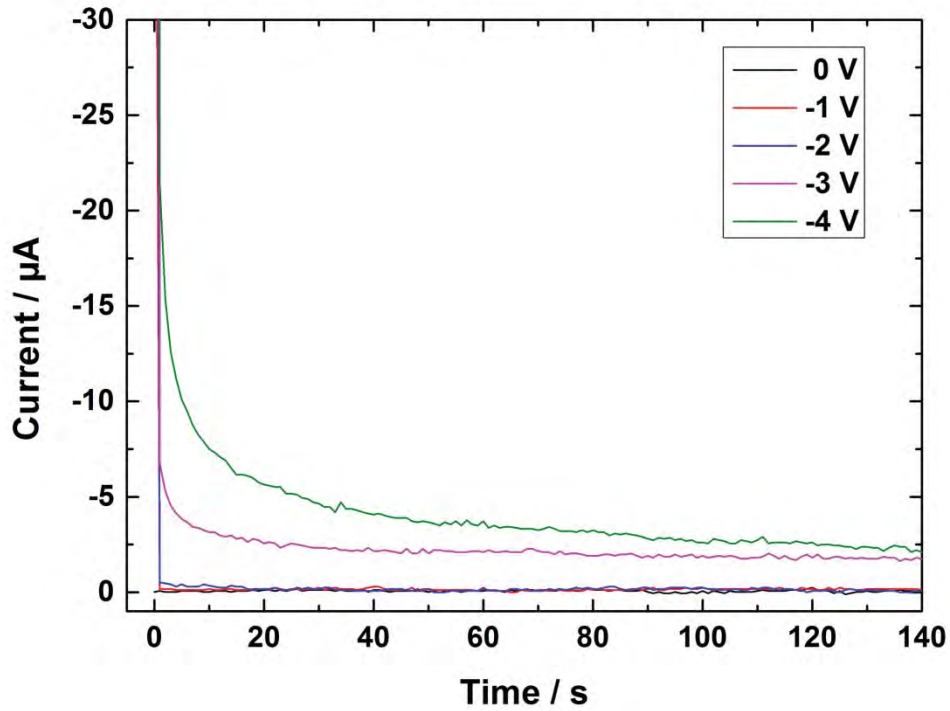
Figure 23 Current between Pt electrodes in [C₈C₁Im][Tf₂N] with a constant applied potential.

Figure 24 (top) shows the F 1s spectra of $[C_8C_1Im][Tf_2N]$ for different voltages applied between two Pt electrodes with the CE grounded. For 0 V, the F 1s peak is observed at 688.85 (±0.05) eV. When +2 V is applied to the WE, the F 1s signal shifts to larger BE by $\Delta BE = 0.55$ eV. This shift is due to the fact that for a positive $U_{applied}$ at the WE, the CE is charged negatively, and the potential of the IL decreases by the amount of screening, which is induced at the CE/IL (cathode) interface.

Consequently, ΔBE indicates the amount of PS at the cathode/IL interface. At −2 V, the F 1s peak is shifted to lower BE by $\Delta BE = -1.45$ eV. With a negative $U_{applied}$, the CE is charged positively and the BE shifts by the amount of PS at the CE/IL (anode) interface, defined as "anodic voltage" ($\Delta\varphi_{anodic}$). Notably, charging effects due to X-ray irradiation were negligible (< 0.05 eV for 3000 s), as expected from a previous study.[101]
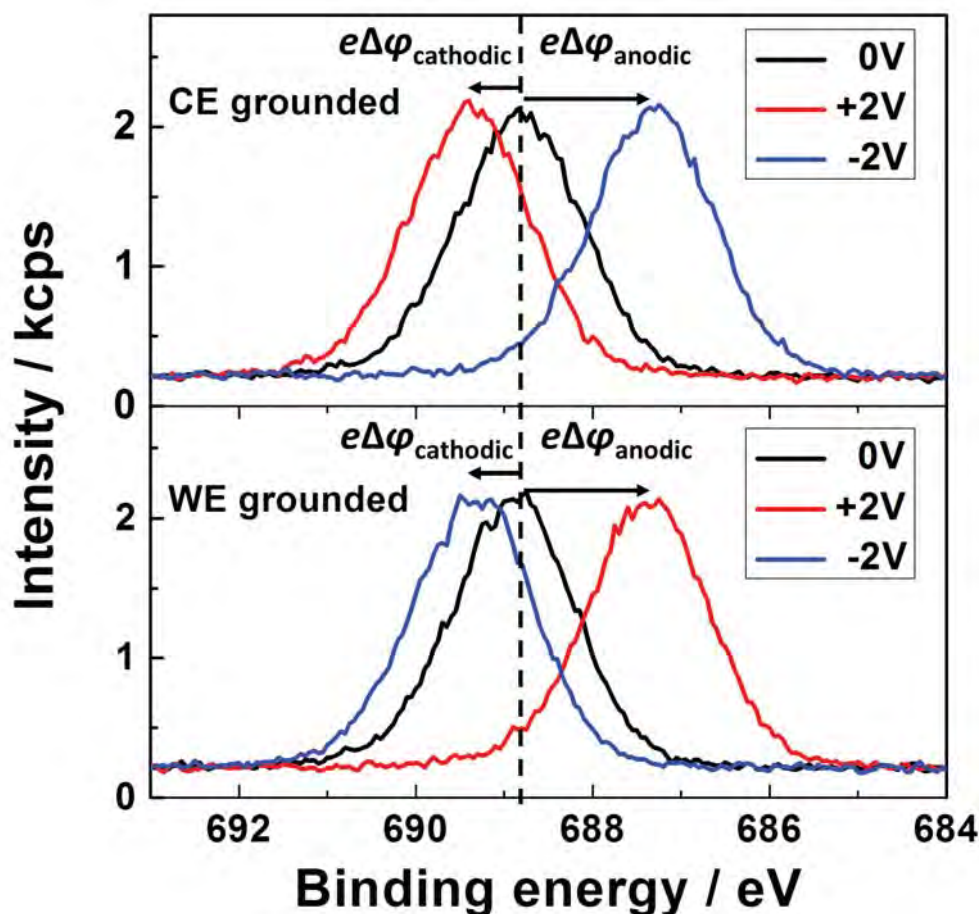
Figure 24 F 1s XP spectra of [C₈C₁Im][Tf₂N] with two identical Pt electrodes.

Within the electrochemical window of the IL, the applied voltage is completely screened at the two IL/electrode interfaces: no voltage drop occurs in the bulk of the IL, which was verified by chronoamperometry, potential sweep measurements, and BE measurements at different XPS probing positions and with electrodes of different sizes (Figure 23 and Figures A2-A11 in Appendix). Furthermore, no shifts or broadening of IL XPS core levels caused by an ohmic potential drop were found. Therefore, $\Delta\varphi_{anodic}$ can be directly converted to $\Delta\varphi_{cathodic}$

and *vice versa* because the applied voltage is identical to the sum of the two ($U_{applied} = \Delta\varphi_{cathodic} + \Delta\varphi_{anodic}$).

When the WE is grounded instead of the CE, the F 1s peak shifts as the amount of the PS at the WE, not at the CE; see Figure 24 (bottom). Therefore, ΔBE indicates $\Delta\varphi_{anodic}$ for a positive $U_{applied}$ and $\Delta\varphi_{cathodic}$ for a negative $U_{applied}$.

Figure 25 shows ΔBE vs $U_{applied}$ with counter (black) and working (red) Pt electrodes grounded.
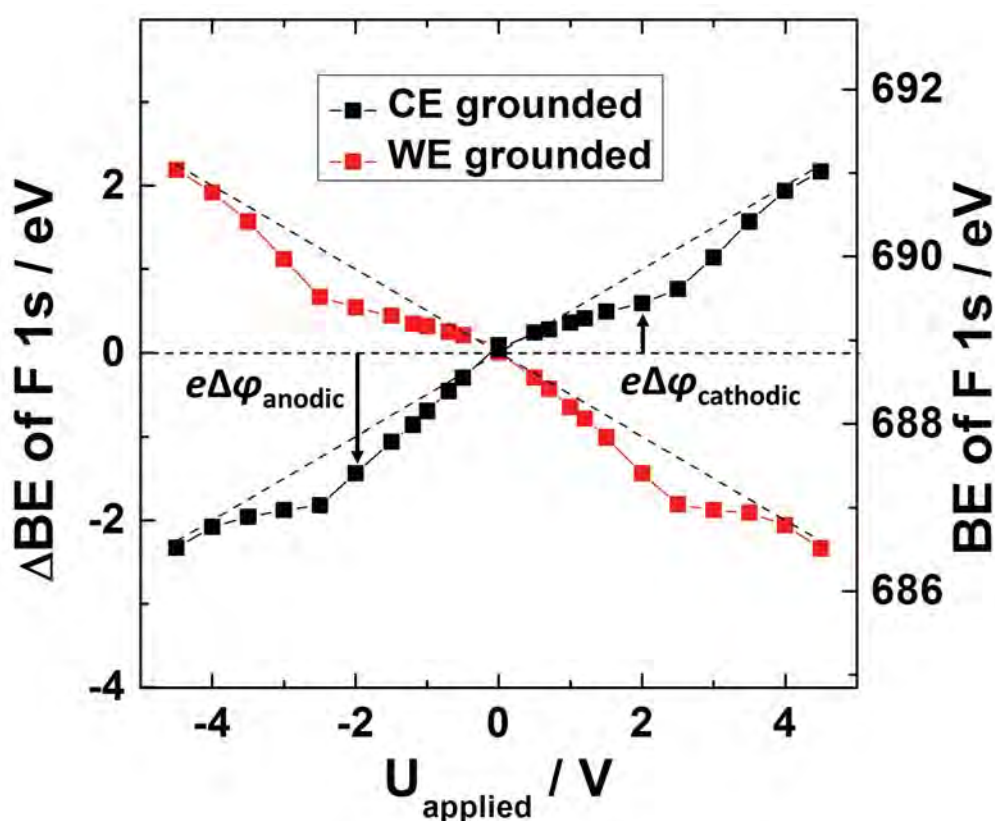
Figure 25 ΔBE of the F 1s peak of [C₈C₁Im][Tf₂N] vs applied potential with CE grounded (black) and WE grounded (red). The ideal lines for equal potential screening at the anode/cathode interfaces are indicated as dashed straight lines (±0.5 eV/V).

For identical PS at both electrodes, defined as "ideal case", the voltage drop at each electrode/IL interface would be half of $U_{applied}$ and the F 1s peak would shift by half of $U_{applied}$. This ideal shift is plotted as dashed straight lines with ±0.5 eV/V slopes. From −3 to +3 V, ΔBE shows considerable deviations from the ideal line towards lower *BE*s, which indicates

34

that for the IL/Pt interface $\Delta\varphi_{anodic}$ is larger than $\Delta\varphi_{cathodic}$. We attribute this asymmetric PS to the asymmetric structure/interaction of the EDL at the anode and cathode.

3.4. Results and Discussion

To elucidate the PS behavior in ILs, we systemically studied the interfaces of imidazolium-based ILs and $[C_4C_1Pyrr][Tf_2N]$ with Pt and Au electrodes (see Table 1 in Chapter 2.3). Figures 26-33 show the XP spectra of one of the core level of the ILs (F 1s XP region for $[C_1C_1Im][Tf_2N]$, $[C_8C_1Im][Tf_2N]$ and $[C_4C_1Pyrr][Tf_2N]$; N 1s XP region for $[C_8C_1Im]Cl$) for $U_{applied} = 0$ V, ±0.5 V, ±0.7 V, ±1.0 V ±1.2 V, ±1.5 V and ±2.0 V. On the left panels, the XP peaks are shown with the CE is grounded while on the right panels with the WE grounded. $\Delta\varphi_{cathodic}$ and $\Delta\varphi_{anodic}$ are indicated in each figure too.

As already emphasized in Chapter 3.3, $U_{applied}$ is equal to the sum of $\Delta\varphi_{cathodic}$ and $\Delta\varphi_{anodic}$; therefore, $\Delta\varphi_{anodic}$ obtained from the *BE* shifts observed in Figures 26-33 can be converted to $\Delta\varphi_{cathodic}$ ($\Delta\varphi_{cathodic} = U_{applied} - \Delta\varphi_{anodic}$).
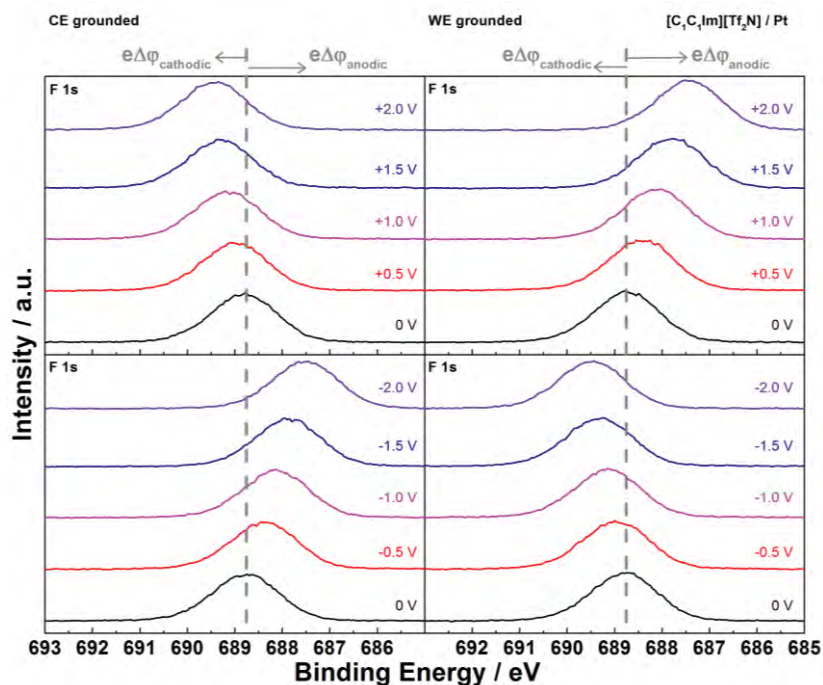
Figure 26 F 1s XP spectra of [C₁C₁Im][Tf₂N] with two identical Pt electrodes for $U_{applied} = 0$ V, ± 0.5 V, ± 0.7 V, ± 1.0 V, ± 1.2 V, ± 1.5 V and ± 2.0 V with CE (left) and WE (right) grounded.
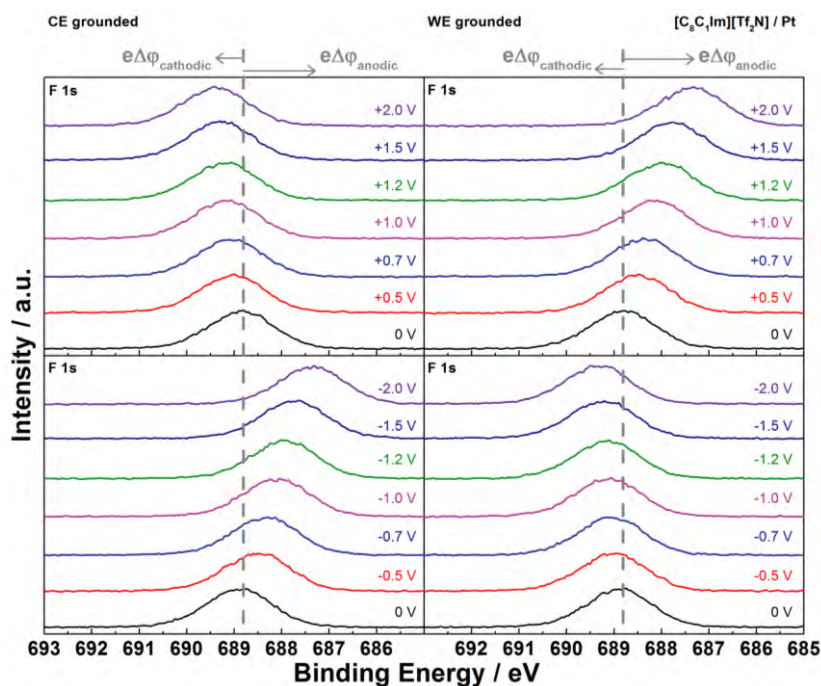
Figure 27 F 1s XP spectra of [C₈C₁Im][Tf₂N] with two identical Pt electrodes for $U_{applied} = 0$ V, ± 0.5 V, ± 0.7 V, ± 1.0 V, ± 1.2 V, ± 1.5 V and ± 2.0 V with CE (left) and WE (right) grounded.
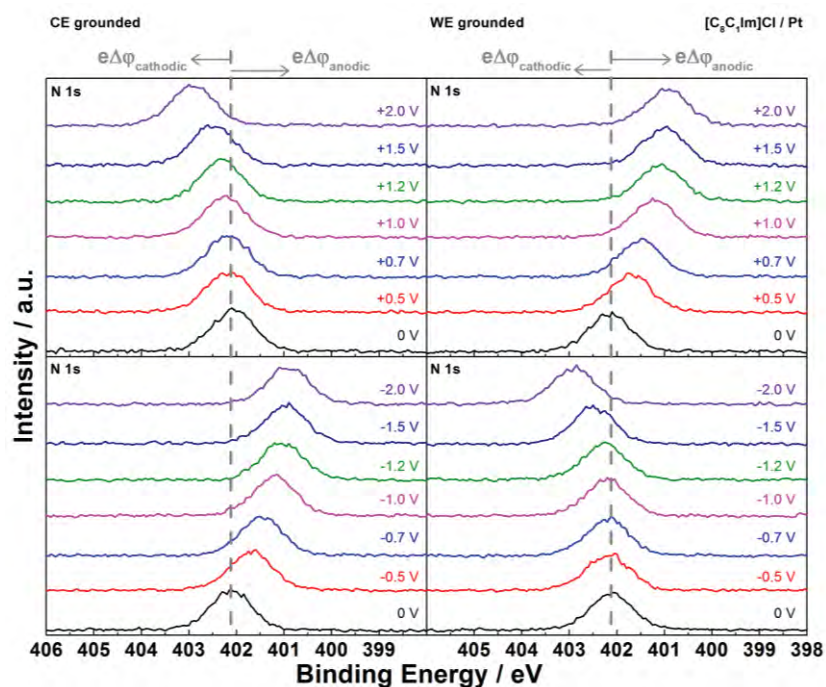
Figure 28 N 1s XP spectra of [C₈C₁Im]Cl with two identical Pt electrodes for $U_{applied} = 0$ V, ± 0.5 V, ± 0.7 V, ± 1.0 V, ± 1.2 V, ± 1.5 V and ± 2.0 V with CE (left) and WE (right) grounded.
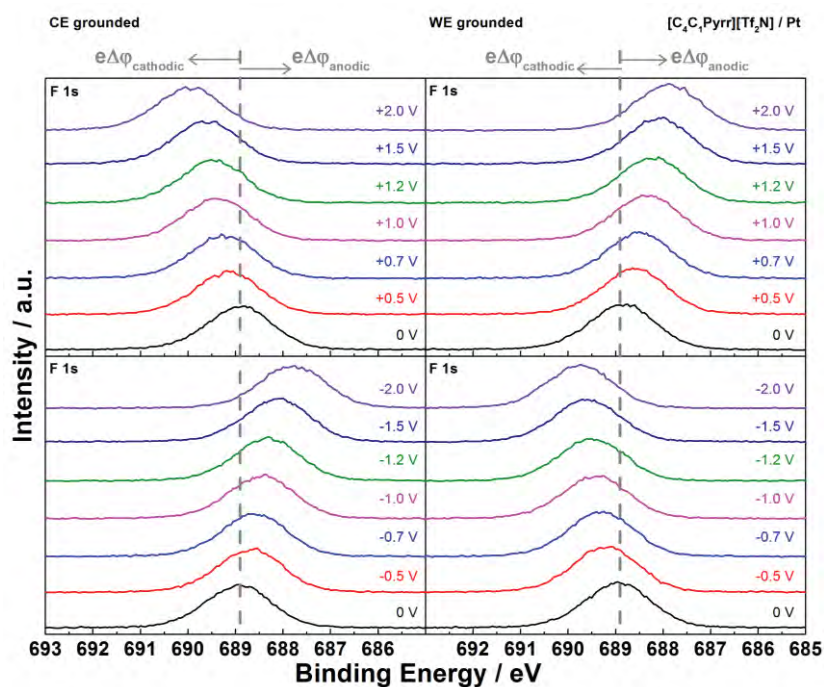
Figure 29 F 1s XP spectra of [C₄C₁Pyrr][Tf₂N] with two identical Pt electrodes for $U_{applied}$ = 0 V, ± 0.5 V, ± 0.7 V, ± 1.0 V, ± 1.2 V, ± 1.5 V and ± 2.0 V with CE (left) and WE (right) grounded.
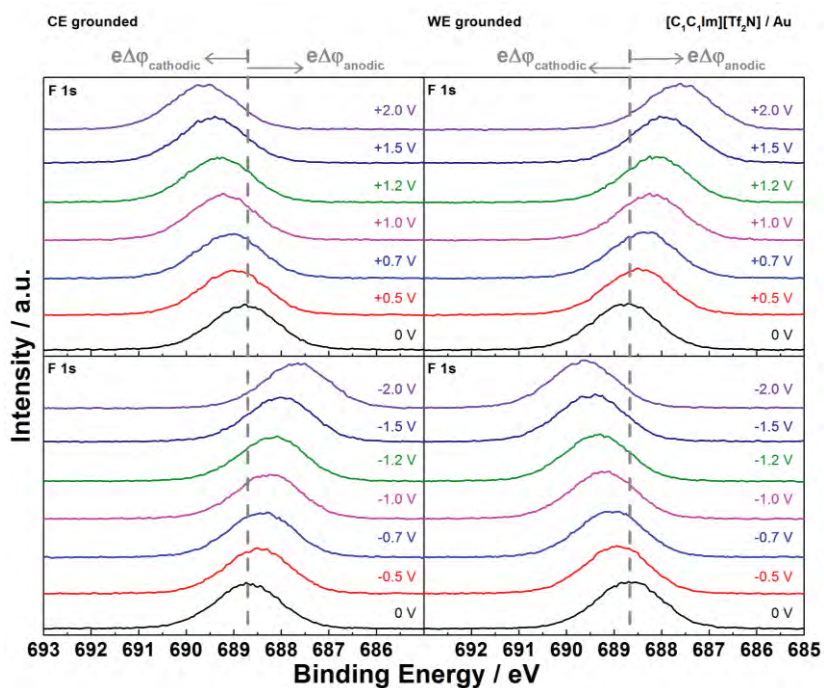
Figure 30 F 1s XP spectra of [C₁C₁Im][Tf₂N] with two identical Au electrodes for $U_{applied}$ = 0 V, ± 0.5 V, ± 0.7 V, ± 1.0 V, ± 1.2 V, ± 1.5 V and ± 2.0 V with CE (left) and WE (right) grounded.
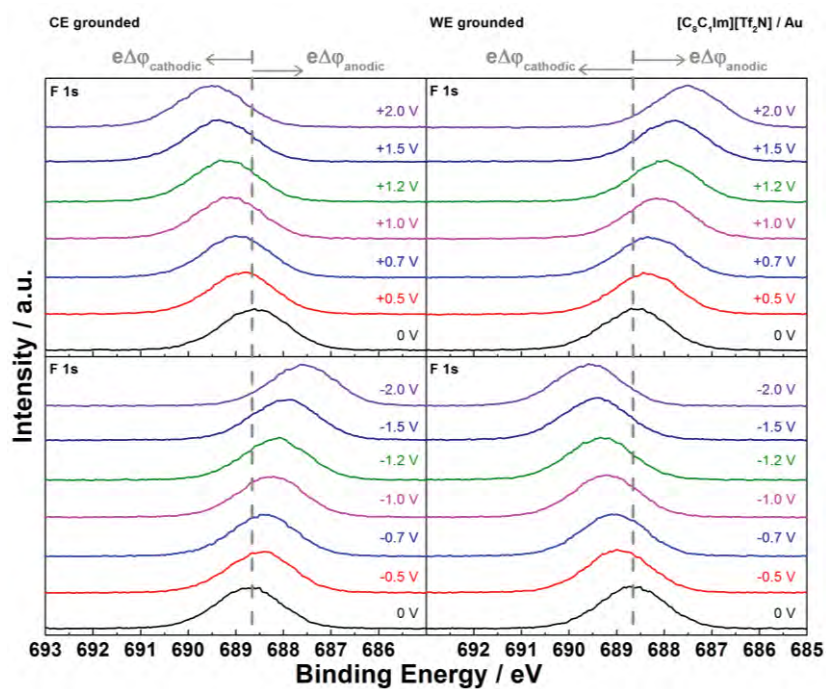
Figure 31 F 1s XP spectra of [C₈C₁Im][Tf₂N] with two identical Au electrodes for $U_{applied} = 0 \ V, \pm 0.5 \ V, \pm 0.7 \ V, \pm 1.0 \ V, \pm 1.2 \ V, \pm 1.5 \ V$ and $\pm 2.0 \ V$ with CE (left) and WE (right) grounded.
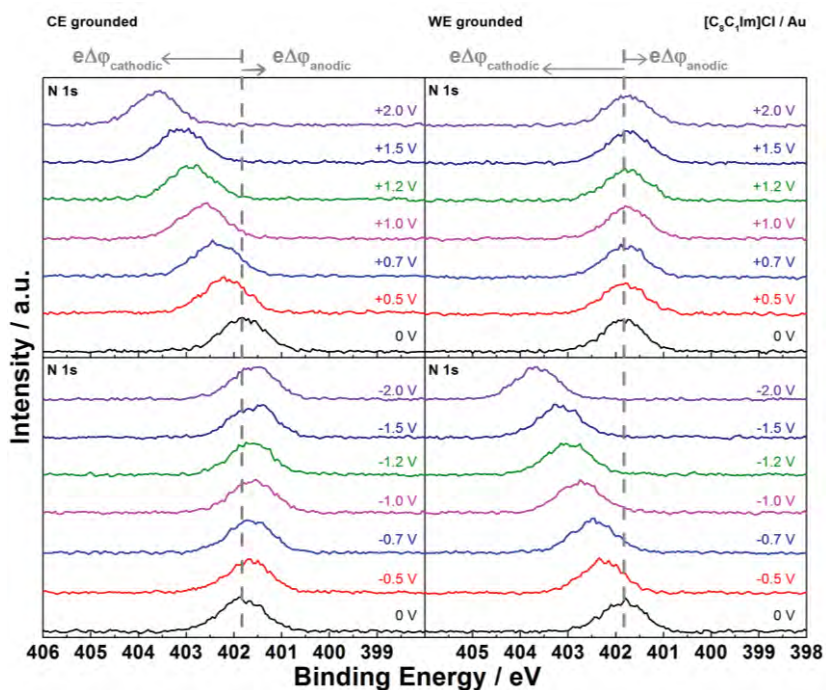
Figure 32 N 1s XP spectra of [C₈C₁Im]Cl with two identical Au electrodes for $U_{applied} = 0 \ V, \pm 0.5 \ V, \pm 0.7 \ V, \pm 1.0 \ V, \pm 1.2 \ V, \pm 1.5 \ V$ and $\pm 2.0 \ V$ with CE (left) and WE (right) grounded.
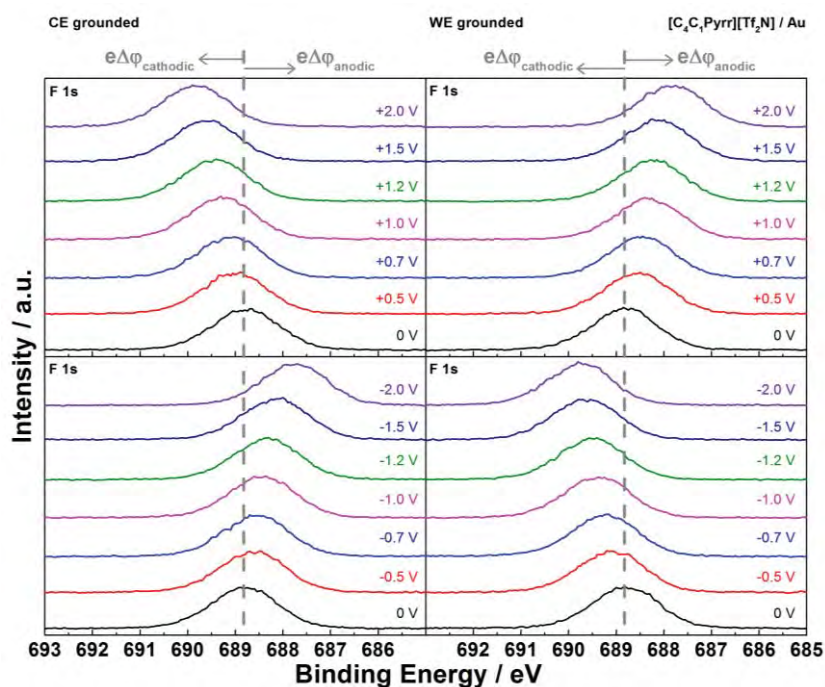
Figure 33 F 1s XP spectra of [C₄C₁Pyrr][Tf₂N] with two identical Au electrodes for
U_applied = 0 V, ±0.5 V, ±0.7 V, ±1.0 V, ±1.2 V, ±1.5 V and ±2.0 V with CE (left) and
WE (right) grounded.

In the following, the averages of $\Delta\varphi_{\text{cathodic}}$ obtained from this conversion are shown in Figure 34 for a clearer presentation; the error bars indicate the standard errors. Note that all measurements were performed within the electrochemical windows of the ILs; see residual currents recorded during XPS and potential sweep measurements in Figures A4-A11 in Appendix.

For Au (Figure 34a), the imidazolium-based ILs with the large [Tf₂N]⁻ anions and [C₄C₁Pyrr][Tf₂N] show within the applied cell voltage range a symmetric behavior, that is, the data for $\Delta\varphi_{\text{cathodic}}$ closely follow the dashed line, with a slope of 0.5 V/V. This indicates similar anodic and cathodic PS for applied voltages from 0 to 2 V. In contrast, [C₈C₁Im]Cl shows a much larger $\Delta\varphi_{\text{cathodic}}$ than $\Delta\varphi_{\text{anodic}}$, as is deduced from a slope of 0.92 V/V. This behavior indicates a highly asymmetric situation, with most of the PS occurring at the cathode while at the anode nearly no changes in PS occur upon applying the voltage. This asymmetry for [C₈C₁Im]Cl can be assigned to the different sizes of anion and cation: in the Helmholtz model, the EDL capacitance is treated as a macroscopic capacitance, which is inversely proportional to the distance between two charged plates. For ILs, the distance between the charged plates

can be assumed as the size of the counterions.[44] Upon charging the anode more positively by increasing the applied voltage, the additional smaller Cl^- counterions in the EDLs reside in a smaller distance d at the anode compared to the situation at the cathode, where the larger $[C_8C_1Im]^+$ counterions compensate the increasing negative charge.
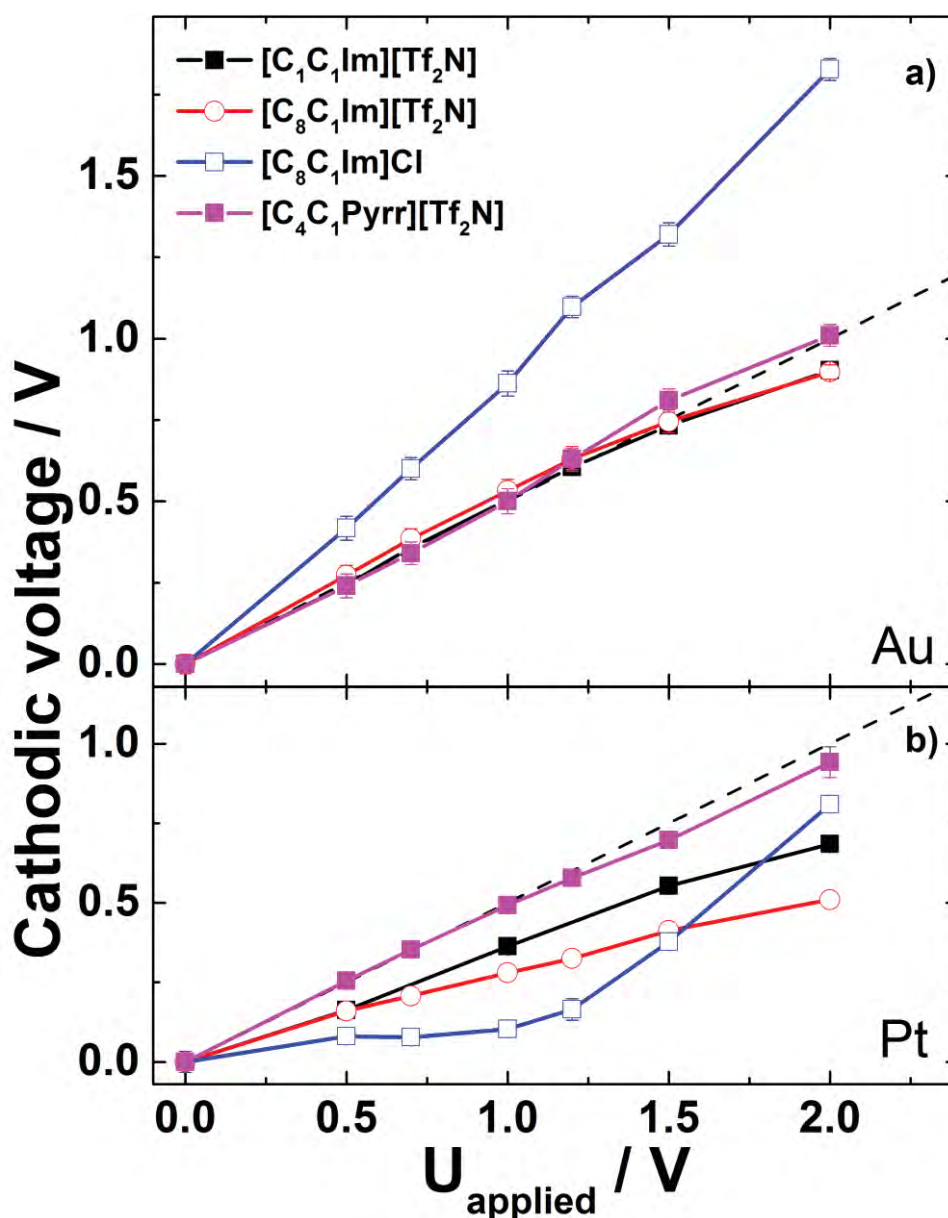
Figure 34 Cathodic voltage of various ILs vs $U_{applied}$. The ideal lines for equal poten-tial drops at the anode/cathode interfaces are indicated as dashed straight lines (+0.5 V/V). a) Au/Au electrodes. b) Pt/Pt electrodes.

Hence, considering the identical contact area A of both electrodes and assuming an identical DC permittivity ε, the corresponding capacitance ($C = \varepsilon_0 \varepsilon A/d$) of the EDL at the anode (C_{anodic}) is larger than that of the EDL at the cathode ($C_{cathodic}$).

Note that in this simple Helmholtz approximation, effects related to differences in ε, multilayer formation ("crowding"), excess charge overcompensation in the next layers ("over-screening"), diffusive layer profiles, charge transfer reactions between metal and adsorbed ions, ion polarization effects at the interface, etc.[44] are neglected.[51] The resulting small $\Delta\varphi_{anodic}$ ($\sim 1/C_{anodic}$) consequently leads to a larger value for $\Delta\varphi_{cathodic}$ ($= U_{applied} - \Delta\varphi_{anodic}$). Note again that the simplified relation $\Delta\varphi \sim d$ only holds because the contact areas of anode and cathode are identical in our cell setup. For $[C_1C_1Im][Tf_2N]$, $[C_8C_1Im][Tf_2N]$, and $[C_4C_1Pyrr][Tf_2N]$, the size of $[Tf_2N]^-$ is similar to that of $[C_nC_1Im]^+$ and $[C_4C_1Pyrr]^+$, and therefore the PS at the cathode and anode side are similar for these ILs.

The situation is very different for Pt electrodes as shown in Figure 34b by the $\Delta\varphi_{cathodic}$ values of all imidazolium-based ILs and $[C_4C_1Pyrr][Tf_2N]$. For applied cell voltages up to 2 V, the $\Delta\varphi_{cathodic}$ curves for all imidazolium-based ILs are located below the ideal line, with initial slopes of 0.27, 0.35 and 0.12 V/V for $[C_8C_1Im][Tf_2N]$, $[C_1C_1Im][Tf_2N]$ and $[C_8C_1Im]Cl$, respectively. While for $[C_8C_1Im][Tf_2N]$ and $[C_1C_1Im][Tf_2N]$ the slope remains unchanged up to 2 V, it strongly increases for $[C_8C_1Im]Cl$ above ~ 1.2 V to a value of 0.81 V/V. The small initial slopes below 0.5 V/V imply that the EDL capacitances at the platinum cathode $C_{cathodic}$ are larger than C_{anodic} for imidazolium-based ILs. We tentatively attribute this behavior to the strong chemical interaction of the imidazolium cation with the platinum surface, most likely between the imidazolium ring π orbital and the Pt 5d orbital, which is much weaker on gold.[102] In the case of $[C_8C_1Im][Tf_2N]$ and $[C_1C_1Im][Tf_2N]$, the slopes of 0.27 and 0.35 V/V thus reflect the smaller distance $d_{cathodic}$ (and thus larger $C_{cathodic}$) of the flat-lying imidazolium rings of the additional $[C_nC_1Im]^+$ counterions at the charged cathode compared to the more bulky $[Tf_2N]^-$ counterions at the anode. In the case of neat $[C_8C_1Im]Cl$ with its very small anion, the observed $\Delta\varphi_{cathodic}$ slope of 0.12 V/V (that is, $C_{cathodic} \gg C_{anodic}$) cannot be simply explained by differences in d, since the size of Cl^- counterions and the vertical extension of a flat-lying imidazolium ring are quite comparable. The situation is complicated by the fact that at applied cell voltages above 1.2 V, the slope of the $\Delta\varphi_{cathodic}$ curve of $[C_8C_1Im]Cl$ considerably changes from 0.12 V/V close to 0.81 V/V, similar to the case for $[C_8C_1Im]Cl$ on gold over the whole cell voltage window. Thus, our simplified description is

not sufficient anymore to explain the observed effects. A detailed understanding requires density functional theory calculations describing the chemical interactions of the IL with the metal surface accurately. These are, however, out of the scope of this work. For $[C_4C_1Pyrr][Tf_2N]$, the $\Delta\varphi_{cathodic}$ values nearly coincide with the ideal line (slope of 0.5 V/V), and thus are similar to $\Delta\varphi_{anodic}$, which is in line with the absence of specific π orbital interactions of the non-aromatic $[C_4C_1Pyrr]^+$ cation with the Pt electrodes.

It is important to emphasize here that the observed large asymmetric PS effects described above cannot be related to our choice of offset (that is, the subtraction of the measured IL *BE* at zero applied voltage to obtain the cathodic voltage curves shown in Figure 34), which was carefully checked by measuring *BE* positions with respect to each other with zero applied voltage between the Pt and Au electrodes. Notably, the very similar F 1s and N 1s *BE* values within ± 0.08 eV indicate for all ILs very similar initial charging and consequently PS at zero applied voltage (see Table 6).

Table 6 F 1s (or N 1s) peak position of various ILs at 0 V applied.

IL	BE with Pt electrodes (eV)	BE with Au electrodes (eV)
$[C_1C_1Im][Tf_2N]$	688.76	688.77
$[C_8C_1Im][Tf_2N]$	688.81	688.66
$[C_8C_1Im]Cl$	402.12	401.83
$[C_4C_1Pyrr][Tf_2N]$	688.91	688.83

Though a considerable number of experimental and modeling studies on the structures at the IL/solid interface already exist, the thickness of the EDL at the IL/electrode interface is still debated.[44] Recent sum-frequency generation [103] and nuclear magnetic resonance [64] results suggest that the counterions are localized in the first monolayer in contact with the charged surface. Within the IL electrochemical window, we found that the magnitude of PS strongly depends on the electrode material and the nature of the IL counterion, which strongly supports our interpretation that the observed PS is mainly governed by a single monolayer of counterions close to the electrode and not by counterions in multilayers.

For voltages around ±2.5 V and above, the deviation of *ΔBE* from the ideal line behavior starts to decrease for all studied ILs (Figure 25 and Figures A4-A11 in Appendix) indicating equivalent PS on anode and cathode at high $U_{applied}$. One possible explanation is that around ±2.5 V, the amount of counterions in the EDL starts to exceed the coverage of one monolayer and thus PS at higher voltage is then achieved by the counterions in multilayers. Likely, these further layers are not strongly influenced by the specific IL/electrode interaction, and thus the PS on anode and cathode becomes similar. With a simple estimation based on a plate capacitor model, the amount of excess counterions at the IL/electrode interface can be roughly estimated as follow:

$$\rho = \frac{n}{A} = \frac{Q}{A * e} = \frac{C * V}{A * e} = \frac{\varepsilon * \varepsilon_0 * A}{d} * \frac{V}{A * e} = \frac{V * \varepsilon * \varepsilon_0}{e * d}$$

where ρ is the number density of excess charges (cm^{-2}), V is the PS on the electrode, e is the charge of an electron, d is the distance between two charged plates, ε is the dielectric constant of the IL at the IL/electrode interface, and ε_0 is the vacuum permittivity. Here we assume the distance between plates as the size of ions (0.5 nm) and the dielectric constant of the IL as 5.[44] According to this simple estimation, 5.5×10^{13} cm^{-2} excess counterions are needed to screen 1 V. This estimated value in comparison with a surface density of 8.6×10^{13} ion pairs cm^{-2} of [C$_8$C$_1$Im][Tf$_2$N] reported in literature, constitutes 0.6 monolayer of IL.[104] This estimation shows that at 3 V the number of excess ions on the electrode roughly corresponds to 2 ML of IL, which supports our argument about the multilayer contribution at higher voltages.

While experimental studies of the PS under equilibrium conditions are scarce, asymmetric PS for the IL/electrode interfaces has been reported by molecular dynamics simulations.[12,66] For example, the simulation for [C$_2$C$_1$Im][SCN] on a graphene electrode shows a smaller cathodic voltage, as is observed here.[20]

3.5.   Conclusions

In this chapter, we introduced a new approach to investigate the PS at various IL/electrode interfaces using *BE* shifts in *in situ* XPS measurements. We studied a variety of different ILs using a two-electrode electrochemical cell with either identical Pt or Au electrodes. In the case of imidazolium-based ILs and Pt electrodes, the PS at the anode is larger than at the cathode, which is attributed to strong interactions via specific adsorption of the imidazolium cations at

Pt. In contrast, for Au electrodes in the absence of specific adsorption, no significant asymmetry is observed. Furthermore, the PS is affected by the thicknesses of the EDLs, as is deduced from pronounced differences for small and large anions. Our results imply that at voltages up to ~2 V the PS in ILs mainly occurs by counterions in the monolayer range on the electrode; only at higher voltages multilayers contribute. We are convinced that our approach provides a new route towards studying chemical interactions between ILs and electrodes as it will be demonstrated in the next chapter.

4.   Electrode / Binary Ionic Liquid Mixtures Interfaces

The content of this chapter is based and adapted from the following publication:[105]

4.1.   Introduction

As pointed out in Chapter 1, the interest in ILs as solvent-free electrolytes has grown over time due to their large electrochemical window (3.5 - 4.0 V), thermal stability, low vapor pressure, and the tunability of their physicochemical properties by choosing certain anion-cation combinations. Recently, IL mixtures have received considerable attention as an additional route to tune the properties of ILs for various applications. For example, the employment of mixtures of $[BF_4]^-$ and $[Tf_2N]^-$ with 1-ethyl-3-methylimidazolium ($[C_2C_1Im]^+$) as common cation led to symmetric charge storage at the two identical electrodes of a capacitor, which resulted in an expanded operating potential window.[30] An IL mixture of tetramethylammonium ($[TMA]^+$) and $[C_2C_1Im]^+$ with $[BF_4]^-$ as common anion on mesoporous carbon electrodes exhibited enhanced power and energy densities. These enhancements were attributed to strong cation-cation interactions between $[TMA]^+$ and $[C_2C_1Im]^+$.[31] Another application field is fuel cells where binary mixtures of protic ILs exhibited higher activity for hydrogen oxidation and oxygen reduction at the electrodes compared to the neat ILs and this improvement was attributed to an enhanced proton transfer reaction.[106]

The behavior of IL mixtures at charged interfaces is thus relevant to design and develop devices for various electrochemical applications. In this context, experimental and theoretical studies have been employed to achieve a better understanding of the electrical double layer (EDL) at IL mixtures-electrode interfaces.[107-114]

The identification of chemical species at the IL mixtures/electrode interface is, however, difficult to assess directly. A very powerful method in this context is ultra-high vacuum (UHV)-based angle-resolved XPS, which however can be applied only for ultrathin IL films, due to the limited escape depth of the emitted photoelectrons on the order of a few nm.[115] Using this method, ultrathin layers of IL mixtures have been investigated.[116, 117] It was found that typically specific cations or anions of the mixture are arranged in a checkerboard structure. Upon successive deposition of individual layers of two different ILs, exchange processes take place which are driven by the interaction strength of the specific ILs with the substrate, yielding interface enrichment effects. The question arises, whether such effects are only occurring in ultrathin films or also in a thicker IL film (larger than 10 nm) on the electrode of an electrochemical cell. Under the latter conditions, angle resolved XPS cannot be directly used to study the chemical composition of the interface, due to limited electron escape depth.

Based on our potential screening (PS) experiments in the case of neat ILs using *in situ* XPS (Chapter 3), we now propose a new approach to indirectly deduce which IL ions are preferentially present at the interface in IL mixtures at applied potentials within the electrochemical stability window (again, as confirmed by chronoamperometry, see Figure A12 in Appendix). As already described in Chapter 3, the measurements were also performed with a symmetric two-electrode electrochemical cell setup comprising two wires of identical metal as electrodes with identical contact areas to the electrolyte. At a specific applied cell voltage, $U_{applied}$, the PS at the anode and cathode is determined by the properties of the IL ions at the electrode interfaces. As demonstrated in Chapter 3 and summarized in Figure 35, the change in PS at anode/cathode can be measured through the binding energy shift (ΔBE) of IL-related core level signals at the IL/vacuum interface by XPS. This allows us to assess the PS response at anode/cathode in equilibrium under ultraclean conditions in UHV. Again, we denote the amount of PS relative to $U_{applied} = 0$ V at the anode (plus pole) as $\Delta\varphi_{anodic}$ and that at the cathode (minus pole) as $\Delta\varphi_{cathodic}$.

The very characteristic behavior of $\Delta\varphi_{cathodic}$ curves as a function of $U_{applied}$ for the neat ILs in contact with different electrodes as discussed in Chapter 3 will now be considered as a "fingerprint" signature for certain IL/electrode combinations. The observed characteristics of the curves, that is, symmetric or asymmetric PS at cathode and anode, along with intermediate behavior, reflect the ionic moieties in contact with the respective electrode and therefore the composition and structure of the EDL.

46
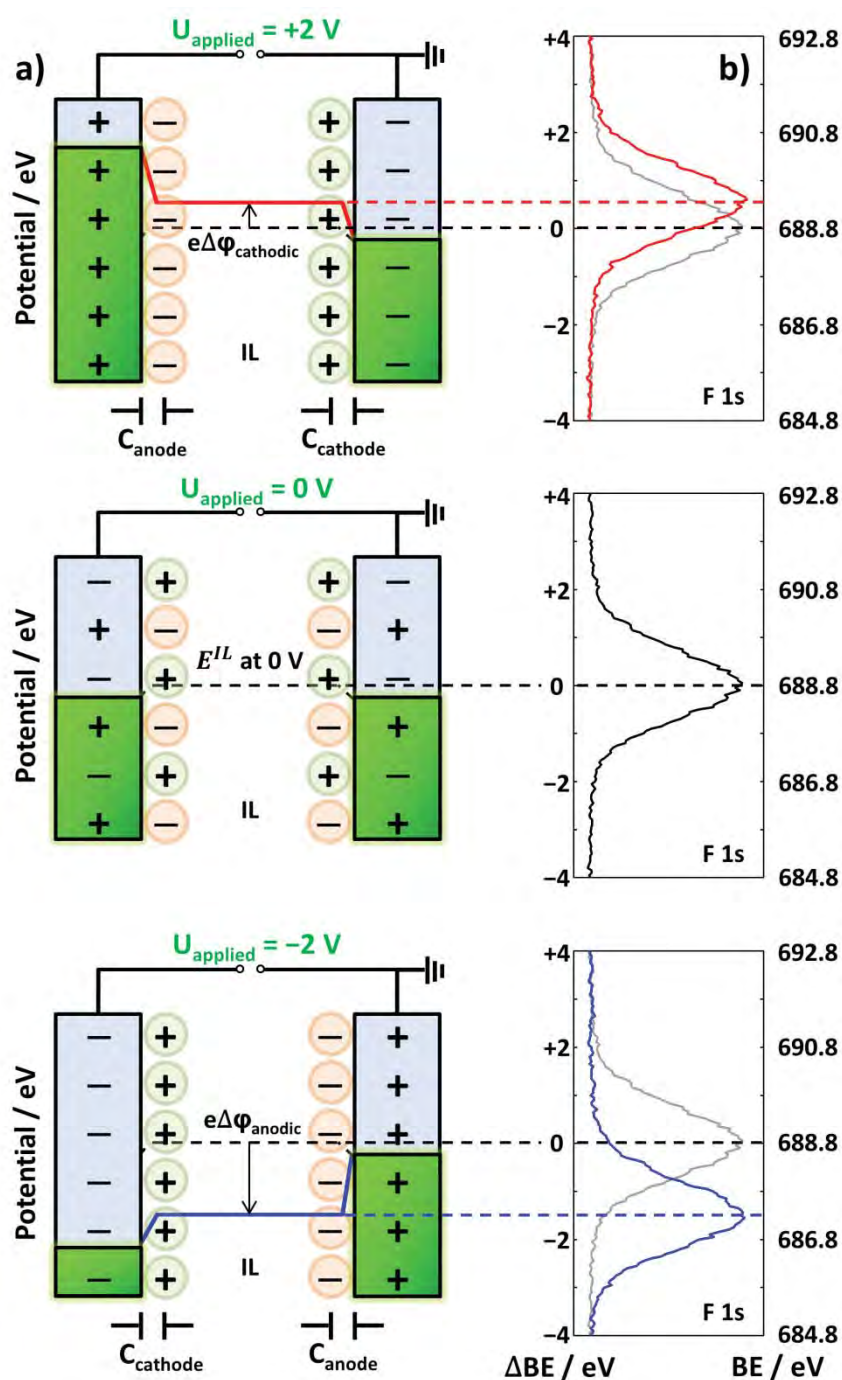
Figure 35 (a) Schematic sketches of the potentials at the IL electrode interfaces and the structure of the EDL, for the electrochemical cell with two Pt electrodes in contact with neat [C$_8$C$_1$Im][Tf$_2$N]. The capacitances at the cathode and anode interfaces are indicated as C$_{cathode}$ and C$_{anode}$, respectively (note that for zero applied cell voltage (center), the number of anions and cations at the interface may not be exactly equal). (b) XPS spectra of the F 1s region according to U$_{applied}$. The XPS spectrum at 0 V is shown in gray as a reference in the +2 V and −2 V spectra. The potential of the IL (E^{IL}) and the binding energy of F 1s at each applied voltage are indicated by dashed lines.

Notably, our method does not allow for determining the specific adsorption geometry of the ions. The idea of the present study rather is to use this fingerprint-type behavior to determine the nature of the IL/electrode interface in mixtures of two ILs A and B, with the same cation. If the mixture shows the identical behavior as IL A, then one can conclude that the interface is dominated by the respective ions of IL A, and if the mixture shows the identical behavior as IL B, the one can conclude that the interface is dominated by the respective ions of IL B. A behavior between that of A and B reflects that the interface contains a mixture of the ions of both ILs.

As already emphasized in Chapter 3, the structure of EDLs is determined by the interactions of the IL cations and anions with the metal surface, which depend on their size, orientation, chemical structure as well as the chemical nature of the electrode. For different IL mixtures, it has been shown by XPS studies of ultrathin layers that typically the ions with the stronger bond to the metal surface preferentially are in direct contact with the substrate while the less-interacting ions of the same polarity are less present at the interface. While the situation for a specific IL at the IL/electrode interface in an electrochemical cell is not necessarily the same due to ions in the second and further layers, the general conclusion should also hold qualitatively at least.

4.2.   Methods and Materials

The PS measurements were performed in the UHV-compatible electrochemical cell developed by our group.[94] The cell consists of two identical metallic electrode wires (electrically isolated by polytetrafluoroethylene spacers) and a molybdenum sample holder, in which the IL is filled (see Chapter 2.2). The distance between the wires was 5 mm. The electrodes are connected to the potentiostat (Keithley 2450) through two contact springs located at the head of the manipulator. The pure Pt (99.99 %) and Au (99.995 %) wires with a diameter of 0.30 and 0.25 mm, respectively, were cleaned by flame-annealing. The synthesis of ultraclean $[C_8C_1Im][Tf_2N]$ and $[C_8C_1Im]Cl$ was carried out as described in a previous publication.[91] All the IL mixtures were prepared by mixing two ILs with the required mass ratio to achieve the reported molar concentration without the use of co-solvents. The mixtures were sonicated for 1 hour at around 60 °C for homogenous mixing. The molar ratio of the two components of the mixtures was confirmed by XPS quantitative analysis (Tables A1-A15 in Appendix). All the

electrodes were carefully placed in the electrochemical cells in order to have identical contact areas (±5 %) with the IL mixtures.

To determine the potential screening at the electrodes, XPS spectra were measured in our DASSA setup using the monochromatic Al K_α source and a hemispherical analyzer (detection of photoelectrons in normal emission) with an overall energy resolution of 0.4 eV.[90] Data were collected in the F 1s or N 1s regions, due to the strong signal intensities of the corresponding peaks. During XPS, one of the electrodes was grounded through a corresponding connector at the front panel of the source meter. All XPS measurements were performed at non-faradaic conditions, which was confirmed by chronoamperometry (Figure A12 in Appendix) using the Keithley 2450 source meter. In addition, we can rule out the production of volatile species such as Cl_2 formed by Cl^- oxidation at the anode side in our two-electrode electrochemical cell within the applied voltage window from 0 - 2 V since the resulting formation of Cl_2 should lead to a measurable pressure increase in the UHV chamber (base pressure of 5×10^{-10} mbar), which was not observed.

4.3. Results and Discussion

4.3.1. Binary Ionic Liquid Mixtures on Au Electrodes

To study the competition of two different anions in the PS at the IL/electrode interface, we prepared various IL mixtures with $[C_8C_1Im]^+$ as a common cation, and $[Tf_2N]^-$ and Cl^- as anions, namely $[C_8C_1Im][Tf_2N]_xCl_{1-x}$. Figure 36 shows a comparison of the PS curves of neat $[C_8C_1Im][Tf_2N]$ and neat $[C_8C_1Im]Cl$ (presented in Chapter 3) with their mixtures on Au electrodes.

As already discussed in Chapter 3, neat $[C_8C_1Im][Tf_2N]$ (x = 1, red squares) shows from 0 V to 2 V a symmetric behavior ($\Delta\varphi_{cathodic} = \Delta\varphi_{anodic}$) with a slope of 0.5 V/V. In contrast, the PS curve of neat $[C_8C_1Im]Cl$ (x = 0, blue squares) exhibits a highly asymmetric situation ($\Delta\varphi_{cathodic} \gg \Delta\varphi_{anodic}$) with a slope of 0.92 V/V. In Chapter 3, we have assigned this asymmetry for $[C_8C_1Im]Cl$ mainly to the different sizes of anion and cation. The smaller Cl^- counterions in EDL reside in a smaller distance (d_{anode}) at the anode compared to the larger distance ($d_{cathode}$) of $[C_8C_1Im]^+$ at the cathode. Hence, in a simple Helmholtz approximation, assuming an identical DC permittivity ε and considering the identical contact area A of both

electrodes, the corresponding capacitance ($C = \varepsilon_0 \varepsilon A/d$) of the EDL at the anode (C_{anodic}) is larger than that of the EDL at the cathode ($C_{cathodic}$). The resulting small $\Delta\varphi_{anodic}$ ($\sim d_{anode}$) consequently leads to a larger value for $\Delta\varphi_{cathodic}$ ($= U_{applied} - \Delta\varphi_{anodic}$). For neat $[C_8C_1Im][Tf_2N]$, the sizes of $[Tf_2N]^-$ and $[C_8C_1Im]^+$ are similar ($d_{anode} \approx d_{cathode}$), and therefore the PS at the cathode and anode side are similar for this IL.
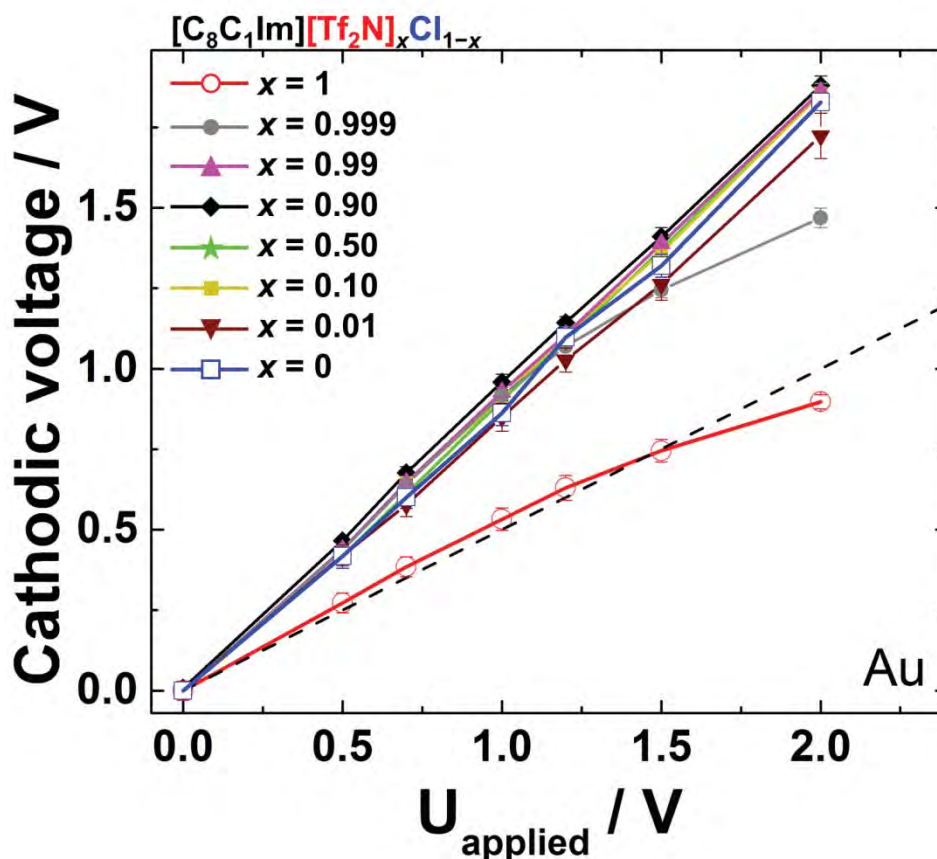
Figure 36 Cathodic voltage of various $[C_8C_1Im][Tf_2N]_xCl_{1-x}$ mixtures versus applied voltage with x = 1, 0.999, 0.99, 0.9, 0.5, 0.1, 0.01 and 0, for Au electrodes. The ideal line for equal potential drops at the anode and cathode interfaces is indicated as dashed straight lines with a slope of +0.5 V/V. The error bars show standard deviations of the measurements.

To investigate which ions are adsorbed on the electrode in IL mixtures, we selected a number of different $[C_8C_1Im][Tf_2N]_xCl_{1-x}$ mixtures, with x = 0.01, 0.1, 0.5, 0.9, 0.99 and 0.999. Interestingly, up to +1.5 V applied voltage, the $\Delta\varphi_{cathodic}$ curves (and consequently, the $\Delta\varphi_{anodic}$ curves) of all mixtures are virtually identical to that of neat $[C_8C_1Im]Cl$ (Figure 36),

50

even down to only 0.1 mol% content of $[C_8C_1Im]Cl$. This implies that the compositions of the IL/cathode and IL/anode interfaces in the mixtures are the same as for neat $[C_8C_1Im]Cl$. In other words, the Cl^- anions are extremely interface-active and thus, in all $[C_8C_1Im][Tf_2N]_xCl_{1-x}$ mixtures studied here, $[Tf_2N]^-$ obviously is completely replaced from the electrode interfaces by Cl^- at zero applied voltage and up to an applied voltage of 1.5 V. Since the electrode-electrolyte interface region is only a very small fraction (about 10^{-6}) of the total electrolyte volume, even a 0.1 mol% bulk content of $[C_8C_1Im]Cl$ is enough to replace all $[Tf_2N]^-$ anions by Cl^- at the electrodes. This anion replacement initially occurs without voltage and is maintained up to 1.5 V applied cell voltage. We attribute the replacement of $[Tf_2N]^-$ by Cl^- at the Au electrode to a strong attraction (specific adsorption) of Cl^- to the Au surface. Preferential enrichment of Cl^- anions on Au has previously been reported in electrochemical experiments.[118, 119] Our arguments imply that up to an applied voltage of 1.5 V the PS at the Au anode occurs mainly within the first monolayer in contact with the electrode, where the $[C_8C_1Im]^+$ is replaced by Cl^- at the anode, and the Cl^- is replaced by $[C_8C_1Im]^+$ at the cathode.

The pronounced dominance of the $[C_8C_1Im]Cl$-like behavior even for x = 0.99 and 0.999 further indicates a very strong energetic driving force for the enrichment of the Cl^- at the electrodes. The fact that for x = 0.999 the behavior starts to deviate for applied voltages above 1.5 V is tentatively attributed to the very low concentration of Cl^- (x = 0.001) in the IL mixture, as compared to $[Tf_2N]^-$, which starts to play a role at higher voltages, where more anions are required to screen the positive electrode charge.

4.3.2.   Binary Ionic Liquid Mixtures on Pt Electrodes

To study the role of the chemical nature of the electrodes, we compare the PS curves of the same neat ILs as above, $[C_8C_1Im][Tf_2N]$ and $[C_8C_1Im]Cl$, with the PS curves of their mixtures $[C_8C_1Im][Tf_2N]_xCl_{1-x}$ on Pt electrodes; see Figure 37. As already reported in Chapter 3, the $\Delta\varphi_{cathodic}$ curve for $[C_8C_1Im][Tf_2N]$ (x = 1; red squares) is located below the ideal line, with a slope of 0.27 V/V. Notably the slope remains unchanged up to 2 V. The $\Delta\varphi_{cathodic}$ curve for $[C_8C_1Im]Cl$ (x = 0, blue squares) is located below the ideal line too, with an initial slope of 0.12 V/V which strongly increases to a value of 0.81 V/V above ~ 1.2 V.

In Chapter 3, this behavior was attributed to the strong chemical interaction of the imidazolium ring π orbital and the Pt 5d orbital. In this regard, the observed slope of 0.27 V/V for neat $[C_8C_1Im][Tf_2N]$ reflects the smaller distance $d_{cathodic}$ (and thus larger $C_{cathodic}$) of the flat-lying imidazolium rings at the charged cathode compared to the larger $[Tf_2N]^-$ at the anode. In the case of neat $[C_8C_1Im]Cl$ (see Chapter 3 for more details), the interpretation is complicated by the fact that (1) the size of Cl^- counterions and the vertical extension of a flat-lying imidazolium ring are quite comparable ($d_{anode} \approx d_{cathodic}$), therefore the observed $\Delta\varphi_{cathodic}$ slope of 0.12 V/V (that is, $C_{cathodic} >> C_{anodic}$) cannot be simply explained by differences in d and (2) at applied cell voltages above 1.2 V, the slope of the $\Delta\varphi_{cathodic}$ curve of $[C_8C_1Im]Cl$ considerably changes from 0.12 close to 0.81 V/V, similar to the case for $[C_8C_1Im]Cl$ on gold over the whole cell voltage window. Thus, the simplified description adopted for the other IL/electrode combinations is not sufficient anymore to explain the observed effects. Nevertheless and most importantly, the very characteristic and different behavior for the two ILs again can serve as fingerprint for characterizing the IL/electrode composition of the corresponding IL mixtures.
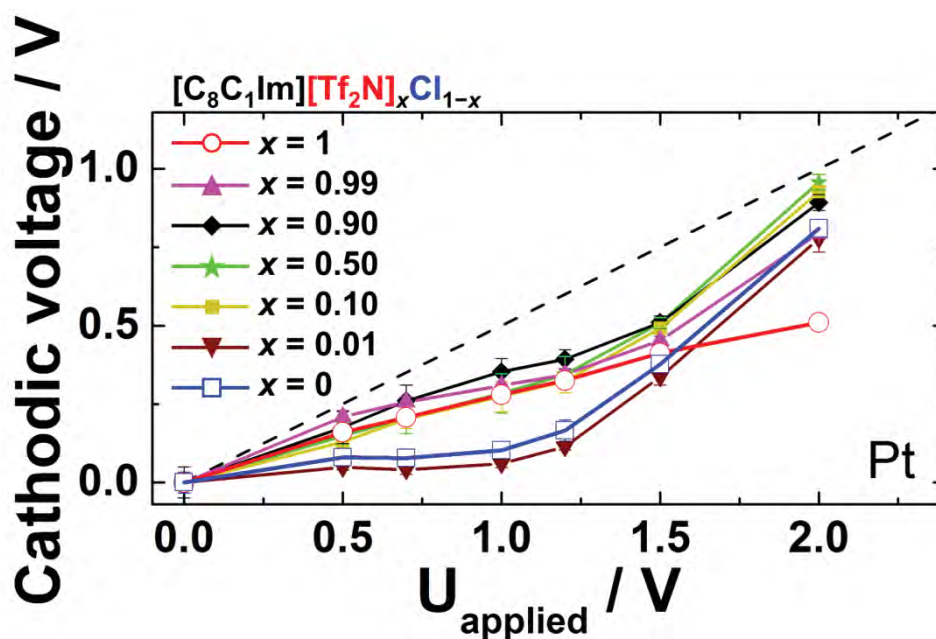
Figure 37 Cathodic voltage of various $[C_8C_1Im][Tf_2N]_xCl_{1-x}$ mixtures versus applied voltage with x = 1, 0.99, 0.9, 0.5, 0.1, 0.01 and 0, for Pt/Pt electrodes. The ideal lines for equal potential drops at the anode and cathode interfaces are indicated as dashed straight lines with a slope of +0.5 V/V. The error bars show standard deviations of the measurements.

For the Pt electrode, $\Delta\varphi_{cathodic}$ curves were measured for $[C_8C_1Im][Tf_2N]_xCl_{1-x}$, mixtures with molar fractions of x = 0.99, 0.9, 0.5, 0.1 and 0.01. Interestingly, from x = 1 down to x = 0.1 (90 mol% Cl$^-$), the behavior at low voltages (up to 1.2 V) shows similar $\Delta\varphi_{cathodic}$ values as neat $[C_8C_1Im][Tf_2N]$, which reflects that from zero applied potential up to 1.2 V, the $[Tf_2N]^-$ ion is selectively enriched at the Pt electrode, as compared to Cl$^-$. The reason for the behavior could be a chemical interaction of the SO$_2$ groups of the $[Tf_2N]^-$ with the platinum electrode which results in specific adsorption of this anion. Only at x = 0.01, a behavior similar to that of $[C_8C_1Im]Cl$ is observed, indicating that at very high Cl$^-$ concentrations, Cl$^-$ starts to dominate the interface behavior.

Again for applied voltages above 1.2 V, the PS behaviors of the mixtures with x = 0.5 and 0.1 divert from that of the neat $[C_8C_1Im][Tf_2N]$ and increase with a similar slope (0.78 V/V) as the $\Delta\varphi_{cathodic}$ curve of the neat $[C_8C_1Im]Cl$ in this applied voltage range. One possible explanation here is that more negative counterions are needed to screen the applied voltage and the packing of the smaller Cl$^-$ anions at the IL-anode interface is apparently easier in this applied voltage range: again, electrostatics seems to win over specific chemical interactions, and thus a similar PS behavior as for the neat $[C_8C_1Im]Cl$ is observed. An alternative explanation for the behavior of the $[C_8C_1Im][Tf_2N]_xCl_{1-x}$ mixtures would be a multilayer EDL model. Up to an applied potential of 1.2 V, also in the mixtures (x = 0.5 and 0.1) only $[Tf_2N]^-$ accumulate in the proximate layer at the IL/Pt interface, due to the strong chemical interaction between $[Tf_2N]^-$ and the Pt electrode.[51, 103, 120-122] Above 1.2 V, the first layer of the EDL at the cathode may be saturated and no more $[Tf_2N]^-$ ions can approach it. At this point, a multilayer EDL can be required to screen higher voltages. In this multilayer, no specific chemical interaction of electrode and counterion is possible; therefore the Cl$^-$ can contribute to the PS on the cathode, and thus the $\Delta\varphi_{cathodic}$ increases with a similar slope as for the neat $[C_8C_1Im]Cl$. In contrast to the Pt electrodes setup, the $[C_8C_1Im][Tf_2N]_xCl_{1-x}$ mixtures on the Au do not show the transition behavior in PS at 1.2 V as reported in Figure 36). On Au, the Cl$^-$ is a dominant counterion and the surface number density of Cl$^-$, required to saturate the first layer, is larger than that of $[Tf_2N]^-$ on Pt due to the smaller ion size of Cl$^-$. Therefore, the PS occurs within the first layer at the anode EDL solely by Cl$^-$ till 2 V and a contribution from multilayers to PS apparently does not play a role on Au.

4.4. Conclusions

In this Chapter, we have demonstrated the interfacial enrichment of specific anions in ILs mixtures through a fingerprint-type behavior of potential screening at polarized IL/electrode interfaces by using *in situ* XPS. We investigated mixtures of $[C_8C_1Im][Tf_2N]$ and $[C_8C_1Im]Cl$ and compared their behavior on gold and platinum electrodes. For the Au electrodes, the IL/electrode interface is dominated by the Cl^- anions even at the very low concentration of 0.1 mol% $[C_8C_1Im]Cl$. This selective enrichment occurs at zero applied voltage and is maintained up to 2 V. In contrast, for the Pt electrode, the IL/electrode interface is enriched with the $[Tf_2N]^-$ anions up to 90 mol% $[C_8C_1Im]Cl$, for applied voltage from zero to ~1.5 V. These examples demonstrate that the interfacial concentration of counterions at the IL mixture/electrode interfaces is determined by the interaction between IL and electrode, not by the bulk ratio of IL mixture.

Our results of the enrichment of minority species at the electrode interfaces imply that the small concentrations of an added IL or contaminations, e.g., a remains from the synthesis process, can dominate the entire situation at charged interfaces. This effect applies to various interfacial or electrochemical systems. For example, when tuning the properties of super-capacitors by adapting the stoichiometry of the ILs mixture, small concentrations of an added IL can be sufficient to modulate the entire interface, if the added one has a stronger interaction with the electrode. Also, the very small amount of impurities can be remarkably enriched at the electrode interface and change the structures and properties of EDL. We expect the consequences to be of similar importance as the known surface-enrichment effects at the gas/IL or vacuum IL interfaces.[116, 117] Therefore, the purity of IL should be of higher concern in electrochemical applications than in the bulk IL applications.

5.   Electrode / Ionic Liquid Interfaces in N_2 and Air Atmosphere

The content of this chapter is based and adapted from the following publication:[123]

The Effect of Ambient Conditions on the Potential Screening at Ionic Liquid – Electrode Interfaces

F. Greco, D. Hemmeter, S. Shin, H.-P. Steinrück and F. Maier

Journal of Ionic Liquids, 2022, **2**, 100019

5.1.   Introduction

As outlined above, ILs represent a significant innovation for electrochemical applications.[30, 31, 85, 96, 98, 114, 124, 125] Due to the great tunability of their physicochemical properties, these molten salts can be well adapted for electrodeposition,[85, 98, 124] supercapacitor[30, 31, 114] and battery[96, 125] technologies. Since ILs often have wider electrochemical windows compared to aqueous or organic electrolytes, they are particularly suitable to achieve higher energy densities in electrochemical devices. However, impurities can drastically affect their physicochemical properties and electrochemical performance. When working under ambient conditions, water is expected to be the main contamination, since ILs are typically hygroscopic; even hydrophobic ILs can rapidly absorb water if exposed to ambient humidity.[126] Already small mole fractions of water can cause a decrease in viscosity and weaken the electrostatic interactions between cations and anions.[127, 128] In electrochemistry, cyclic voltammetry (CV) studies of various ILs have shown a pronounced reduction of the electrochemical window with the increase of relative humidity.[129] Dissolved water in ILs can induce additional features in CVs, which can have comparable intensity to those of the electroactive species under study.[130] Moreover, decomposition reactions of IL ions, such as $[Tf_2N]^-$, can be catalyzed by the presence of water and OH^-.[131]

While the effect of residual water in ILs has been extensively studied for faradaic reactions, its influence at the liquid-solid interface and in particular on the structure of the electrical double layer (EDL) in non-faradaic situations such as in supercapacitors has been investi-

gated much less. Molecular dynamics simulations showed that impurity water molecules accumulate within a subnanometer thick layer at the charged electrodes, and that the accumulated amount increases with increasing voltage.[132] Hence, the electrical properties of the EDL can be strongly affected even by a small bulk concentration of water molecules, because small changes in local ion density can considerably change the potential drop across the IL/electrode interface.[132] Force curve studies at the Au(111)/[C$_4$C$_1$Pyrr][Tf$_2$N] interface performed with atomic force microscopy (AFM) showed a decreasing stiffness of the interfacial layering of the IL with increasing water concentration.[133] These findings were attributed either to adsorption of water molecules at the electrode, or to weakening the attraction between IL cations and anions, thereby modifying the layered structure close to the electrodes. Another AFM force curve study revealed alterations on the layering at the liquid/solid interface given by water also for an imidazolium-based IL ([C$_2$C$_1$Im][Tf$_2$N]) on Au electrodes; these changes were mainly attributed to the interaction of water with the ionic moieties of the IL while pronounced adsorption effects of water at the polarized Au electrodes were not observed.[134] From the mentioned studies, it is evident that different interactions between the components of the system involved (ions, contaminants, electrode surface, applied potential) contribute to the observed behavior. Thus, it is of great importance to compare the interaction of various ILs with different electrode materials under ultraclean conditions and ambient conditions. Moreover, since purifying and degassing of ILs might be costly and not always a feasible choice for large-scale applications, the characterization of the influence of contaminations on such systems is of great interest in order to find out the best operation condition when using ILs under ambient conditions without additional processing.

In this study, we focus on the effect of ambient conditions on the interface of ILs and different metal electrodes. We do this by investigating the potential screening (PS) behavior in air and also in a N$_2$ atmosphere (as model system with a low water content) in comparison to reference measurements under ultraclean (contamination-free) conditions. For the latter, we use XPS under ultra-high vacuum (UHV) conditions in a symmetric 2-electrode setup as detailed in Chapter 3. In these experiments, the binding energy shift (ΔBE) as a function of the applied voltage ($U_{applied}$) was found to be characteristic for a particular IL/electrode combination. Thus, the ΔBE vs $U_{applied}$ curves can be used as fingerprints, which, as detailed in Chapter 4, proved to be particularly valuable to deduce information on the PS and EDL composition at the polarized electrode interfaces of IL mixtures.[105] In this Chapter, we now extend this approach to compare PS curves recorded in UHV by XPS with PS curves in 1 bar N$_2$ gas or in

1 bar air using a 3-electrode setup (for details, see below). Notably, XPS cannot be performed at 1 bar, and thus only 3-electrode PS measurements can be realized under these conditions. From the comparison, conclusions on the influence of contaminations on the PS can be derived: On the one hand, if the PS curves recorded in N_2 or air show the same behavior as in UHV, we can assume that contaminants do not have any significant effect on the PS. On the other hand, different PS curves arising from different measuring environments indicate an alteration of the PS by contaminations. The comparison of measurements in N_2 and air provides some indication on the sensitivity of the PS and thus also the EDL to contaminations introduced by the surrounding gas atmosphere.

In the following, we first verify that PS measurements performed by XPS in UHV yield the same results as measurements using a very specific 3-electrode sample holder in UHV. Based on this proof-of-principle experiment, we then compare PS measurements by XPS in UHV with PS measurements with a 3-electrode setup performed in N_2 and in air, and simultaneously record the cell current between working and counter electrode (WE and CE). With these measurements, we demonstrate that there is indeed an influence of the gas atmosphere, which depends on applied voltage and the combination of IL and electrode material. By adding an excess of water in a 1:1 water-IL solution, we will demonstrate that the contamination effect on PS is mainly due to water. In the course of our studies, we also observed that for certain IL/electrode combinations reaction products formed under faradaic conditions lead to a contamination of the 3rd reference electrode, yielding time-dependent deviations from the true behavior

5.2.   Methods and Materials

Ultrapure $[C_8C_1Im][Tf_2N]$ and $[C_8C_1Im]Cl$ were synthesized as reported in a previous publication.[91] The Pt (Ø 0.30 mm) and Au(Ø 0.25 mm) electrodes with a purity of 99.99% and 99.995% and flame annealed before use, as in the previous chapters.

The PS measurements recorded with XPS in UHV are taken from Chapter 3. The PS measurements recorded in N_2 atmosphere and air were performed in an air-tight box (see Figure 38 and Appendix for more details) with an electrochemical cell developed by our group. The inlet and outlet pipes (1 and 2 in Figure 38) of the air-tight box allowed for a constant flow of high purity N_2 during the measurements performed in N_2 atmosphere. The

sample stage (3) is equipped with three spring contacts with which the electrodes are connected to the potentiostat and the multimeter through a feedthrough (4). To perform the measurements in air, the air-tight box was opened and exposed to atmospheric air before applying the voltage steps.
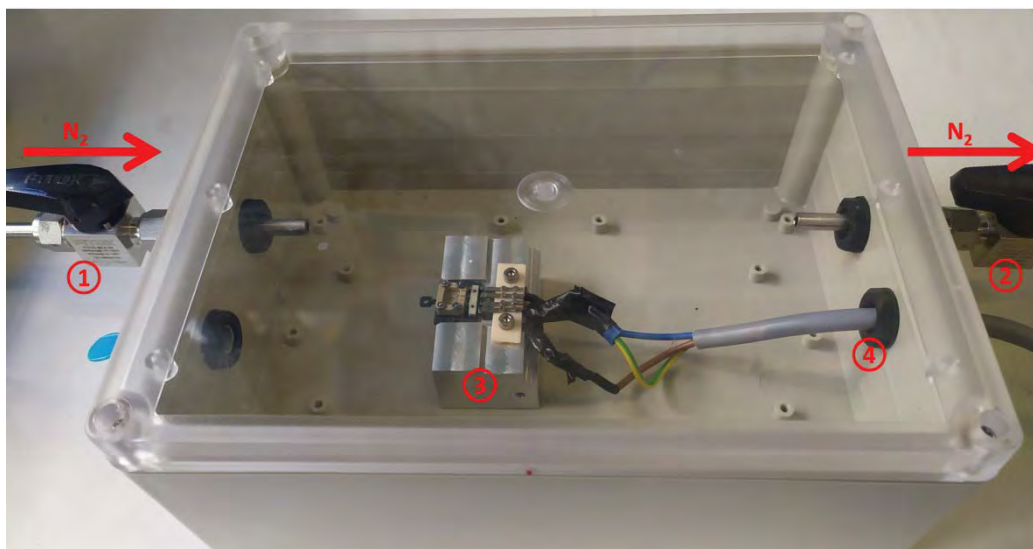
Figure 38 Air-tight box used to perform the measurements in N_2 atmosphere and air (numbers, see text).

The cell consists of a PEEK reservoir in which the IL is filled and WE and CE are immersed with great care to have the same contact area with the IL (± 5%). The distance between WE and CE was 5 mm and the Pt 3rd reference electrode was placed in between them at a distance of 2.5 mm from each. WE and CE were connected to a Keithley 2450 used as potentiostat. The voltage profiles were recorded with a Keithley DMM6500 used as high resistance multimeter.

5.3. Results and Discussion

5.3.1. Experimental Concept and Comparison of PS Measurements Using XPS in UHV and Using a 3rd Reference Electrode in UHV

In the following, the link between the 2-electrode XPS and 3-electrode PS measurements will be detailed in Figure 39 for non-faradaic conditions, both in UHV. As described in Chapter 3

for our 2-electrode setup, an external voltage $U_{applied}$ is applied between two identical electrodes (that is, same metal and same electrolyte/electrode contact area); the grounded electrode is the CE and the non-grounded one is the WE. Due to $U_{applied}$, the ions of the IL rearrange at the liquid/metal interfaces to compensate for the electrode charges forming EDLs, yielding corresponding potential drops $\Delta\varphi$ at the two electrodes (remember that due to the high ion density in ILs, the potential drops for moderate applied voltages predominantly occur within the first IL interface layer by accumulation of the corresponding counter ions,[64, 103] while no potential drop takes place in the bulk between the two electrodes, when faradaic currents are absent (see Chapter 3).
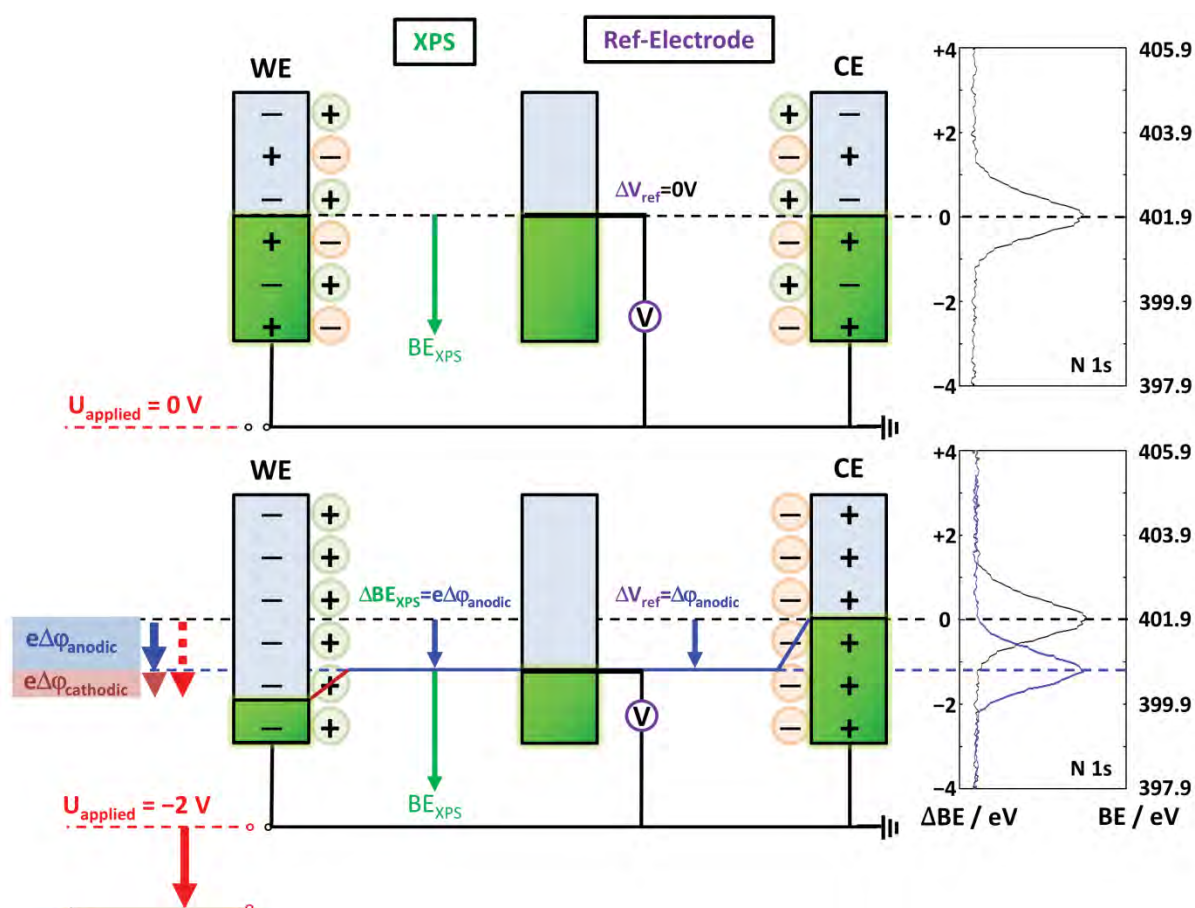
Figure 39 Schematic representation of the EDL structure and the potential at the interface for the electrochemical cell comprised of [C₈C₁Im]Cl and two identical Pt electrodes. The respective XPS spectra of the N 1s region are reported on the right, indicating the BE and the ΔBE for 0V and −2V applied. The eΔφ_anodic indicates the potential drop measured against the CE for −2V applied and is equal to ΔBE and ΔV_ref.

Consequently, the potential of the IL bulk shifts (Figure 39) relative to CE, which can be measured with XPS by recording one of the IL core levels: at a certain applied voltage, $U_{applied}$, the binding energy difference (ΔBE) relative to the BE at $U_{applied} = 0$ V gives access to the potential drop changes at the interfaces ($e\Delta\varphi$). In the example illustrated in Figure 39, ΔBE is equal to the potential drop at the anode ($e\Delta\varphi_{anodic}$), since the grounded CE is positively polarized and attracts the anions of the IL while $\Delta\varphi_{cathodic} = U_{applied} - \Delta\varphi_{anodic}$ is the potential drop at the WE (cathode).

Since XPS requires UHV conditions, the measurements in N_2 and air must be carried out in a different way, which we realize by recording the potential change (ΔV_{ref}) of a 3rd inert reference electrode that is connected to CE via a high resistance multimeter (>10 GΩ) (See Figure 40 and Appendix for further details).
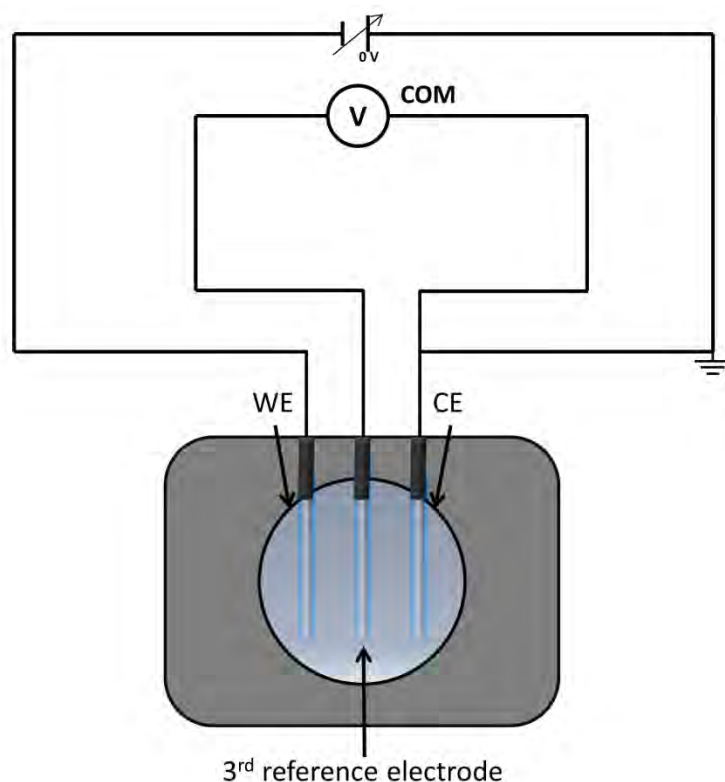
Figure 40 Sketch of the electrochemical cell used for the potential screening measurements in N_2 and air.

As shown in Figure 39, ΔV_{ref} recorded at $U_{applied} = -2$ V relative to $U_{applied} = 0$ V is equal to $\Delta\varphi_{anodic}$. To test the suitability of both methods, we performed proof-of-principle PS meas-

60

urements in UHV with both types of setup (2-electrode configuration with XPS (yielding ΔBE), 3-electrode setup (yielding ΔV_{ref}) by using the molybdenum support sample holder as 3rd reference electrode). For these experiments, we used an IL/electrode combination with a very characteristic ΔBE vs $U_{applied}$ behavior, namely [C$_8$C$_1$Im]Cl/Pt. As shown in Figure 41, ΔBE and ΔV_{ref} show exactly the same variation with $U_{applied}$, that is, ΔBE is equal to $e\Delta V_{ref}$.
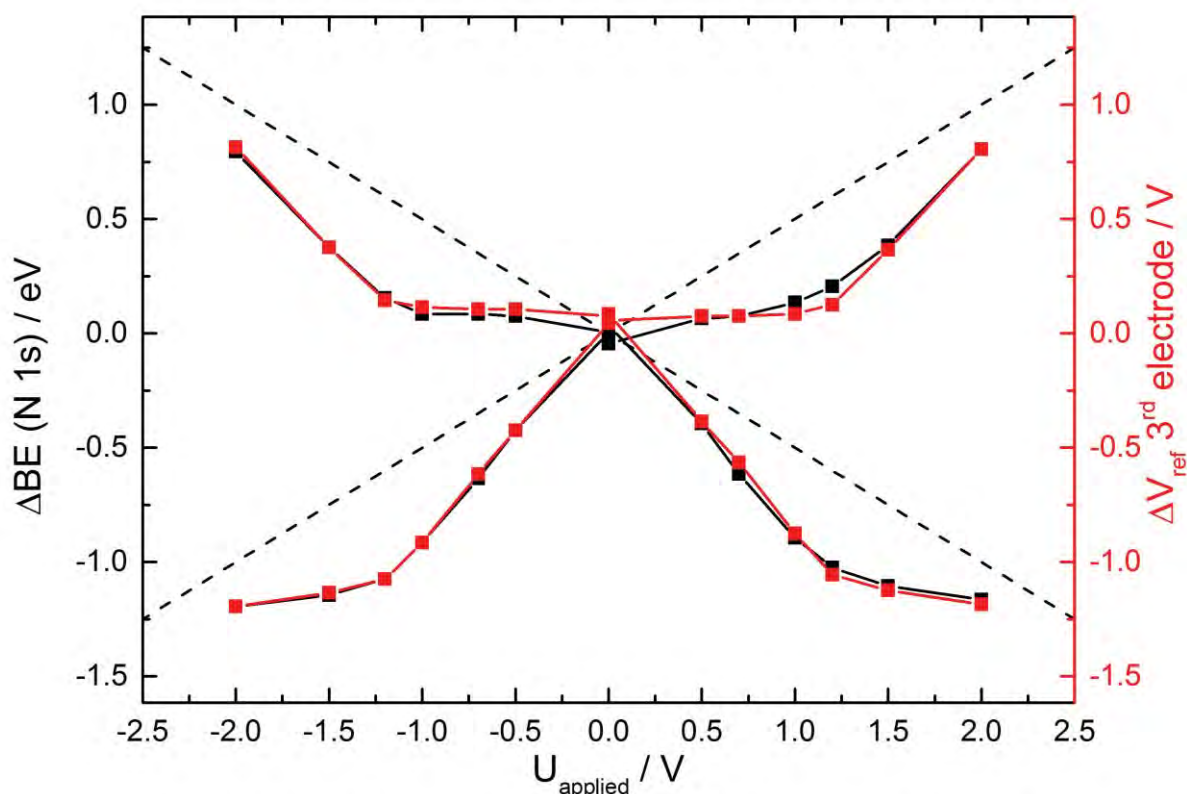
Figure 41 Relation between the ΔBE (N 1s) and the ΔV_{ref} measured with a 3rd reference electrode for the electrochemical cell comprised of [C$_8$C$_1$Im]Cl and two identical Pt electrodes vs an applied voltage. The black symbols correspond to the curves measured in UHV with XPS, the red symbols to the curves measured in UHV with a 3rd reference electrode. The dashed straight (±0.5 eV/V) lines indicate equal potential drop at the cathode and anode interface.

Since both methods agree well under UHV conditions, we can assert that our use of a 3rd reference electrode is suitable to measure PS also in N$_2$ atmosphere and air. All the ΔV_{ref} measurements are recorded for negative and positive polarization relative to both the WE and CE over time (See Appendix, Figures A30 to A33) and both $\Delta \varphi_{anodic}$ and $\Delta \varphi_{cathodic}$ are ob-

tained. This is particularly useful to detect modifications at the electrodes and in the electro-chemical cell during the measurements. As demonstrated in Chapter 3, $\Delta\varphi_{anodic} + \Delta\varphi_{cathodic}$ is always equal to $U_{applied}$ and $\Delta\varphi_{anodic}$ can be always converted to $\Delta\varphi_{cathodic}$ ($\Delta\varphi_{cathodic} = U_{applied} - \Delta\varphi_{anodic}$). In the next sections, the averages of the absolute values in the four quadrants (Figure 41) are shown as the $\Delta\varphi_{cathodic}$ curves for a clearer presentation; the error bars indicate the standard errors.

As a final remark, our 3-electrode PS method can of course be related to a typical 3-electrode setup consisting also of WE, CE and reference electrode (RE). In such a standard potentiostatic configuration, however, the WE is the electrode at which the potential relative to a high-ohmic RE is *controlled* via a potentiostat, that is, the applied voltage $U_{applied}$ between WE and CE is continuously adapted such to achieve a certain desired potential drop ΔV_{ref} *between WE and RE*. In our setup, a *constant* potential difference $U_{applied}$ of choice is applied *between WE and CE* employing a potential source (as it is done e.g. in a supercapacitor application), and ΔV_{ref} is only read through the high resistance circuit via a high resistance multimeter.

5.3.2.   [C$_8$C$_1$Im]Cl in N$_2$ and Air at the Au Electrode Interface

Figure 42a compares the $\Delta\varphi_{cathodic}$ curves of [C$_8$C$_1$Im]Cl for two identical Au electrodes measured in UHV (presented in Chapter 3), and in N$_2$ and air using a Pt wire as 3rd reference electrode. The data determined in UHV by XPS (black squares) are reproduced from Chapter 3. They exhibit a linear behavior with a slope of 0.92 V/V that is nearly twice the slope of 0.50 V/V (dashed line) of an ideal symmetric behavior, where half of the applied voltage is screened on the cathodic and the anodic sides. The observed highly asymmetric behavior of $\Delta\varphi_{cathodic}$ indicates that most of the PS takes place at the cathodic side while at the anodic side the PS is small. As discussed in Chapter 3 this behavior is due to the large size difference between the [C$_8$C$_1$Im]$^+$ cation and the Cl$^-$ anion. Remember that, in a simple Helmholtz approximation for ILs under non-faradaic conditions, $\Delta\varphi$ at an electrode is inverse proportional to the corresponding EDL capacitance and – due to the identical contact areas in our setup – directly proportional to the size of the counterions. Hence, at the cathode, the large imidazolium cations lead to a large $\Delta\varphi_{cathodic}$, which is considerably larger than the small $\Delta\varphi_{anodic}$ at the anode resulting from the smaller chloride anions (see Chapter 3).
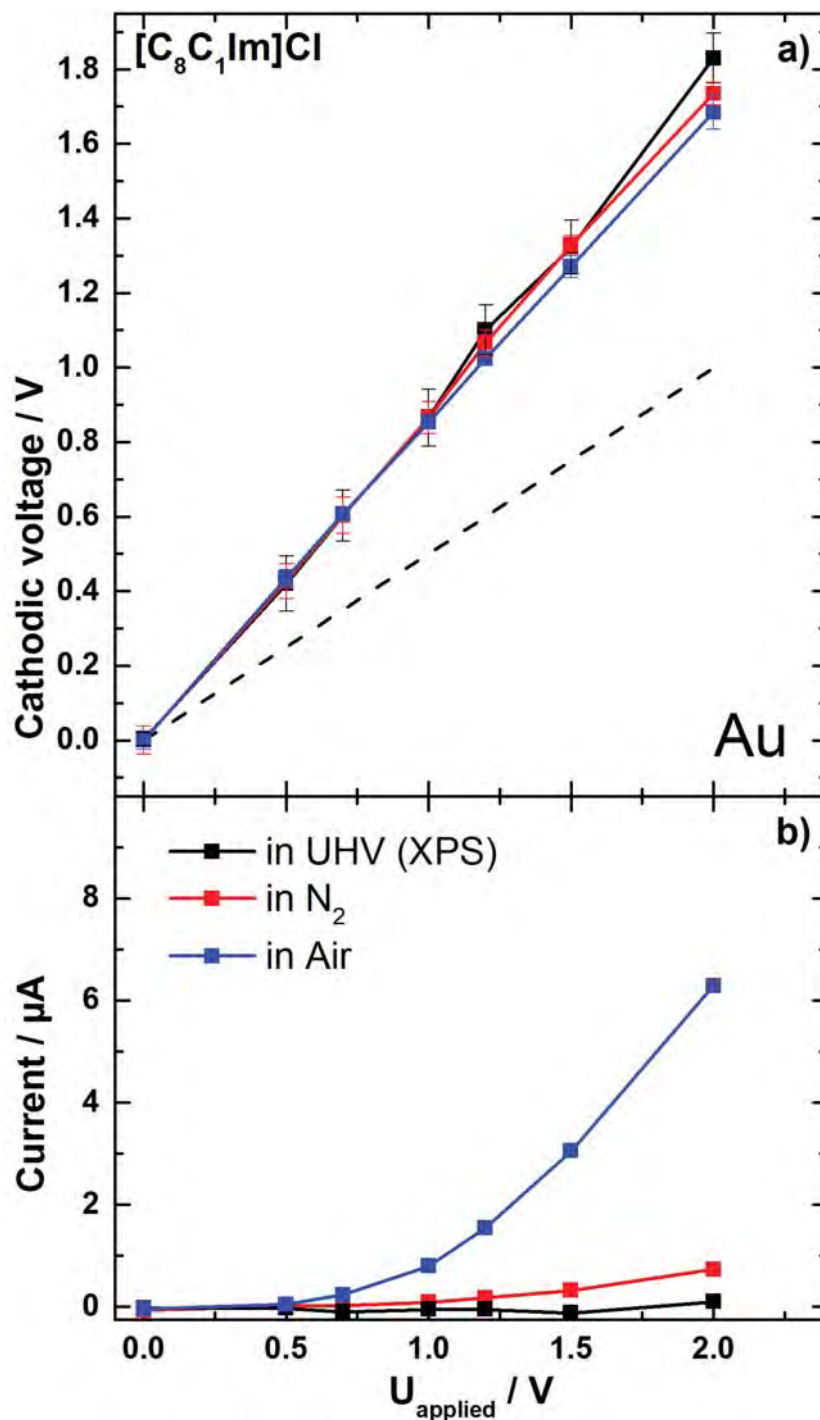
Figure 42 a) Cathodic voltage of [C$_8$C$_1$Im]Cl vs U$_{applied}$ between two identical Au electrodes. The black line refers to the measurements performed in UHV with XPS, red and blue lines refer to the measurements performed with a 3rd reference electrode in N$_2$ and Air atmosphere, respectively. The dashed straight line (± 0.5 V/V) indicates equal PS at the cathode and the anode. b) Averaged current recorded during the measurements.

To investigate the influence of ambient conditions on the PS characteristics, we performed PS measurements in N_2 and air (red and blue symbols in Figure 42) using a Pt wire as a 3rd reference electrode. Surprisingly, the cathodic voltage curves are virtually identical to the measurements performed in UHV. Following our fingerprint approach, the N_2 and air atmospheres lead to the same asymmetric PS behavior as in UHV (the small differences at 2 V are within the experimental uncertainty).

At first sight, this unchanged asymmetric behavior directly indicates an unchanged composition of the EDL which is solely given by the dissimilar sizes of cations and anions of the IL. However, considering the fact that the behavior is dominated by the large cations, yielding a slope of 0.92 V/V, small changes at the anodic side (e.g. via adsorption of other small ions such as OH^-) would also leave the behavior unchanged. Figure 42b depicts the measured steady-state currents between cathode and anode recorded during the PS measurements under the three different conditions. In UHV, the current is negligible up to the highest voltage of 2 V, indicating that faradaic phenomena at the electrode interface are absent under the ultra-clean conditions of UHV. On the contrary, in N_2 and air (red and blue symbols, respectively), the current rises above 0.5 V applied voltage, indicating that faradaic reactions start to take place at these voltages; notably, this current increase is much more pronounced in air than N_2, while it does not have an impact on the PS behavior. Therefore, for this particular IL/electrode combination, faradaic reactions do not seem to affect the observed PS, which is an indication that the composition of the corresponding EDLs does not change significantly due to the presence of N_2 or air. We propose that the residence time of formed redox products at the electrodes that are generated at voltages above 0.5 V is small compared to the time scale of our averaging PS measurements, which "see" predominantly Cl^- and $[C_8C_1Im]^+$ as counterions at the interfaces. At the anode, the dominant presence of Cl^- on Au at the expense of other species formed in course of the oxidation is not surprising: pronounced adsorption of halides at the Au surface in contact with IL mixtures was found even in cases where these halide anions were only present in traces (see Chapter 4).[118] As final comment, one should note that despite the fact that the PS curves and therefore the EDLs are not significantly affected by contaminations, the observed faradaic currents occurring in N_2 atmosphere and air could lead to issues such as discharging effects in IL-based supercapacitor applications.

5.3.3. [C$_8$C$_1$Im]Cl in N$_2$ and Air at the Pt Electrode Interface

The electrode material plays a crucial role in the structure of the EDL. In contrast to the previous example of [C$_8$C$_1$Im]Cl and Au electrodes, where $\Delta\varphi_{\text{cathodic}}$ is found to be always larger than $\Delta\varphi_{\text{anodic}}$ within the applied voltage range, the situation is very different for Pt electrodes. As it is evident from Figure 43a, $\Delta\varphi_{\text{cathodic}}$ under UHV conditions initially increases only very moderately in a linear trend (slope 0.12 V/V) up to 1.2 V applied voltage and then strongly increases with a slope of 0.81 V/V (black symbols); its absolute value stays always below the dashed line in the studied voltage range, that is, it is always smaller than $\Delta\varphi_{\text{anodic}}$.

In Chapter 3, this larger $\Delta\varphi_{\text{cathodic}}$ for different imidazolium ILs in UHV conditions was attributed to the specific attractive interaction of the π ring orbital of the aromatic cation with the d orbitals of the Pt electrode.

To study the impact of ambient environment, we also measured $\Delta\varphi_{\text{cathodic}}$ curves in N$_2$ and air; the data are also shown in Figure 43a (red and blue symbols, respectively). Up to 0.7 V, a similar PS behavior as in UHV is observed. In contrast, the transition to the steeper slope already occurs at 0.7 V in N$_2$ and air. This transition coincides with the onset of a significant current in Figure 43b, which is absent in UHV under the otherwise same conditions. Due to the similarity of the PS curves, we propose that the ambient conditions hardly affect the EDLs up to 0.7 V. The deviations observed at higher voltages are attributed to a change in the composition of the EDLs, such that the electrode/liquid interfaces are not exclusively composed of the counterions of the IL, but also by additional species formed in the redox reactions at the electrodes, which change the composition of the EDL. It is tempting to speculate about the nature of the formed redox species: since atomic hydrogen is known to be strongly bound on Pt,[135, 136] a possible candidate is hydrogen formed by reduction of residual water at the cathode, which weakens the specific attractive interaction of the imidazolium ring with the Pt electrode. As a consequence, the slope of the corresponding cathodic voltage curves changes more to the situation where the EDL capacitances are dominated by the different sizes of cation and anion without specific ion-electrode interactions in a similar way such as measured in the previous example of [C$_8$C$_1$Im]Cl in contact with Au electrodes even for values of U_{applied} close to zero.
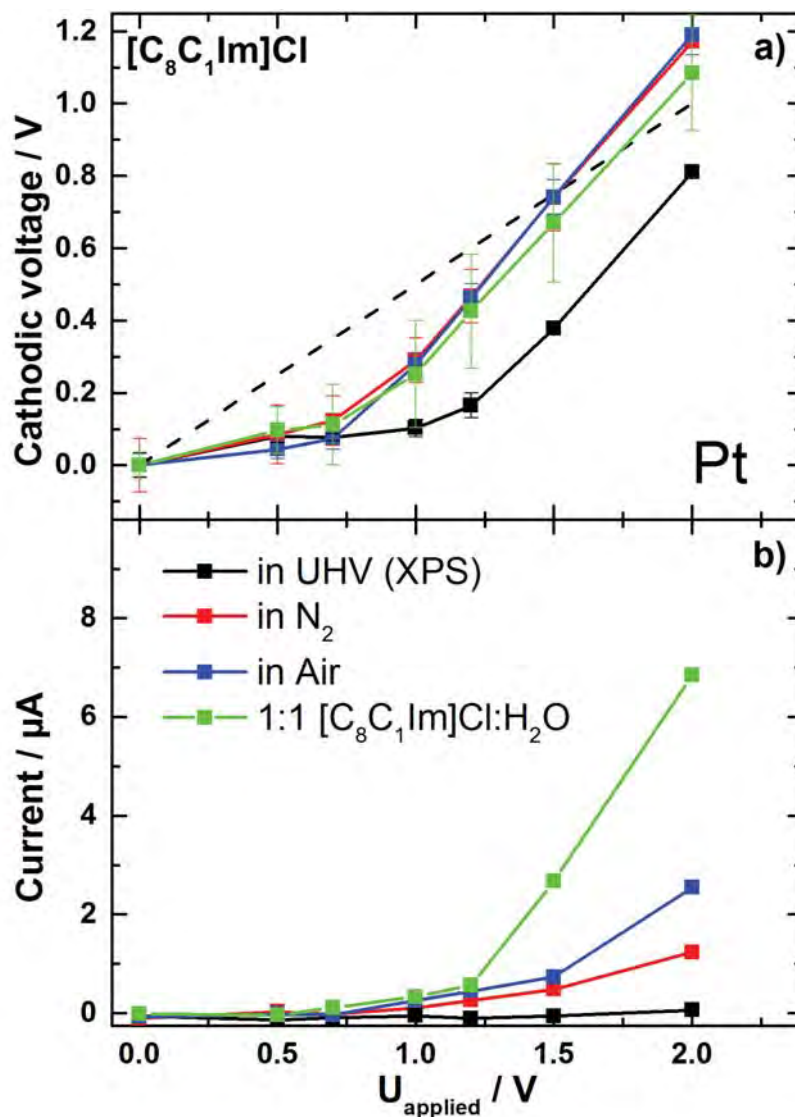
Figure 43 a) Cathodic voltage of [C₈C₁Im]Cl vs U_applied between two identical Pt electrodes. The black line refers to the measurements performed in UHV with XPS, red and blue lines refer to the measurements performed with a 3ʳᵈ reference electrode in N₂ and Air atmosphere, respectively. The green line represents PS data of a 1 : 1 molar solution of water and [C₈C₁Im]Cl recorded with a 3ʳᵈ reference electrode in N₂. The dashed straight line (± 0.5 V/V) indicates equal PS at the cathode and the anode. b) Averaged current recorded during the measurements.

In order to verify that the observed effects under ambient conditions are indeed due to water (as already suggested above) we performed an additional measurement with high water content. The green symbols in Figures 43a and b show $\Delta\varphi_{\text{cathodic}}$ and current values of a 1:1 molar mixture of [C₈C₁Im]Cl and H₂O, that is, one water molecule per ion pair measured with

66

Pt electrodes in 1 bar N_2. While the PS is identical to the measurements of the pure IL in N_2 and air, the observed currents have significantly increased as compared to air and even more as compared to N_2. This behavior strongly suggests that it is most likely water that leads to the observed deviations from ultraclean conditions. The fact that the changes in PS already occurred for N_2, that is, with only minor water content, indicates that already small amounts of water are sufficient to change the EDL.

The comparison of Au and Pt as electrode materials with the same IL shows how the interactions between ions, contaminants and electrodes strongly influence the observed PS, which is attributed to changes of EDL composition. These deviations observed above 0.7 V applied in N_2 and air, compared to UHV, can be relevant to electrochemical studies with a 3-electrode setup, such as CV and chronoamperometry. As mentioned above for a standard potentiostatic arrangement, the desired ΔV_{ref} is set between WE and RE and it is achieved by applying a voltage with a potential source between WE and CE. In this regard, different biases have to be applied between WE and CE in N_2 atmosphere and air than under ultraclean conditions.

5.3.4. $[C_8C_1Im][Tf_2N]$ in N_2 and Air at the Au Electrode Interface

While in the previous examples, cation and anion were very different in size, the sizes and thus also the expected EDL dimensions are very similar for $[C_8C_1Im][Tf_2N]$ as electrolyte. Figure 44a depicts $\Delta\varphi_{cathodic}$ as function of applied voltage between two identical Au electrodes. The XPS-derived data in UHV (black symbols) reveal a linear behavior with a slope of 0.45 V/V, that is, they lie approximately on the ideal line for symmetric PS with $\Delta\varphi_{cathodic} = \Delta\varphi_{anodic}$. In Chapter 3, we attributed this behavior to the absence of pronounced specific chemical interactions between the Au electrode and the anions and cations of the IL; the EDL capacitances are thus given by the similar size of the counterions at the corresponding interfaces. The experiments performed in N_2 and air (red and blue symbols, respectively) show the same PS behavior as in UHV, which indicates that ambient conditions do not significantly affect the structure of the EDL.

5.3.5. $[C_8C_1Im][Tf_2N]$ in N_2 and Air at the Pt Electrode Interface

The cathodic voltage curve of $[C_8C_1Im][Tf_2N]$ measured for two identical Pt electrodes in UHV is depicted in Figure 45a (black symbols). We observe the typical asymmetric behavior of imidazolium-based ILs on Pt electrodes described above and in Chapter 3, with $\Delta\varphi_{cathodic}$ being smaller than $\Delta\varphi_{anodic}$; the initial slope of the curve is 0.27 V/V. The PS curves recorded in N_2 and air (red and blue symbols, respectively), however, show a steeper increase with a slope of 0.44 V/V and 0.42 V/V respectively, which is closer to the ideal line. Similar to our observation on Au for this IL, the observed currents between WE and CE are very low for this electrolyte in UHV and also under non-UHV conditions up to 1.5 V applied, which rules out pronounced redox reactions being responsible for the observed changes. Hence, we attribute the different PS curves for Pt to the fact that residual contaminants being present in the IL (most likely traces of water) adsorb on Pt and weaken the interaction of the IL with the electrode; this in turn leads to different liquid/metal EDLs than in UHV.

Interestingly, the comparison of the observed behavior for Pt and Au electrodes shows a pronounced influence of the ambient conditions on the PS behavior for both $[C_8C_1Im][Tf_2N]$ and $[C_8C_1Im]Cl$ in the case of Pt electrodes, while for Au electrodes hardly any influence is seen. This difference can possibly be attributed to the hydrophobicity and ionophilicity of the Au electrode,[134] at which the interaction with the IL counterions is favorable over other species. In contrast, the interactions between Pt electrodes and the imidazolium cations dominate for pure ILs, but under ambient conditions, the affinity of certain contaminants or redox products might be even stronger and drastically alter the interfacial composition.
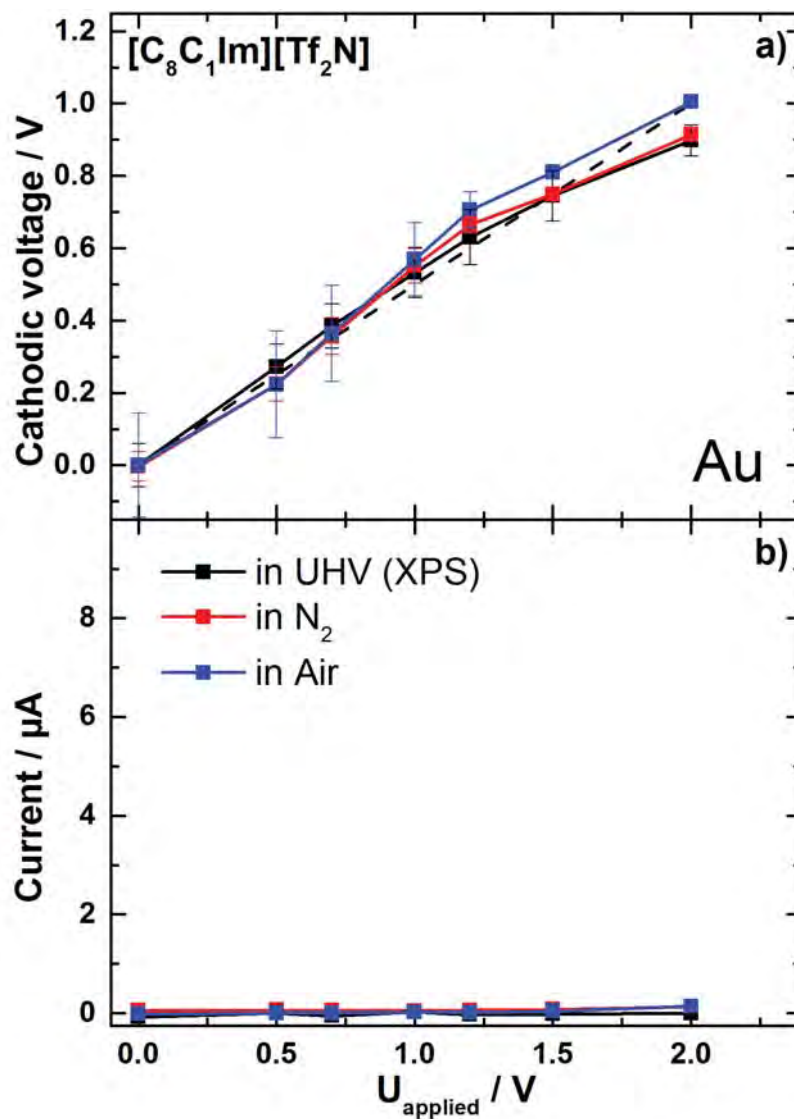
Figure 44 a) Cathodic voltage of [C₈C₁Im][Tf₂N] vs U_applied between two identical Au electrodes. The black line refers to the measurements performed in UHV with XPS, red and blue lines refer to the measurements performed with a 3ʳᵈ reference electrode in N₂ and Air atmosphere, respectively. The dashed straight line (± 0.5 V/V) indicates equal PS at the cathode and the anode. b) Averaged current recorded during the measurements.
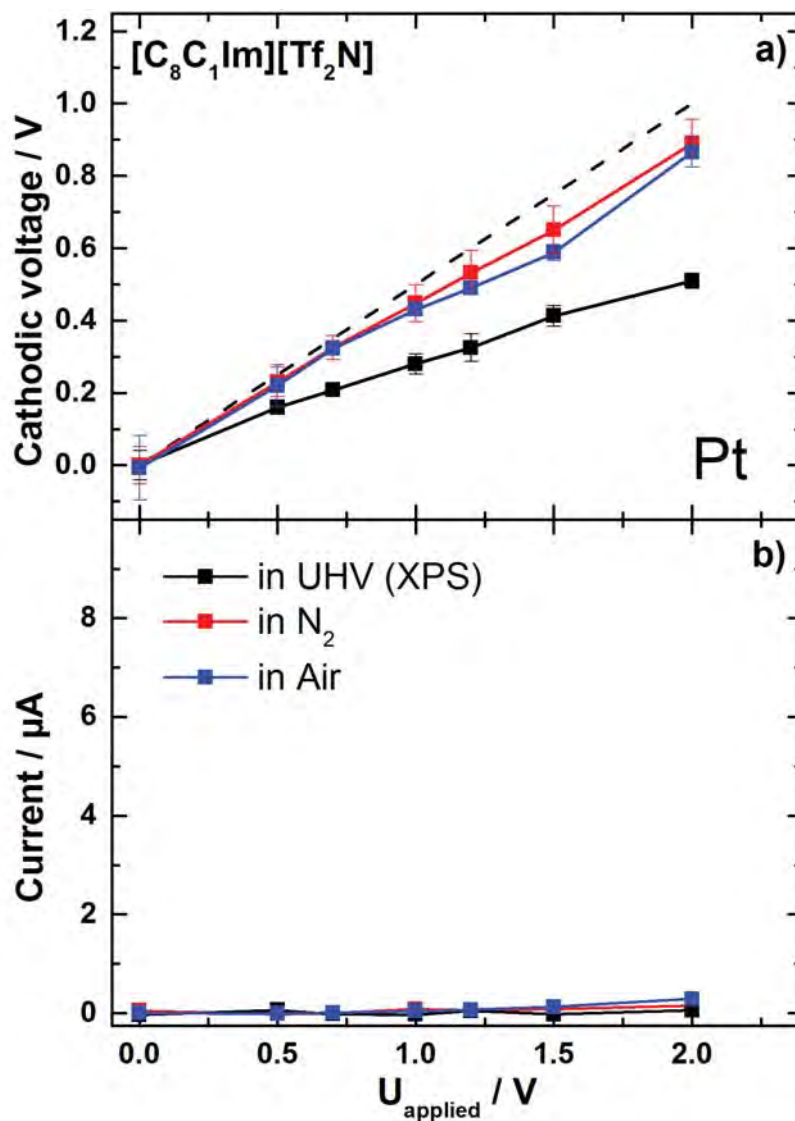
Figure 45 a) Cathodic voltage of [C₈C₁Im][Tf₂N] vs U_applied between two identical Pt electrodes. The black line refers to the measurements performed in UHV with XPS, red and blue lines refer to the measurements performed with a 3rd reference electrode in N₂ and Air atmosphere, respectively. The dashed straight line (± 0.5 V/V) indicates equal PS at the cathode and the anode. b) Averaged current recorded during the PS measurements.

5.3.6. Contamination of the 3rd Reference Electrode

In this section, we want to address an interesting observation in some of the studies reported in this Chapter. Typically, we perform four PS measurements with positive and negative $U_{applied}$ voltage steps and either the WE or CE grounded. The four quadrants as shown in Figure 41 are then averaged yielding the data shown in Figures 42 to 45. The detailed measurements as a function of time are shown in Figures A30 to A33 in Appendix. After a voltage ramp from 0 to ± 2 V, the applied voltage was set back to 0 V to start the next experiment. In all UHV experiments (black data), the ΔBE values and also in all experiments in N_2 the ΔV_{ref} values (red data) dropped back to zero, as is to be expected. This is also the case for the experiments in air (blue data), with the exception of the experiments for $[C_8C_1Im][Tf_2N]$ with Pt and Au electrodes, where we observe a strong change on the ΔV_{ref} at $U_{applied} = 0$ V (Figures A32 and A33, blue data). This deviation was observed after the first voltage ramp in air and it was persistent for all the following measurements. These deviations were not observed in UHV and N_2 and with all the other electrode/IL combinations in all the different measuring conditions.

To further investigate this phenomenon, we measured ΔV_{ref} for $[C_8C_1Im][Tf_2N]$ with two identical Au electrodes at $U_{applied} = 0$ V for 10 minutes before and after positive and negative voltage steps (Figure 46). For all $U_{applied}$ values up to ±1.5 V, the ΔV_{ref} value measured at $U_{applied} = 0$ V after the voltage steps approached zero after a certain relaxation time, indicative of the reorganization of the EDL after the potential change: For instance, for $U_{applied} = -1.5$ V, we observe a positive ΔV_{ref} during the step and after changing back to $U_{applied} = 0$ V, a small remaining positive ΔV_{ref} value slowly decays to zero. Accordingly, for $U_{applied} = +1.5$ V, ΔV_{ref} is negative, and after changing back to $U_{applied} = 0$ V, a small remaining negative ΔV_{ref} value slowly decays to zero. Surprisingly, the behavior is different when applying ±2.0 V, where the ΔV_{ref} values recorded at $U_{applied} = 0$ V after the steps are always negative, independent of the sign of the voltage steps.

We attribute the expected behavior up to ±1.5 V to the slow transport kinetics of the IL ions in the highly viscous media, leading to a slow reorganization of the counterions at the EDL after the potential step and an excess of cations at the cathode and anions at the anode remaining when no voltage is applied ($U_{applied} = 0$ V). It has been reported in differential capacitance (C_d) measurements that slow transport kinetic can lead to hysteresis of the C_d

curves, which requires to wait until the system is back to equilibrium before starting a new measurement.[41]
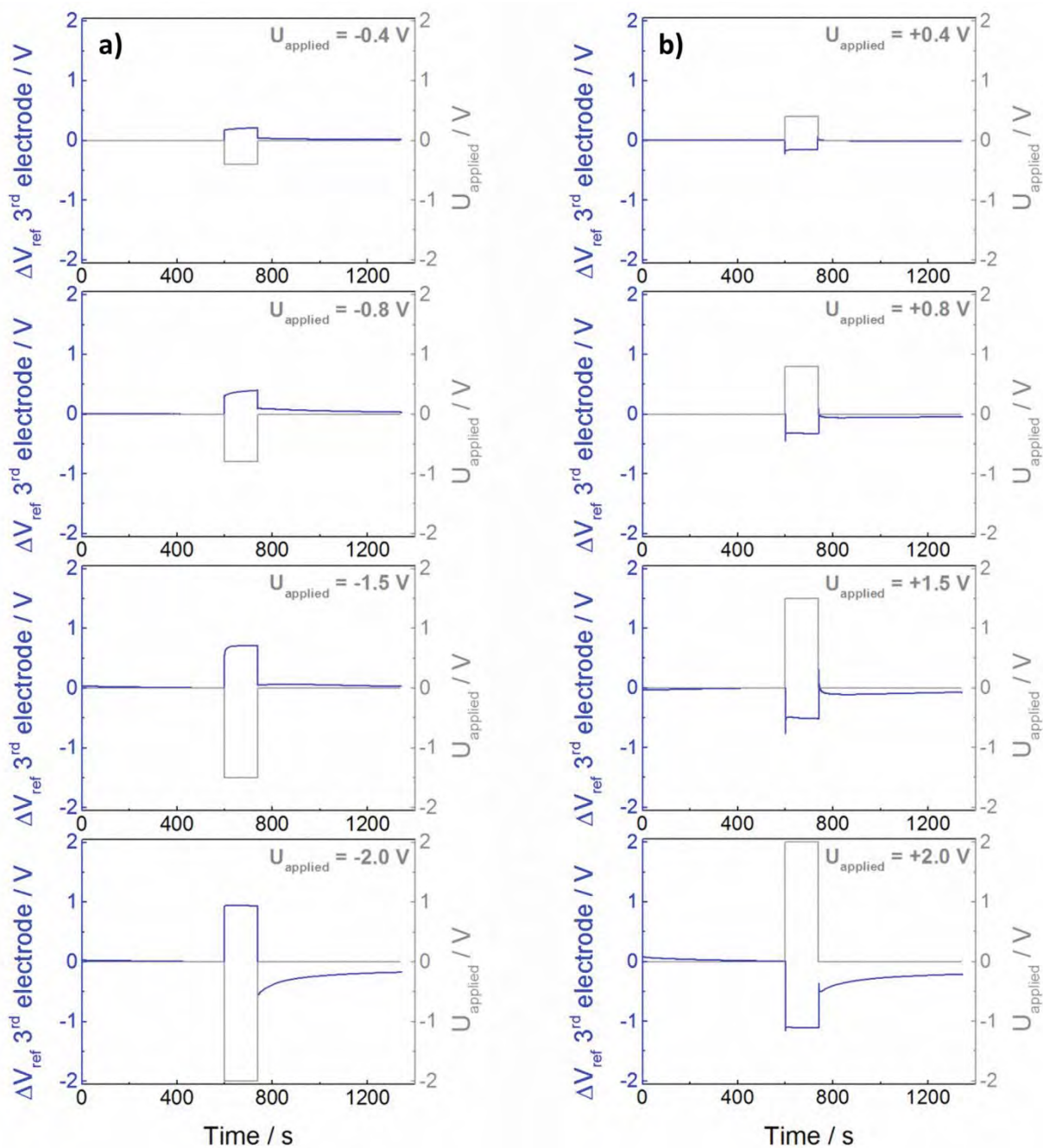
Figure 46 ΔV_{ref} recorded with a Pt 3rd reference electrode in air for positive (a) and negative (b) voltages applied. The voltage is held at $U_{applied} = 0$ V for 600 s before and after the voltage steps. The voltage steps have a duration of 139 s.

In contrast, the always negative ΔV_{ref} values observed at $U_{applied} = 0$ V after ± 2.0 V steps in Figure 46 have a different origin. We attribute them to redox products in the IL phase that adsorb on the 3rd reference electrode and thereby change the reference potential. As our setup is symmetric with respect to WE and CE, positive or negative applied voltages lead to the same redox products and thus the same effect on the 3rd reference electrode. A possible origin of this effect could be electrodegradation of the $[Tf_2N]^-$ anion in presence of OH^- and water, that is, when not operating in dry conditions.[131] This reaction produces anionic and radicalic fragments of the $[Tf_2N]^-$, such as $\cdot NSO_2CF_3^-$ and $SO_2CF_3^-$, which can be highly surface-active at the 3rd reference electrode.

As mentioned above, the 3rd reference electrode used in our study is related to the RE electrode of a standard 3-electrode setup. In this regard, our study shows the possibility to use the ΔBE recorded through XPS as a stable and reliable reading of the potential difference between the electrolyte and the electrodes. This is particularly interesting for all the *in-situ* studies in which all the three electrodes (WE, CE and RE) are located in the same cell compartment and therefore the influence of redox species on the stability of the RE cannot be avoided.

Finally, the observed sensitivity of the potential measured by the 3rd reference electrode towards contaminations could also be a hint towards explaining uncertainties/differences of several tenths of eV that are frequently observed in reported XPS binding energy values of nominally identical ILs.[101, 137] These can possibly be traced back to changes of the potential drop at the interface of the IL with the grounded support due to residual contaminations adsorbing at this interface, and thus, changing the related EDL. Moreover, this interpretation could explain long-term changes of XPS binding energy values quite commonly observed during the course of XPS measurements, due to adsorption of species created by X-ray-induced beam damage of the ILs.

5.4. Conclusions

We investigated the effect of ambient conditions on the PS at the interface of $[C_8C_1Im][Tf_2N]$ and $[C_8C_1Im]Cl$ with polarized Au and Pt electrodes. For this purpose, data collected in 1 bar air and also in 1 bar N_2 using a 3 electrode setup are compared to reference measurements under ultraclean (contamination-free) conditions by XPS in a symmetric 2-electrode setup. The observed binding energy shifts as a function of the applied voltage $U_{applied}$ mirror the PS

and EDL composition at the polarized electrode/IL interfaces. From the comparison, conclusions on the influence of contaminations on the PS can be derived: On the one hand, if the PS curves recorded in N_2 (that is, moderate clean conditions) or air (full ambient conditions) show the same behavior as in UHV, we can assume that contaminants from ambience do not have a significant effect on the PS. On the other hand, different PS curves arising from different measuring environments indicate an alteration of the PS by contaminations. In the course of our study, we first confirmed that PS measurements performed by XPS in UHV yield the same results as measurements using a very specific 3-electrode sample holder in UHV. This proof-of-principle experiment is the basis for comparing PS measurements by XPS in UHV with PS measurements with a 3-electrode setup performed in N_2 and in air. Additional information is obtained from simultaneously recording the cell current between working and counter electrodes.

With our PS and current measurements, we demonstrate that there is indeed an influence of the gas atmosphere, which depends on applied voltage and the combination of IL and electrode material. For Pt electrodes, we find a pronounced influence of the ambient conditions on the PS for both $[C_8C_1Im][Tf_2N]$ and $[C_8C_1Im]Cl$, while for Au electrodes hardly any influence is seen even under faradaic conditions. The latter indicates that due to overall attractive interactions between Au and IL ions, the EDLs are dominated by the IL counterions whereas other possible co-adsorbed species that are e.g. produced in a faradaic process have a short life-time at the metal-IL interface. In contrast, the very specific interactions between Pt electrodes and the imidazolium cations that dominate for pure ILs, are significantly altered under ambient conditions due to the affinity of certain contaminants or redox products adsorbing on Pt. These findings indicate that the interplay between contaminations, IL ions and the electrode material determine the composition of the EDL in which the strongest interactions lead to the final interfacial behavior. By adding an excess of water in a 1:1 water-IL solution, we demonstrated that the contamination effect on PS observed under ambient conditions is most likely due to water. In the course of our studies, we also observed that for certain IL/electrode combinations reaction products formed under faradaic conditions lead to a contamination of the 3rd reference electrode, yielding time-dependent deviations from the true behavior.

To conclude, our findings demonstrate that in electrochemical studies and applications of ILs in ambient conditions several factors can compromise the results and the performances of such devices. In this regard, the comparison between the PS behaviors obtained with *in-situ* XPS under ultraclean conditions and with the 3rd reference electrode in ambient conditions

can be employed as a reliable tool to detect and subsequently avoid undesirable effects arising from species other than solely the ions of the ILs.

6. Two Different Materials Electrode / Ionic Liquid Interfaces

6.1. Introduction

As already mentioned in the introductory Chapter 1, one of the biggest challenges in supercapacitors is to increase the energy densities. The energy density (E) in a supercapacitor is given by the following equation:

$$E = \frac{CU^2}{2}$$

where C and U are the capacitance and the total operative voltage window of the device, respectively. In this context, higher values of E can be achieved by increasing C, e.g. through high-surface-area carbonaceous materials,[3, 4] or by using electrolytes which can withstand high U without incurring in electrodegradation, such as organic electrolytes or ILs.

In a supercapacitor, the total operative voltage window depends on the electrochemical stability of the electrolyte at both cathode and anode. In a device comprised of two identical electrodes (symmetric), the electrochemical stability can be limited by irreversible electrochemical processes occurring at only one of the two electrodes. Replacing such a "limiting" electrode by an electrode, which provides higher electrochemical stability is therefore a suitable way to expand the maximum operational window of a supercapacitor. Electrochemical cells consisting of two different electrodes are referred in literature as asymmetric devices.[138] The two electrodes can be different in charge storage mechanism (faradaic, non-faradaic, pseudocapacitive), thickness, weight, surface area, and material. Asymmetric devices have been mainly investigated in aqueous and organic electrolytes and showed (i) high capacitance, high operative voltage range and high energy densities by combining one activated carbon electrode and one graphite electrode;[139] (ii) high operative voltage window and good cycling performance by combining RuO_2/TiO_2 nanotube composite and activated carbon

electrodes;[140] (iii) enhanced energy densities by changing the mass loading of the active material between negative and positive electrode.[141]

In Chapter 3, it was demonstrated that potential screening (PS) measurements through *in-situ* XPS under the ultra-clean condition of ultra-high vacuum (UHV) are a reliable tool to study the electrical double layer (EDL) at the IL/electrode interface in a symmetric two-electrode electrochemical cell. In such symmetric cell, we observed a very characteristic behavior of the potential drop at the cathode ($\Delta\varphi_{cathodic}$) and the anode ($\Delta\varphi_{anodic}$) as a function of the applied potential. According to the specific combination of the IL and the electrode material, the potential drop ranged from symmetric to asymmetric, that is, $\Delta\varphi_{cathodic} = \Delta\varphi_{anodic}$ and $\Delta\varphi_{cathodic} \neq \Delta\varphi_{anodic}$. In this regard, strong asymmetric behaviors ($\Delta\varphi_{cathodic} >> \Delta\varphi_{anodic}$ or $\Delta\varphi_{cathodic} << \Delta\varphi_{anodic}$) could lead to the occurrence of irreversible faradaic reactions at one of the two electrodes earlier than at the other. Therefore, in this Chapter, we explore with *in-situ* XPS in UHV a possible route to tune and equalize the potential drop at both electrode interfaces, by combining an Au and a Pt electrode in a two-electrode asymmetric cell. In the following explorative approach, we will compare the $\Delta\varphi_{cathodic}$ curves obtained with a symmetric cell (data from Chapter 3) and an asymmetric cell.

6.2.   Methods and Materials

Ultrapure $[C_8C_1Im][Tf_2N]$ and $[C_8C_1Im]Cl$ were synthesized as reported in a previous publication,[91] $[C_4C_1Pyrr][Tf_2N]$ was purchased from IoLitech with a purity >99%. The Pt and Au electrodes used for the measurements shown in this chapter have both a diameter of 0.30 mm, a purity of 99.99% and 99.9% and were flame-annealed before use.

The PS measurements of the cell with two electrodes composed of the same material (Au or Pt) are taken from Chapter 3. The PS measurements of the cell comprising two different material electrodes were performed in an identical way as those as described in Chapter 3. For each combination of IL and metal, the Pt and the Au electrodes were mounted in the electrochemical cell in such a way that their contact areas with the ILs were identical (±5%); this is important in order to avoid geometry effects on the PS. XPS was carried out using a monochromated Al Kα source and a hemispherical ARGUS analyzer (see Chapter 2.2). High-resolution scans were recorded with a pass energy of 35 eV and a dwell time of 0.5 s with an overall energy resolution of 0.4 eV (see Chapter 2.2).

6.3.   Results and Discussion

As already described in Chapter 3, when an external voltage ($U_{applied}$) is applied in a two-electrode electrochemical cell, the ions of the IL form an EDL at the liquid/metal interfaces to compensate for the electrode charges, and a potential drop ($\Delta\varphi$) occurs within the first IL interface layer at the two electrodes. The resulting shift of the potential of the IL in the bulk (Figure 47) relative to the grounded electrode can be measured with XPS by following the binding energy (*BE*) of one of the IL core levels at a certain value of $U_{applied}$ (Figure 48 top).
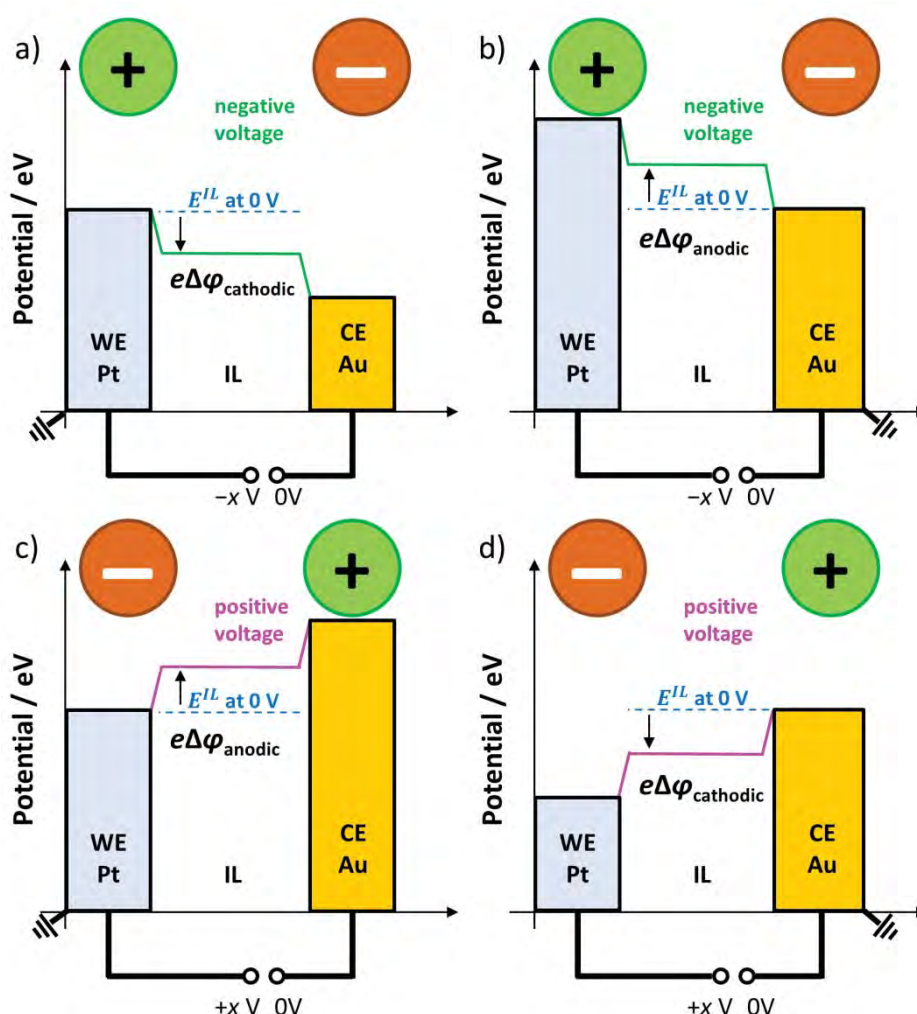
Figure 47 Schematic representation of the IL/electrodes interfaces for negative (a and b) and positive (c and d) polarization with the Pt WE grounded (a and c) and the Au CE grounded (b and d); cations and anions at the electrodes are represented as green and orange circles respectively.

The binding energy difference relative to the *BE* at $U_{applied} = 0$ V allows us to obtain the potential drop changes at the interfaces ($e\Delta\varphi$). Again, we denote the amount of PS relative to $U_{applied} = 0$ V at the anode (plus pole) as $\Delta\varphi_{anodic}$ and that at the cathode (minus pole) as $\Delta\varphi_{cathodic}$.
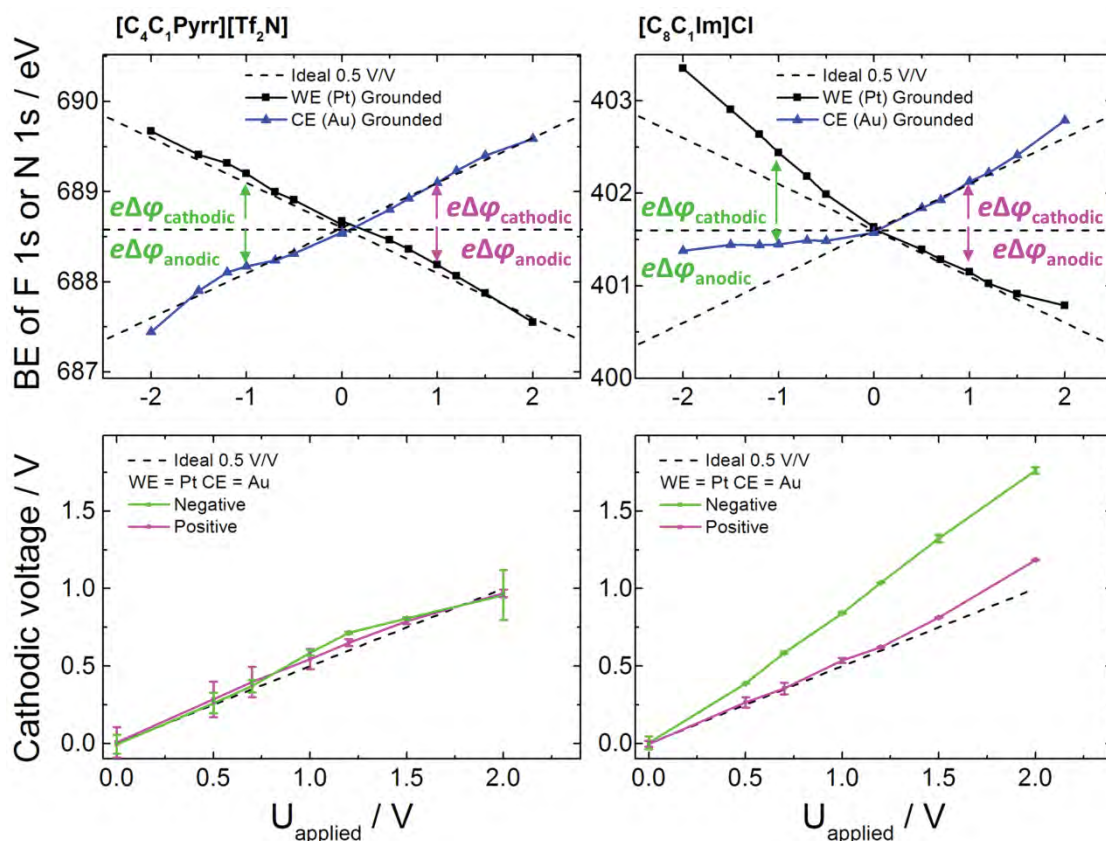
Figure 48 (Top) BE of the F 1s and N 1s peak for [C₄C₁Pyrr][Tf₂N] and [C₈C₁Im]Cl, with Pt WE grounded (black) and Au CE grounded (blue). (Bottom) Corresponding cathodic voltages at the different electrodes of [C₄C₁Pyrr][Tf₂N] and [C₈C₁Im]Cl for negative (Δφcathodic at Pt electrode, green) and positive (Δφcathodic at Au electrode, magenta) polarization of the Pt WE.

In comparison to the measurements reported in Chapters 3 to 5, here we are using two electrodes composed of different materials; therefore, some more remarks have to be added. In the set-up used in the following experiments, the Au electrode is always connected to the counter electrode (CE) plug of the potentiostat, which means that for negative polarization (Figures 47a and b) the Au electrode will be always positively polarized and therefore act as

anode; *vice versa*, the Pt working electrode (WE) will act as cathode. As shown in Figures 47c and d for positive $U_{applied}$, the Au and Pt electrodes will always be cathode and anode, respectively. Thus, in this specific example, the $\Delta\varphi_{cathodic}$ and $\Delta\varphi_{anodic}$ obtained for negative polarization stem from cations and anions at the Pt and Au electrodes, respectively.

In contrast, $\Delta\varphi_{anodic}$ and $\Delta\varphi_{cathodic}$ for positive polarization come from cations at the Au electrode and anions at the Pt electrode, respectively. This leads again to very characteristic *BE* shifts depending on polarization and grounding as demonstrated for the two ILs [C$_4$C$_1$Pyrr][Tf$_2$N] and [C$_8$C$_1$Im]Cl (see Figure 48, Top). In the following, the results will be shown only as function of $\Delta\varphi_{cathodic}$ (see Figure 48, Bottom) for both negative and positive polarization of the WE, in order to give a clearer presentation; remember that $\Delta\varphi_{anodic}$ can always be directly converted to $\Delta\varphi_{cathodic}$ and *vice versa* because $U_{applied} = \Delta\varphi_{cathodic} + \Delta\varphi_{anodic}$.
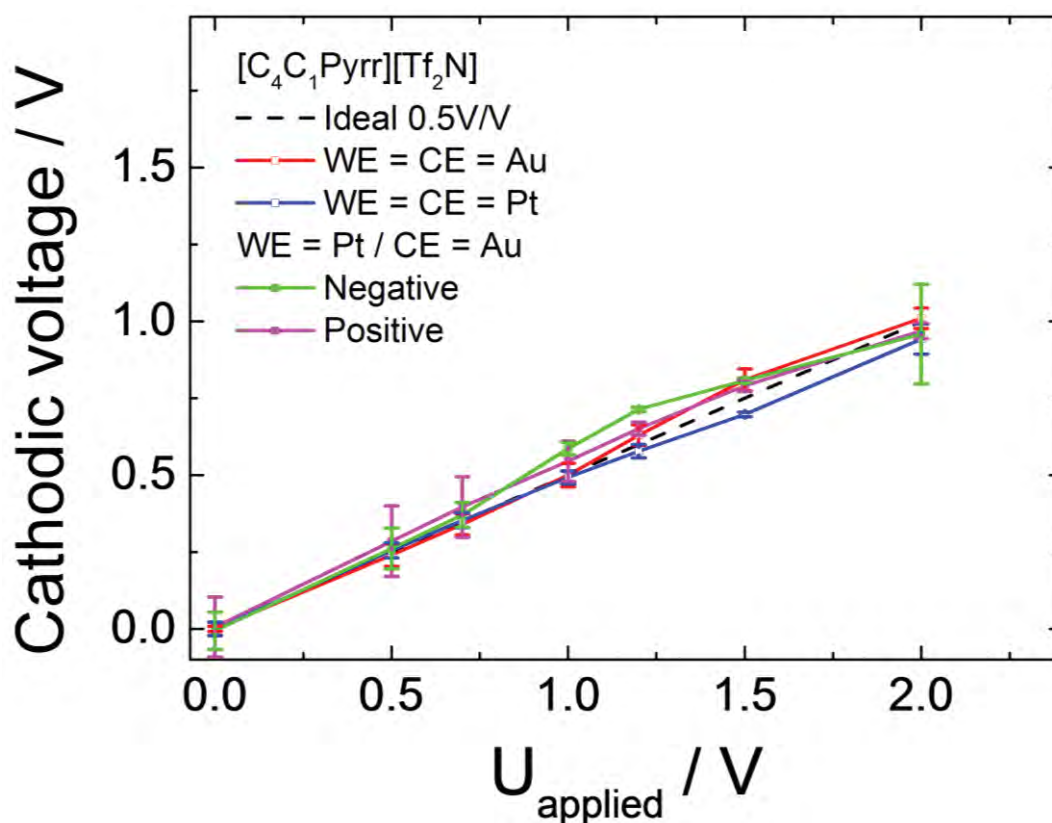
Figure 49 Cathodic voltage of [C$_4$C$_1$Pyrr][Tf$_2$N] versus *applied voltage, for two identical Au WE and CE (red); for two identical Pt WE and CE (blue); for Pt WE and Au CE at negative (green) and positive (magenta) polarizations. Equal potential drops at the anode and cathode interfaces are indicated as dashed straight line with a slope of +0.5 V/V. The error bars show standard deviations of the measurements.*

In Figure 49, the $\Delta\varphi_{cathodic}$ curves presented in Chapter 3 for [C$_4$C$_1$Pyrr][Tf$_2$N] in a symmetric two-electrode cell (red line for two identical Au electrodes; blue lines for two identical Pt electrodes) are compared with the behavior obtained from an asymmetric cell for negative (green line) and positive (magenta line) polarizations. In Chapter 3, the slope of 0.5 V/V observed for [C$_4$C$_1$Pyrr][Tf$_2$N] with both two identical Au or Pt electrodes was attributed to the absence of strong interactions of the IL counterions with the electrode material. Therefore, the equal values for $\Delta\varphi_{cathodic}$ and $\Delta\varphi_{anodic}$ were attributed to the comparable sizes of anion and cation, following a simple Helmholtz approximation. The $\Delta\varphi_{cathodic}$ curves observed for the asymmetric cell at negative and positive polarizations show the same behavior as for the symmetric cell. This behavior confirms that the electrode material does not play a role for this system and that the PS is solely dominated by the sizes of the counterions. Furthermore, the almost identical behavior of the cathodic voltage at negative and positive polarizations indicates that the roughness of the two different materials used as electrodes is comparable. Notably, a different roughness would lead to different contact areas between the electrolyte and the two electrodes and consequently to different PS curves for negative and positive polarizations (see Figure A3 in the Appendix for more details on the effect of different contact areas between electrode and electrolyte on the PS curves). The latter observations can be considered as a proof-of-principle experiment demonstrating that PS experiments in an asymmetric cell with two different material electrodes can be applied to more complex systems, where specific interactions between the counterions and the electrodes can occur and the size of cations and anions of the IL is different.

The next investigated IL is [C$_8$C$_1$Im][Tf$_2$N]. The corresponding cathodic voltage curves measured in both a symmetric and an asymmetric two-electrode electrochemical cell are depicted in Figure 50. As already reported in Chapter 3, the PS curve recorded with two identical Pt electrodes shows a smaller $\Delta\varphi_{cathodic}$ than $\Delta\varphi_{anodic}$ with a slope of 0.27 V/V (see Figure 50, blue line). This characteristic behavior was attributed to the smaller distance $d_{cathodic}$ of the flat-lying imidazolium rings at the cathode compared to the larger [Tf$_2$N]$^-$ at the anode due to strong specific interactions between the π orbitals of the [C$_8$C$_1$Im]$^+$ with the d orbitals of the Pt electrodes (see Chapter 3). With two identical Au electrodes (see Figure 50, red line), the PS curve shows a $\Delta\varphi_{cathodic}$ almost equal to $\Delta\varphi_{anodic}$ with a slope 0.45 V/V. In Chapter 3, this behavior was attributed to the absence of strong interactions between the Au electrode and the IL and to the comparable size of cation and anions at the interface.
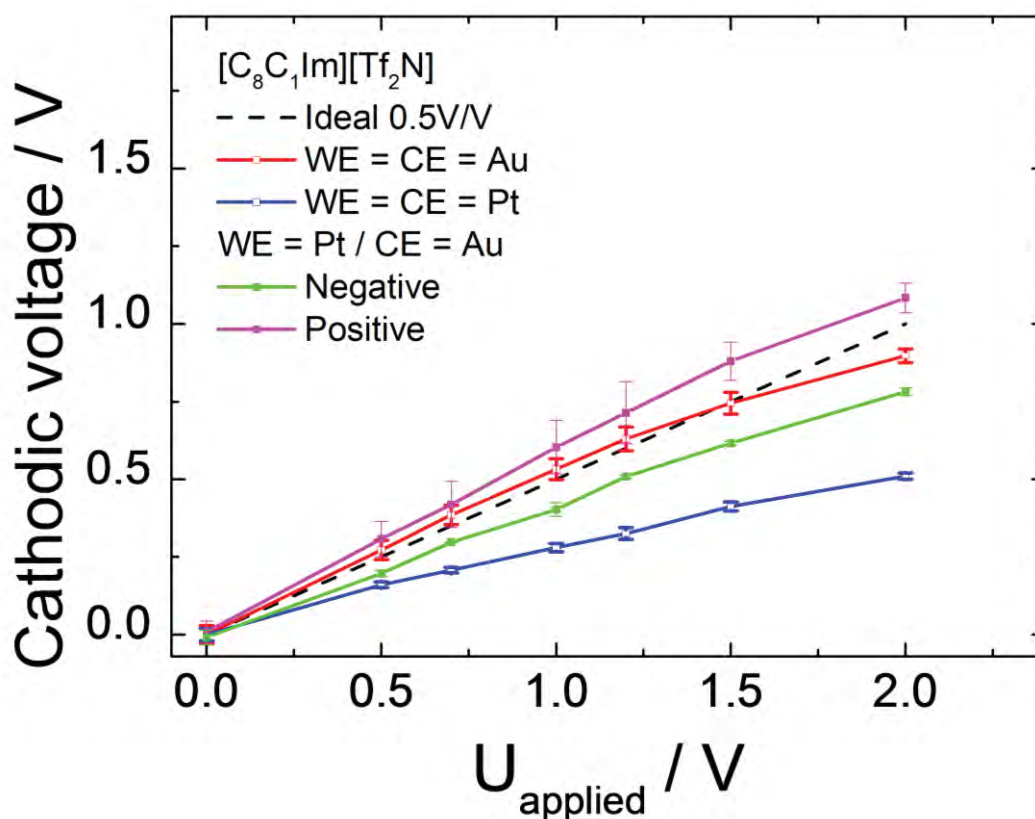
Figure 50 Cathodic voltage of [C$_8$C$_1$Im][Tf$_2$N] versus applied voltage, for two identical Au WE and CE (red); for two identical Pt WE and CE (blue); for Pt WE and Au CE at negative (green) and positive polarizations (magenta). Equal potential drops at the anode and cathode interfaces are indicated as dashed straight line with a slope of +0.5 V/V. The error bars show standard deviations of the measurements.

In the asymmetric cell setup (WE = Pt; CE = Au), the PS curve shows a slope of 0.40 V/V for negative polarization (see Figure 50 green line), that is, $\Delta\varphi_{\text{cathodic}} < \Delta\varphi_{\text{anodic}}$. This behavior is tentatively assigned to strong interactions between the Pt electrode and the imidazolium ring leading to a smaller distance d_{cathodic} of the [C$_8$C$_1$Im]$^+$ at the Pt cathode than the larger [Tf$_2$N]$^-$ at the Au anode, similar to the case of the symmetric cell with two identical Pt electrodes. For positive polarization (see Figure 50 magenta line), the PS curve exhibits a slightly larger $\Delta\varphi_{\text{cathodic}}$ than $\Delta\varphi_{\text{anodic}}$ with a slope of 0.55 V/V. Here, the interpretation is complicated by the fact that in absence of specific adsorption, the size of [C$_8$C$_1$Im]$^+$ on Au and [Tf$_2$N]$^-$ on Pt would be expected to be similar. Therefore, the explanation used for the symmetric cell with two identical electrodes is not sufficient anymore to fully explain the behavior of PS at positive polarizations. However, for the exploratory scope of this chapter, these first

experiments show that combining electrodes of different materials can be used to successfully tune the potential drop at the EDL in IL electrolytes, e.g., from a slope of 0.27 V/V for two Pt electrodes to a nearly symmetric behavior (0.55 V/V) for mixed Pt/Au electrodes.

To further explore how the properties of an IL are affecting the PS behavior in an asymmetric cell, we performed the same set of measurements as above with $[C_8C_1Im]Cl$. As already presented in Chapter 3 and shown in Figure 51, $[C_8C_1Im]Cl$ with two identical Pt electrodes (blue line) is characterized by a slope of 0.12 V/V which changes to a value of 0.81 V/V above $U_{applied} = 1.2$ V; overall, we always find $\Delta\varphi_{cathodic} < \Delta\varphi_{anodic}$. This behavior was again attributed to typical strong interactions between the aromatic imidazolium ring and the Pt electrode. The PS of the same IL measured with two identical Au electrodes (see Chapter 3 and Figure 51 red line) show again a highly asymmetric behavior with a slope of 0.92 V/V and a $\Delta\varphi_{cathodic} \gg \Delta\varphi_{anodic}$. This strong asymmetry was attributed in Chapter 3 to the small size of the Cl^- compared to the larger $[C_8C_1Im]^+$.

The PS curve measured in the asymmetric cell at negative polarization shows a $\Delta\varphi_{cathodic} \gg \Delta\varphi_{anodic}$ behavior with a slope of 0.89 V/V (Figure 51, green line). This behavior is virtually identical to the one observed with $[C_8C_1Im]Cl$ with two identical Au electrodes. It indicates that for negative polarization of the asymmetrical cell, the EDL formed of Cl^- on Au dominates the overall PS. Such a strong effect on the PS behavior of Cl^- on Au is not surprising and was already observed for IL mixtures and in measurements performed in atmosphere (see Chapters 4 and 5). For positive polarizations (Figure 51, magenta line), that is $[C_8C_1Im]^+$ on Au and Cl^- on Pt, the PS curve shows an initial slope of 0.52 V/V, which changes to a slope of 0.71 V/V above $U_{applied} = 1.2$ V. This virtually symmetric behavior of the PS curve, that is, $\Delta\varphi_{cathodic} \approx \Delta\varphi_{anodic,}$ cannot be simply attributed to the different size or to specific adsorption of the counterions at the electrodes and more studies are needed to fully understand the nature of the EDL at both interfaces. However, this experiment clearly demonstrates that at negative polarizations the potential drop at the IL/electrode interface can be tuned from highly asymmetric to symmetric simply by changing the material of one of the electrodes.

In the following, some more considerations will be added on the equalization of the potential drop at cathode and anode using the example of $[C_8C_1Im]Cl$.
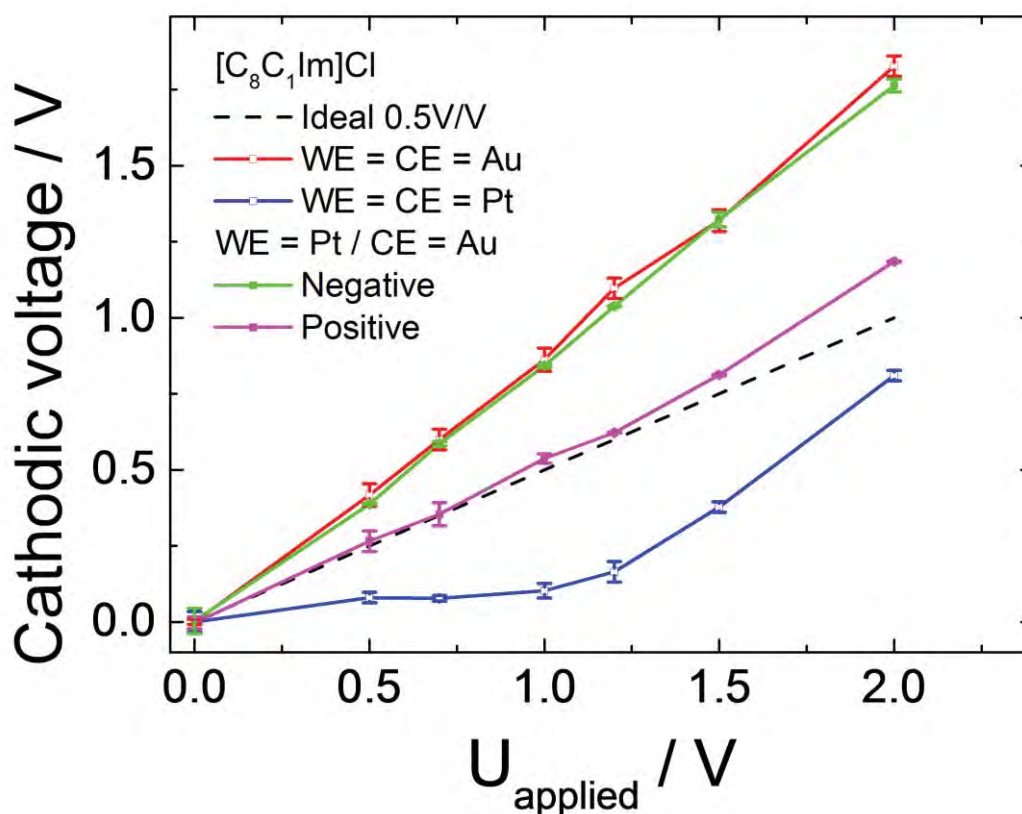
Figure 51 Cathodic voltage of [C₈C₁Im]Cl versus applied voltage, for two identical Au WE and CE (red); for two identical Pt WE and CE (blue); for Pt WE and Au CE at negative (green) and positive (magenta) polarizations. Equal potential drops at the anode and cathode interfaces are indicated as dashed straight line with a slope of +0.5 V/V. The error bars show standard deviations of the measurements.

As already emphasized, the sum of the potential drop at the cathode and the anode is always equal to the applied voltage ($U_{applied} = \Delta\varphi_{cathodic} + \Delta\varphi_{anodic}$). Consequently, the low $\Delta\varphi_{cathodic}$ at the negative electrode, observed with two identical Pt electrodes, implies a corresponding high $\Delta\varphi_{anodic}$ at the positive electrode for the same $U_{applied}$ values. This means that applying higher $U_{applied}$ might lead to irreversible faradaic reactions much earlier at the anode than at the cathode. The situation with two identical Au electrodes in contact with [C₈C₁Im]Cl is inverted: the much larger $\Delta\varphi_{cathodic}$ than $\Delta\varphi_{anodic}$ can lead to irreversible faradaic reactions much earlier at the negative than at the positive electrode. In contrast, the approximately equal $\Delta\varphi_{cathodic}$ and $\Delta\varphi_{anodic}$ values observed with the asymmetric cell at negative polarizations might indicate that a larger electrochemical window can be achieved in this configuration.

6.4.   Conclusions

In this chapter, we explored the effect of combining two different material electrodes on the cathodic and anodic voltage following the *BE* shift with *in-situ* XPS. Three different ILs were studied in an asymmetric two-electrode electrochemical cell comprised of a Pt and an Au electrode with identical size and diameter. The measurements performed with $[C_4C_1Pyrr][Tf_2N]$ are considered as a proof-of-principle experiment to rule out a different roughness of the Au and Pt electrodes, which would lead to different IL/electrode contact areas and consequently different cathodic voltage at positive and negative polarizations. The cathodic voltage curves obtained with $[C_8C_1Im][Tf_2N]$ in the asymmetric cell at negative and positive polarizations exhibit an almost symmetric behavior ($\Delta\varphi_{cathodic} \approx \Delta\varphi_{anodic}$) compared to the symmetric cell with two identical Pt electrodes. In contrast, the extremely asymmetric behaviors of $[C_8C_1Im]Cl$ ($\Delta\varphi_{cathodic} \neq \Delta\varphi_{anodic}$) observed in the symmetric cell with both two identical Pt or Au electrodes remarkably change to highly symmetric in the cell with two different material electrodes at negative polarizations.

In the context of supercapacitors, these findings are important as a symmetric potential drop at both interfaces allows one to take advantage of the full potential windows of the two electrodes and this might result in an expanded operational voltage of the cell and consequently higher energy densities of the device.

7. Summary

Understanding the behavior of ionic liquids (ILs) at electrified interfaces in the context of supercapacitor applications is pivotal to improve performance and stability of such systems. In this context, the studies reported in this thesis aim to provide a molecular-level understanding of various ILs at polarized metal electrodes, mainly by using *in-situ* XPS under ultra-high vacuum (UHV) conditions.

As a first step, we developed a new approach to investigate the interfaces of ILs with charged electrodes in a symmetric two-electrode electrochemical cell setup. The core level binding energy shifts for different IL/electrode combinations measured with *in-situ* XPS gave access to the potential screening (PS) at the solid/liquid interface as a function of applied voltage. For all imidazolium-based ILs studied in contact with Pt electrodes, the PS was found to be significantly larger at the anode than at the cathode, which was attributed to strong attractive interactions between Pt and the imidazolium cation and, thus, to a larger electrical double layer (EDL) capacitance at the cathode than at the anode. For Au electrodes, where no specific ion/electrode interactions occur, we found that the PS behavior is predominantly determined by the different size of cations and anions, which leads to different thicknesses of the formed EDLs: While for ILs with similar size of anion and cation (such as $[C_4C_1Pyrr][Tf_2N]$), PS at both electrodes is of similar magnitude, it becomes asymmetric for different ion sizes (such as $[C_8C_1Im]Cl$, where most of the PS takes place at the cathode).

The very characteristic behavior of the PS curves arising from the specific combination of IL and electrode was then used to characterize the nature of the IL/electrode interfaces for IL mixtures of $[C_8C_1Im][Tf_2N]$ and $[C_8C_1Im]Cl$ on Au and Pt electrodes. *In-situ* XPS measurements in UHV performed in a two-electrode electrochemical cell showed that the PS at the IL-mixture/Au interfaces was dominated by Cl^- anions even down to 0.1 mol% $[C_8C_1Im]Cl$ content. On the other hand, $[Tf_2N]^-$ anions enrich at the IL-mixture/Pt interfaces down to 10 mol% $[C_8C_1Im][Tf_2N]$; only at lower concentrations, a transition to a Cl^- enrichment occurred. These results demonstrated that even small concentrations of another IL or contaminations can strongly influence the composition of ILs at charged interfaces.

To further investigate the role of contaminations at the IL/electrode interface, we studied the influence of ambient conditions on the PS at the interfaces of Au and Pt electrodes

with the ionic liquids $[C_8C_1Im][Tf_2N]$ and $[C_8C_1Im]Cl$. These studies were based on a proof-of-principle experiment, which showed that PS measurements performed by XPS yield the same results as measurements using a specific 3-electrode sample holder setup, both in UHV. Based on this control experiment, we were able to compare the PS measurements obtained under the ultraclean conditions of UHV by XPS with PS measurements with a 3-electrode setup in N_2 and in air. We found for Pt electrodes a more pronounced influence of the ambient conditions on the PS for both $[C_8C_1Im][Tf_2N]$ and $[C_8C_1Im]Cl$ in comparison to Au electrodes. We attributed the observed effects mainly to water affecting the EDLs at the IL/electrode interfaces. In addition, we observed that products of faradaic reactions occurring in air can lead to a consecutive contamination of the 3rd electrode (reference electrode), yielding time-dependent deviations from the true PS behavior.

Finally, the combination of two different material electrodes on PS behavior was explored following the binding energy shift with *in-situ* XPS in UHV. $[C_4C_1Pyrr][Tf_2N]$, $[C_8C_1Im][Tf_2N]$ and $[C_8C_1Im]Cl$ were studied in an asymmetric two-electrode electrochemical cell comprised of a Pt and an Au electrode. The measurements performed with $[C_4C_1Pyrr][Tf_2N]$ in such asymmetric cell were used as proof-of-principle experiment; moreover, a different IL/electrode contact area originating from a possible different roughness of the Au and Pt electrodes could be excluded. For $[C_8C_1Im][Tf_2N]$ and $[C_8C_1Im]Cl$, the PS behavior measured with the asymmetric cell was found to be dependent on the polarization of the electrodes. The PS curves obtained with $[C_8C_1Im][Tf_2N]$ in the asymmetric cell at negative and positive polarizations exhibit an almost symmetric behavior compared to the symmetric cell with two identical Pt electrodes. In contrast, the extremely asymmetric behaviors of $[C_8C_1Im]Cl$ observed in the symmetric cell with both two identical Pt or Au electrodes remarkably change to highly symmetric in the cell with two different material electrodes at negative polarizations. The obtained results show that tuning the PS at the IL/electrode interface by combining two electrodes of different materials in an asymmetric electrochemical cell might be a route towards improving the performance of electrochemical devices such as supercapacitors.

8. Zusammenfassung

Das Verständnis des Verhaltens ionischer Flüssigkeiten (engl. ionic liquids, ILs) an elektrifizierten Grenzflächen im Zusammenhang mit Superkondensatoranwendungen ist entscheidend für die Verbesserung der Leistung und Stabilität solcher Systeme. In diesem Zusammenhang zielen die hier vorgestellten Untersuchungen darauf ab, ein Verständnis auf molekularer Ebene für das Verhalten verschiedener ILs an polarisierten Metallelektroden zu erlangen. Als experimentelle Methode kam hauptsächlich *in-situ* XPS unter Ultrahochvakuum (UHV) Bedingungen zum Einsatz.

In einem ersten Schritt haben wir einen neuen Ansatz entwickelt, um die Grenzflächen von ILs mit geladenen Elektroden in einer symmetrischen elektrochemischen Zelle mit zwei Elektroden zu untersuchen. Die Verschiebungen der Rumpfniveau-Bindungsenergien (engl. chemical shifts) für verschiedene IL/Elektroden-Kombinationen, die mit *in-situ*-XPS gemessen wurden, geben Aufschluss über die Potenzialabschirmung (engl. potential screening, PS) an der fest/flüssig-Grenzfläche in Abhängigkeit von der angelegten Spannung. Alle hier untersuchten Imidazolium-basierten ILs in Kontakt mit Pt-Elektroden zeigen an der Anode ein deutlich größeres PS als an der Kathode. Dies wird auf starke anziehende Wechselwirkungen zwischen Pt und dem Imidazoliumkation und somit auf eine größere elektrische Doppelschichtkapazität (engl. electrical double layer, EDL) an der Kathode als an der Anode zurückgeführt. Für Au-Elektroden, bei denen keine spezifischen Ionen/Elektroden-Wechselwirkungen auftreten, wird das PS-Verhalten hauptsächlich durch die unterschiedliche Größe der Kationen und Anionen bestimmt, was zu unterschiedlichen Dicken der gebildeten EDLs führt: Während bei ILs mit ähnlicher Anionen- und Kationengröße (wie z. B. $[C_4C_1Pyrr][Tf_2N]$) das PS an beiden Elektroden ähnlich groß ist, wird es bei unterschiedlichen Ionengrößen stark asymmetrisch, so etwa bei $[C_8C_1Im]Cl$, wo der Hauptteil des PS an der Au-Kathode beobachtet wird.

Das sehr charakteristische Verhalten der PS-Kurven, das sich aus der spezifischen Kombination von IL und Elektrode ergibt, wurde dann genutzt, um die Beschaffenheit der IL/Elektroden-Grenzflächen für Mischungen der ILs $[C_8C_1Im][Tf_2N]$ und $[C_8C_1Im]Cl$ im Kontakt mit Au- und Pt-Elektroden zu charakterisieren. *In-situ*-XPS-Messungen im UHV, die in einer elektrochemischen Zelle mit zwei Elektroden durchgeführt wurden, zeigen, dass das

PS an den IL-Mischungen/Au-Grenzflächen selbst bei einem [C$_8$C$_1$Im]Cl-Gehalt von nur 0,1 mol% von Cl$^-$ Anionen dominiert wird. Andererseits reichern sich [Tf$_2$N]$^-$ Anionen im Fall der IL-Mischungen an der Pt-Grenzfläche bis hinunter zu 10 mol% Anteil von [C$_8$C$_1$Im][Tf$_2$N] an; erst bei noch niedrigeren Konzentrationen erfolgt ein Übergang zu einer verstärkten Präsenz von Cl$^-$ Anionen an dieser Grenzfläche. Diese Ergebnisse zeigen, dass selbst geringe Konzentrationen einer anderen IL oder Verunreinigungen im Volumen die Zusammensetzung der IL an geladenen Grenzflächen stark beeinflussen können.

Um die Rolle von Verunreinigungen an der IL/Elektroden-Grenzfläche weiter zu ermitteln, untersuchten wir den Einfluss der Umgebungsbedingungen auf das PS an den Grenzflächen von Au- und Pt-Elektroden mit den ionischen Flüssigkeiten [C$_8$C$_1$Im][Tf$_2$N] und [C$_8$C$_1$Im]Cl. Diese Untersuchungen basierten auf einem Proof-of-Principle-Experiment, das zeigt, dass PS-Messungen mittels XPS die gleichen Ergebnisse liefern wie Messungen mit einem speziellen 3-Elektroden-Probenhalter; die Experimente wurden dabei jeweils im UHV durchgeführt. Auf Grundlage dieses Kontrollexperiments konnten wir die PS-Messungen, die unter den ultrasauberen Bedingungen des UHV mittels XPS durchgeführt wurden, mit PS-Messungen mittels dieses 3-Elektroden-Setups unter Stickstoff-Atmosphäre und an Luft vergleichen. Wir fanden für Pt-Elektroden einen stärkeren Einfluss der Umgebungsbedingungen auf das PS, sowohl für [C$_8$C$_1$Im][Tf$_2$N] als auch für [C$_8$C$_1$Im]Cl, im Vergleich zu Au-Elektroden. Wir führen die beobachteten Effekte hauptsächlich auf die Beeinflussung der EDLs an den IL/Elektroden-Grenzflächen durch Wasser zurück. Darüber hinaus beobachteten wir, dass Produkte von elektrochemischen Reaktionen (engl. faradaic reactions), die unter Laborluft-Bedingungen auftraten, zu einer Verunreinigung der dritten Elektrode (Referenzelektrode) führten, wodurch sich zeitabhängige Abweichungen zum „echten" PS-Verhalten (d.h. gemessen zu Beginn der Messserie) ergaben.

Schließlich wurde das PS-Verhalten für zwei Elektroden aus unterschiedlichen Materialien mittels *in-situ* XPS im UHV charakterisiert. [C$_4$C$_1$Pyrr][Tf$_2$N], [C$_8$C$_1$Im][Tf$_2$N] und [C$_8$C$_1$Im]Cl wurden in einer asymmetrischen elektrochemischen Zelle mit zwei Elektroden untersucht, die aus je einer Pt- und einer Au-Elektrode bestand. Die mit [C$_4$C$_1$Pyrr][Tf$_2$N] in einer solchen asymmetrischen Zelle durchgeführten Messungen dienten als Proof-of-Principle-Experiment; außerdem konnte damit eine unterschiedliche IL/Elektroden-Kontaktfläche aufgrund einer möglichen unterschiedlichen Rauheit der Au- und Pt-Elektroden ausgeschlossen werden. Das mit der asymmetrischen Zelle gemessene PS-Verhalten erwies sich im Fall von [C$_8$C$_1$Im][Tf$_2$N] und von [C$_8$C$_1$Im]Cl abhängig von der Polarisierung der

Elektroden. Die mit $[C_8C_1Im][Tf_2N]$ in der asymmetrischen Zelle bei negativer und positiver Polarisation erhaltenen PS-Kurven zeigen im Vergleich zur symmetrischen Zelle mit zwei identischen Pt-Elektroden ein nahezu symmetrisches Verhalten. Im Gegensatz dazu ändert sich das extrem asymmetrische Verhalten von $[C_8C_1Im]Cl$, das in der symmetrischen Zelle mit zwei identischen Pt- oder Au-Elektroden beobachtet wurde, in der Zelle mit zwei unterschiedlichen Elektroden bei negativer Polarisation der Pt-Elektrode in ein hochsymmetrisches Verhalten. Die erzielten Ergebnisse zeigen, dass die Anpassung des PS an der IL/Elektroden-Grenzfläche durch die Kombination von zwei Elektroden aus unterschiedlichen Materialien in einer asymmetrischen elektrochemischen Zelle ein Weg zur Verbesserung der Leistung von elektrochemischen Superkondensatoren sein könnte.

9. Literature

1. B. Dunn, H. Kamath and J.-M. Tarascon, Electrical Energy Storage for the Grid: A Battery of Choices, *Science*, **2011**, *334*, 928-935.

2. F. Wang, X. Wu, X. Yuan, Z. Liu, Y. Zhang, L. Fu, Y. Zhu, Q. Zhou, Y. Wu and W. Huang, Latest advances in supercapacitors: from new electrode materials to novel device designs, *Chem. Soc. Rev.*, **2017**, *46*, 6816-6854.

3. A. Lewandowski and M. Galiński, Carbon–ionic liquid double-layer capacitors, *J. Phys. Chem. Solids*, **2004**, *65*, 281-286.

4. W. Xing, S. Z. Qiao, R. G. Ding, F. Li, G. Q. Lu, Z. F. Yan and H. M. Cheng, Superior electric double layer capacitors using ordered mesoporous carbons, *Carbon*, **2006**, *44*, 216-224.

5. C. Zhong, Y. Deng, W. Hu, J. Qiao, L. Zhang and J. Zhang, A review of electrolyte materials and compositions for electrochemical supercapacitors, *Chem. Soc. Rev.*, **2015**, *44*, 7484-7539.

6. V. Lockett, M. Horne, R. Sedev, T. Rodopoulos and J. Ralston, Differential capacitance of the double layer at the electrode/ionic liquids interface, *Phys. Chem. Chem. Phys.*, **2010**, *12*, 12499-12512.

7. R. Costa, C. M. Pereira and F. Silva, Double layer in room temperature ionic liquids: influence of temperature and ionic size on the differential capacitance and electrocapillary curves, *Phys. Chem. Chem. Phys.*, **2010**, *12*, 11125-11132.

8. V. Lockett, R. Sedev, J. Ralston, M. Horne and T. Rodopoulos, Differential Capacitance of the Electrical Double Layer in Imidazolium-Based Ionic Liquids: Influence of Potential, Cation Size, and Temperature, *J. Phys. Chem. C.*, **2008**, *112*, 7486-7495.

9. M. M. Islam, M. T. Alam and T. Ohsaka, Electrical Double-Layer Structure in Ionic Liquids: A Corroboration of the Theoretical Model by Experimental Results, *J. Phys. Chem. C.*, **2008**, *112*, 16568-16574.

10. B. Roling, M. Drüschler and B. Huber, Slow and fast capacitive process taking place at the ionic liquid/electrode interface, *Faraday Discuss.*, **2012**, *154*, 303-311.

11. A. A. Kornyshev, Double-layer in ionic liquids: paradigm change?, *J. Phys. Chem. B*, **2007**, *111*, 5545-5557.

12. M. V. Fedorov and A. A. Kornyshev, Ionic liquid near a charged wall: structure and capacitance of electrical double layer, *J. Phys. Chem. B*, **2008**, *112*, 11868-11872.

13. Y. Lauw, M. D. Horne, T. Rodopoulos, A. Nelson and F. A. Leermakers, Electrical double-layer capacitance in room temperature ionic liquids: ion-size and specific adsorption effects, *J. Phys. Chem. B*, **2010**, *114*, 11149-11154.

14. X. Zhang, Y. X. Zhong, J. W. Yan, Y. Z. Su, M. Zhang and B. W. Mao, Probing double layer structures of Au (111)-BMIPF6 ionic liquid interfaces from potential-dependent AFM force curves, *ChemComm*, **2012**, *48*, 582-584.

15. T. Cui, A. Lahiri, T. Carstens, N. Borisenko, G. Pulletikurthi, C. Kuhl and F. Endres, Influence of Water on the Electrified Ionic Liquid/Solid Interface: A Direct Observation of the Transition from a Multilayered Structure to a Double-Layer Structure, *J. Phys. Chem. C.*, **2016**, *120*, 9341-9349.

16. Y. X. Zhong, J. W. Yan, M. G. Li, X. Zhang, D. W. He and B. W. Mao, Resolving fine structures of the electric double layer of electrochemical interfaces in ionic liquids with an AFM tip modification strategy, *J. Am. Chem. Soc.*, **2014**, *136*, 14682-14685.

17. T. A. Petach, A. Mehta, R. Marks, B. Johnson, M. F. Toney and D. Goldhaber-Gordon, Voltage-Controlled Interfacial Layering in an Ionic Liquid on SrTiO3, *ACS Nano*, **2016**, *10*, 4565-4569.

18. M. Mezger, H. Schroder, H. Reichert, S. Schramm, J. S. Okasinski, S. Schoder, V. Honkimaki, M. Deutsch, B. M. Ocko, J. Ralston, M. Rohwerder, M. Stratmann and H. Dosch, Molecular layering of fluorinated ionic liquids at a charged sapphire (0001) surface, *Science*, **2008**, *322*, 424-428.

19. M. Z. Bazant, B. D. Storey and A. A. Kornyshev, Double layer in ionic liquids: overscreening versus crowding, *Phys. Rev. Lett.*, **2011**, *106*, 046102.

20. C. Noh and Y. Jung, Understanding the charging dynamics of an ionic liquid electric double layer capacitor via molecular dynamics simulations, *Phys. Chem. Chem. Phys.*, **2019**, *21*, 6790-6800.

21. J. Vatamanu, O. Borodin and G. D. Smith, Molecular insights into the potential and temperature dependences of the differential capacitance of a room-temperature ionic liquid at graphite electrodes, *J. Am. Chem. Soc.*, **2010**, *132*, 14825-14833.

22. E. F. Smith, I. J. Villar Garcia, D. Briggs and P. Licence, Ionic liquids in vacuo; solution-phase X-ray photoelectron spectroscopy, *ChemComm*, **2005**, 5633-5635.

23. O. Höfft, S. Bahr, M. Himmerlich, S. Krischok, J. A. Schaefer and V. Kempter, Electronic Structure of the Surface of the Ionic Liquid [EMIM][Tf2N] Studied by Metastable Impact Electron Spectroscopy (MIES), UPS, and XPS, *Langmuir*, **2006**, *22*, 7120-7123.

24. K. R. J. Lovelock, I. J. Villar-Garcia, F. Maier, H.-P. Steinrück and P. Licence, Photoelectron Spectroscopy of Ionic Liquid-Based Interfaces, *Chem. Rev.*, **2010**, *110*, 5158-5190.

25. V. Lockett, R. Sedev, S. Harmer, J. Ralston, M. Horne and T. Rodopoulos, Orientation and mutual location of ions at the surface of ionic liquids, *Phys. Chem. Chem. Phys.*, **2010**, *12*, 13816-13827.

26. T. Hammer, M. Reichelt and H. Morgner, Influence of the aliphatic chain length of imidazolium based ionic liquids on the surface structure, *Phys. Chem. Chem. Phys.*, **2010**, *12*, 11070-11080.

27. F. Maier, T. Cremer, C. Kolbeck, K. R. J. Lovelock, N. Paape, P. S. Schulz, P. Wasserscheid and H.-P. Steinrück, Insights into the surface composition and enrichment effects of ionic liquids and ionic liquid mixtures, *Phys. Chem. Chem. Phys.*, **2010**, *12*, 1905-1915.

28. C. Kolbeck, I. Niedermaier, N. Taccardi, P. S. Schulz, F. Maier, P. Wasserscheid and H.-P. Steinrück, Monitoring of Liquid-Phase Organic Reactions by Photoelectron Spectroscopy, *Angew. Chem. Int. Ed.*, **2012**, *51*, 2610-2613.

29. I. Niedermaier, M. Bahlmann, C. Papp, C. Kolbeck, W. Wei, S. Krick Calderón, M. Grabau, P. S. Schulz, P. Wasserscheid and H.-P. Steinrück, Carbon dioxide capture by an amine functionalized ionic liquid: fundamental differences of surface and bulk behavior, *J. Am. Chem. Soc.*, **2014**, *136*, 436-441.

30. K. L. Van Aken, M. Beidaghi and Y. Gogotsi, Formulation of ionic-liquid electrolyte to expand the voltage window of supercapacitors, *Angew. Chem. Int. Ed.*, **2015**, *54*, 4806-4809.

31. X. Wang, A. Y. Mehandzhiyski, B. Arstad, K. L. Van Aken, T. S. Mathis, A. Gallegos, Z. Tian, D. Ren, E. Sheridan, B. A. Grimes, D. E. Jiang, J. Wu, Y. Gogotsi and D. Chen, Selective Charging Behavior in an Ionic Mixture Electrolyte-Supercapacitor System for Higher Energy and Power, *J. Am. Chem. Soc.*, **2017**, *139*, 18681-18687.

32. Y. Shao, M. F. El-Kady, J. Sun, Y. Li, Q. Zhang, M. Zhu, H. Wang, B. Dunn and R. B. Kaner, Design and Mechanisms of Asymmetric Supercapacitors, *Chem. Rev.*, **2018**, *118*, 9233-9280.

33. H. Helmholtz, Ueber einige Gesetze der Vertheilung elektrischer Ströme in körperlichen Leitern mit Anwendung auf die thierisch-elektrischen Versuche, *Ann. Phys.*, **1853**, *165*, 211-233.

34. H. Helmholtz, Studien über electrische Grenzschichten, *Ann. Phys.*, **1879**, *243*, 337-382.

35. M. Gouy, Sur la constitution de la charge électrique à la surface d'un électrolyte, *J. Phys. Theor. Appl.*, **1910**, *9*, 457-468.

36. D. L. Chapman, LI. A contribution to the theory of electrocapillarity, *Philos. Mag.*, **1913**, *25*, 475-481.

37. O. Stern, Zur theorie der elektrolytischen doppelschicht, *Z. Elektrochem.*, **1924**, *30*, 508-516.

38. H. Hertz, Ueber einen Einfluss des ultravioletten Lichtes auf die elektrische Entladung, *Ann. Phys.*, **1887**, *267*, 983-1000.

39. W. Hallwachs, Ueber den Einfluss des Lichtes auf electrostatisch geladene Körper, *Ann. Phys.*, **1888**, *269*, 301-312.

40. A. Einstein, Über einen die Erzeugung und Verwandlung des Lichtes betreffenden heuristischen Gesichtspunkt, *Ann. Phys.*, **1905**, *322*, 132-148.

41. V. Lockett, M. Horne, R. Sedev, T. Rodopoulos and J. Ralston, Differential capacitance of the double layer at the electrode/ionic liquids interface, *Phys. Chem. Chem. Phys.*, **2010**, *12*, 12499-12512.

42. M. Drüschler, N. Borisenko, J. Wallauer, C. Winter, B. Huber, F. Endres and B. Roling, New insights into the interface between a single-crystalline metal electrode and an extremely pure ionic liquid: slow interfacial processes and the influence of temperature on interfacial dynamics, *Phys. Chem. Chem. Phys.*, **2012**, *14*, 5090-5099.

43. Q. Zhang, Y. N. Han, Y. L. Wang, S. H. Ye and T. Y. Yan, Comparing the differential capacitance of two ionic liquid electrolytes: Effects of specific adsorption, *Electrochem. Commun.*, **2014**, *38*, 44-46.

44.   M. V. Fedorov and A. A. Kornyshev, Ionic liquids at electrified interfaces, *Chem. Rev.*, **2014**, *114*, 2978-3036.

45.   S. Lamperski, C. W. Outhwaite and L. B. Bhuiyan, The electric double-layer differential capacitance at and near zero surface charge for a restricted primitive model electrolyte, *J. Phys. Chem. B*, **2009**, *113*, 8925-8929.

46.   M. V. Fedorov, N. Georgi and A. A. Kornyshev, Double layer in ionic liquids: The nature of the camel shape of capacitance, *Electrochem. Commun.*, **2010**, *12*, 296-299.

47.   C. Merlet, D. T. Limmer, M. Salanne, R. van Roij, P. A. Madden, D. Chandler and B. Rotenberg, The Electric Double Layer Has a Life of Its Own, *J. Phys. Chem. C*, **2014**, *118*, 18291-18298.

48.   X. Si, S. Li, Y. Wang, S. Ye and T. Yan, Effects of specific adsorption on the differential capacitance of imidazolium-based ionic liquid electrolytes, *ChemPhysChem*, **2012**, *13*, 1671-1676.

49.   J. Zheng, S. S. Moganty, P. C. Goonetilleke, R. E. Baltus and D. Roy, A Comparative Study of the Electrochemical Characteristics of [Emim+][BF4−] and [Bmim+][BF4−] Ionic Liquids at the Surfaces of Carbon Nanotube and Glassy Carbon Electrodes, *J. Phys. Chem. C*, **2011**, *115*, 7527-7537.

50.   J. P. Zheng, P. C. Goonetilleke, C. M. Pettit and D. Roy, Probing the electrochemical double layer of an ionic liquid using voltammetry and impedance spectroscopy: A comparative study of carbon nanotube and glassy carbon electrodes in [EMIM]+[EtSO4]−, *Talanta*, **2010**, *81*, 1045-1055.

51.   S. Baldelli, Surface structure at the ionic liquid-electrified metal interface, *Acc. Chem. Res.*, **2008**, *41*, 421-431.

52.   S. Xu, S. Xing, S.-S. Pei, V. Ivaništšev, R. Lynden-Bell and S. Baldelli, Molecular Response of 1-Butyl-3-Methylimidazolium Dicyanamide Ionic Liquid at the Graphene Electrode Interface Investigated by Sum Frequency Generation Spectroscopy and Molecular Dynamics Simulations, *J. Phys. Chem. C*, **2015**, *119*, 26009-26019.

53.   R. Yamamoto, H. Morisaki, O. Sakata, H. Shimotani, H. Yuan, Y. Iwasa, T. Kimura and Y. Wakabayashi, External electric field dependence of the structure of the electric double layer at an ionic liquid/Au interface, *App. Phys. Lett.*, **2012**, *101*, 053122.

54.   A. Uysal, H. Zhou, G. Feng, S. S. Lee, S. Li, P. Fenter, P. T. Cummings, P. F. Fulvio, S. Dai and J. K. McDonough, Structural origins of potential dependent hysteresis at the electrified graphene/ionic liquid interface, *J. Phys. Chem. C*, **2013**, *118*, 569-574.

55.   Y.-Z. Su, Y.-C. Fu, J.-W. Yan, Z.-B. Chen and B.-W. Mao, Double Layer of Au(100)/Ionic Liquid Interface and Its Stability in Imidazolium-Based Ionic Liquids, *Angew. Chem. Int. Ed.*, **2009**, *48*, 5148-5151.

56.   R. Wen, B. Rahn and O. M. Magnussen, Potential-Dependent Adlayer Structure and Dynamics at the Ionic Liquid/Au(111) Interface: A Molecular-Scale In Situ Video-STM Study, *Angew. Chem. Int. Ed.*, **2015**, *54*, 6062-6066.

57.   F. Endres, N. Borisenko, S. Z. El Abedin, R. Hayes and R. Atkin, The interface ionic liquid(s)/electrode(s): In situSTM and AFM measurements, *Faraday Discuss.*, **2012**, *154*, 221-233.

58.   H. Li, F. Endres and R. Atkin, Effect of alkyl chain length and anion species on the interfacial nanostructure of ionic liquids at the Au(111)–ionic liquid interface as a function of potential, *Phys. Chem. Chem. Phys.*, **2013**, *15*, 14624-14633.

59.   N. Nishi, K. Minami, K. Motobayashi, M. Osawa and T. Sakka, Interfacial Structure at the Quaternary Ammonium-Based Ionic Liquids|Gold Electrode Interface Probed by Surface-Enhanced Infrared Absorption Spectroscopy: Anion Dependence of the Cationic Behavior, *J. Phys. Chem. C*, **2017**, *121*, 1658-1666.

60.   T. Romann, O. Oll, P. Pikma, H. Tamme and E. Lust, Surface chemistry of carbon electrodes in 1-ethyl-3-methylimidazolium tetrafluoroborate ionic liquid – an in situ infrared study, *Electrochim. Acta*, **2014**, *125*, 183-190.

61.   K. Motobayashi, K. Minami, N. Nishi, T. Sakka and M. Osawa, Hysteresis of Potential-Dependent Changes in Ion Density and Structure of an Ionic Liquid on a Gold Electrode: In Situ Observation by Surface-Enhanced Infrared Absorption Spectroscopy, *J. Phys. Chem. Lett.*, **2013**, *4*, 3110-3114.

62.   O. Brummel, F. Faisal, T. Bauer, K. Pohako-Esko, P. Wasserscheid and J. Libuda, Ionic Liquid-Modified Electrocatalysts: The Interaction of [C 1 C 2 Im][OTf] with Pt(1 1 1) and its Influence on Methanol Oxidation Studied by Electrochemical IR Spectroscopy, *Electrochim. Acta*, **2016**, *188*, 825-836.

63.   V. O. Santos, Jr., M. B. Alves, M. S. Carvalho, P. A. Suarez and J. C. Rubim, Surface-enhanced Raman scattering at the silver electrode/ionic liquid (BMIPF6) interface, *J. Phys. Chem. B*, **2006**, *110*, 20379-20385.

64.   M. R. Castillo, J. M. Fraile and J. A. Mayoral, Structure and Dynamics of 1-Butyl-3-methylimidazolium Hexafluorophosphate Phases on Silica and Laponite Clay: From Liquid to Solid Behavior, *Langmuir*, **2012**, *28*, 11364-11375.

65.   Y. Z. Su, Y. C. Fu, J. W. Yan, Z. B. Chen and B. W. Mao, Double layer of Au(100)/ionic liquid interface and its stability in imidazolium-based ionic liquids, *Angew. Chem. Int. Ed.*, **2009**, *48*, 5148-5151.

66.   C. Pinilla, M. G. Del Popolo, J. Kohanoff and R. M. Lynden-Bell, Polarization relaxation in an ionic liquid confined between electrified walls, *J. Phys. Chem. B*, **2007**, *111*, 4877-4884.

67.   W. N. Hansen, C. L. Wang and T. W. Humpherys, A study of electrode immersion and emersion, *J. Electroanal. Chem.*, **1978**, *93*, 87-98.

68.   W. N. Hansen, The emersed double layer, *J. Electroanal. Chem.*, **1983**, *150*, 133-140.

69.   R. Kötz, H. Neff and S. Stucki, Anodic Iridium Oxide Films: XPS-Studies of Oxidation State Changes and, *J. Electrochem. Soc.*, **1984**, *131*, 72-77.

70.   A. T. D'Agostino and W. N. Hansen, Observation of systematic electrochemically induced binding energy shift in the XPS spectra of emersed Cs^+ double layer species, *Surf. Sci.*, **1986**, *165*, 268-276.

71.   W. Kautek and J. G. Gordon, XPS Studies on Emersed Silver Electrodes: Coverage and Bonding State of Specifically Adsorbed Chloride, *J. Electrochem. Soc.*, **1990**, *137*, 3405-3409.

72.   D. Hecht and H.-H. Strehblow, A surface analytical investigation of the electrochemical double layer on silver electrodes in chloride solutions, *J. Electroanal. Chem.*, **1997**, *436*, 109-118.

73. D. Lützenkirchen-Hecht and H.-H. Strehblow, Surface analytical investigations of the electrochemical double layer on silver electrodes in alkaline media, *Electrochim. Acta*, **1998**, *43*, 2957-2968.

74. W. Zhou and D. M. Kolb, Influence of an electrostatic potential at the metal/electrolyte interface on the electron binding energy of adsorbates as probed by X-ray photoelectron spectroscopy, *Surf. Sci.*, **2004**, *573*, 176-182.

75. Zhou, T. Baunach, V. Ivanova and D. M. Kolb, Structure and Electrochemistry of 4,4'-Dithiodipyridine Self-Assembled Monolayers in Comparison with 4-Mercaptopyridine Self-Assembled Monolayers on Au(111), *Langmuir*, **2004**, *20*, 4590-4595.

76. S. Haupt and H.-H. Strehblow, The formation of the passive layer on Cr in 0.5 M H2SO4 A combined electrochemical and surface analytical study, *J. Electroanal. Chem.*, **1987**, *228*, 365-392.

77. H.-W. Hoppe and H.-H. Strehblow, XPS and UPS examinations of the formation of passive layers on Ni in 1 M sodium hydroxide and 0.5 M sulphuric acid, *Surf. Interface Anal.*, **1989**, *14*, 121-131.

78. A. Foelske and H.-H. Strehblow, Passivity of cobalt in borate buffer at pH 9.3 studied by x-ray photoelectron spectroscopy, *Surf. Interface Anal.*, **2000**, *29*, 548-555.

79. A. Foelske, J. Kunze and H.-H. Strehblow, Initial stages of hydroxide formation and its reduction on Co(0001) studied by in situ STM and XPS in 0.1 M NaOH, *Surf. Sci.*, **2004**, *554*, 10-24.

80. B. Philippe, M. Hahlin, K. Edström, T. Gustafsson, H. Siegbahn and H. Rensmo, Photoelectron Spectroscopy for Lithium Battery Interface Studies, *J. Electrochem. Soc.*, **2015**, *163*, A178-A191.

81. A. Foelske-Schmitz, D. Weingarth, H. Kaiser and R. Kötz, Quasi in situ XPS study of anion intercalation into HOPG from the ionic liquid [EMIM][BF4], *Electrochem. Commun.*, **2010**, *12*, 1453-1456.

82. A. Foelske-Schmitz, D. Weingarth and R. Kötz, Quasi in situ XPS study of electrochemical oxidation and reduction of highly oriented pyrolytic graphite in [1-ethyl-3-methylimidazolium][BF4] electrolytes, *Electrochim. Acta*, **2011**, *56*, 10321-10331.

83. A. W. Taylor, F. Qiu, I. J. Villar-Garcia and P. Licence, Spectroelectrochemistry at ultrahigh vacuum: in situ monitoring of electrochemically generated species by X-ray photoelectron spectroscopy, *ChemComm*, **2009**, *39*, 5817-5819.

84. F. Qiu, W. T. Alasdair, S. Men, I. J. Villar-Garcia and P. Licence, An ultra high vacuum-spectroelectrochemical study of the dissolution of copper in the ionic liquid (N-ethylacetate)-4-picoliniumbis(trifluoromethylsulfonyl)imid, *Phys. Chem. Chem. Phys.*, **2010**, *12*, 1982-1990.

85. R. Wibowo, L. Aldous, R. M. J. Jacobs, N. S. A. Manan and R. G. Compton, Monitoring potassium metal electrodeposition from an ionic liquid using in situ electrochemical-X-ray photoelectron spectroscopy, *Chem. Phys. Lett.*, **2011**, *509*, 72-76.

86. R. Wibowo, L. Aldous, R. M. J. Jacobs, N. S. A. Manan and R. G. Compton, In situ electrochemical-X-ray Photoelectron Spectroscopy: Rubidium metal deposition from

an ionic liquid in competition with solvent breakdown, *Chem. Phys. Lett.*, **2011**, *517*, 103-107.

87. D. Weingarth, A. Foelske-Schmitz, A. Wokaun and R. Kötz, In situ electrochemical XPS study of the Pt/[EMIM][BF4] system, *Electrochem. Commun.*, **2011**, *13*, 619-622.

88. M. T. Camci, P. Aydogan, B. Ulgut, C. Kocabas and S. Suzer, XPS enables visualization of electrode potential screening in an ionic liquid medium with temporal- and lateral-resolution, *Phys. Chem. Chem. Phys.*, **2016**, *18*, 28434-28440.

89. M. T. Camci, B. Ulgut, C. Kocabas and S. Suzer, XPS investigation of the vacuum interface of an ionic liquid under triangular electrical excitation for slow transients, *Anal. Methods*, **2018**, *10*, 4225-4228.

90. I. Niedermaier, C. Kolbeck, H.-P. Steinrück and F. Maier, Dual analyzer system for surface analysis dedicated for angle-resolved photoelectron spectroscopy at liquid surfaces and interfaces, *Rev. Sci. Instrum.*, **2016**, *87*, 045105.

91. C. Kolbeck, T. Cremer, K. R. Lovelock, N. Paape, P. S. Schulz, P. Wasserscheid, F. Maier and H.-P. Steinrück, Influence of different anions on the surface composition of ionic liquids studied using ARXPS, *J. Phys. Chem. B*, **2009**, *113*, 8682-8688.

92. K. R. J. Lovelock, C. Kolbeck, T. Cremer, N. Paape, P. S. Schulz, P. Wasserscheid, F. Maier and H.-P. Steinrück, Influence of Different Substituents on the Surface Composition of Ionic Liquids Studied Using ARXPS, *J. Phys. Chem. B*, **2009**, *113*, 2854-2864.

93. J. M. Gottfried, F. Maier, J. Rossa, D. Gerhard, P. S. Schulz, P. Wasserscheid and H.-P. Steinrück, Surface Studies on the Ionic Liquid 1-Ethyl-3-Methylimidazolium Ethylsulfate Using X-Ray Photoelectron Spectroscopy (XPS), *Z. Phys. Chem.*, **2006**, *220*, 1439-1453.

94. F. Greco, S. Shin, F. J. Williams, B. S. J. Heller, F. Maier and H.-P. Steinrück, Potential Screening at Electrode/Ionic Liquid Interfaces from In Situ X-ray Photoelectron Spectroscopy, *ChemistryOpen*, **2019**, *8*, 1365-1368.

95. M. Armand, F. Endres, D. R. MacFarlane, H. Ohno and B. Scrosati, Ionic-liquid materials for the electrochemical challenges of the future, *Nat. Mater.*, **2009**, *8*, 621-629.

96. I. Osada, H. de Vries, B. Scrosati and S. Passerini, Ionic-Liquid-Based Polymer Electrolytes for Battery Applications, *Angew. Chem. Int. Ed.*, **2016**, *55*, 500-513.

97. T. Y. Kim, H. W. Lee, M. Stoller, D. R. Dreyer, C. W. Bielawski, R. S. Ruoff and K. S. Suh, High-Performance Supercapacitors Based on Poly(ionic liquid)-Modified Graphene Electrodes, *ACS Nano*, **2011**, *5*, 436-442.

98. A. P. Abbott and K. J. McKenzie, Application of ionic liquids to the electrodeposition of metals, *Phys. Chem. Chem. Phys.*, **2006**, *8*, 4265-4279.

99. M. Jitvisate and J. R. T. Seddon, Direct Measurement of the Differential Capacitance of Solvent-Free and Dilute Ionic Liquids, *J. Phys. Chem. Lett.*, **2018**, *9*, 126-131.

100. B. Uhl, T. Cremer, M. Roos, F. Maier, H.-P. Steinrück and R. J. Behm, At the ionic liquid|metal interface: structure formation and temperature dependent behavior of an ionic liquid adlayer on Au(111), *Phys. Chem. Chem. Phys.*, **2013**, *15*, 17295-17302.

101. I. J. Villar-Garcia, E. F. Smith, A. W. Taylor, F. Qiu, K. R. Lovelock, R. G. Jones and P. Licence, Charging of ionic liquid surfaces under X-ray irradiation: the measurement of absolute binding energies by XPS, *Phys. Chem. Chem. Phys.*, **2011**, *13*, 2797-2808.

102. R. J. Maurer, V. G. Ruiz, J. Camarillo-Cisneros, W. Liu, N. Ferri, K. Reuter and A. Tkatchenko, Adsorption structures and energetics of molecules on metal surfaces: Bridging experiment and theory, *Progr. Surf. Sci.* , **2016**, *91*, 72-100.

103. S. Baldelli, Interfacial Structure of Room-Temperature Ionic Liquids at the Solid–Liquid Interface as Probed by Sum Frequency Generation Spectroscopy, *J. Phys. Chem. Lett.*, **2013**, *4*, 244-252.

104. B. Uhl, H. Huang, D. Alwast, F. Buchner and R. J. Behm, Interaction of ionic liquids with noble metal surfaces: structure formation and stability of [OMIM][TFSA] and [EMIM][TFSA] on Au(111) and Ag(111), *Phys. Chem. Chem. Phys.*, **2015**, *17*, 23816-23832.

105. S. Shin, F. Greco, F. Maier and H.-P. Steinrück, Enrichment effects of ionic liquid mixtures at polarized electrode interfaces monitored by potential screening, *Phys. Chem. Chem. Phys.*, **2021**, *23*, 10756-10762.

106. M. S. Miran, T. Yasuda, M. A. Susan, K. Dokko and M. Watanabe, Binary Protic Ionic Liquid Mixtures as a Proton Conductor: High Fuel Cell Reaction Activity and Facile Proton Transport, *J. Phys. Chem. C.*, **2014**, *118*, 27631-27639.

107. O. Oll, M. Väärtnõu, G. Gorbatovski, J. Zhao, C. Siimenson, L. Siinor, K. Lust, T. Romann, P. Pikma and E. Lust, Adsorption of anions on bismuth and cadmium single crystal plane electrodes from various solvents and ionic liquid mixtures, *Electrochim. Acta*, **2019**, *319*, 895-908.

108. C. Lian, K. Liu, K. L. Van Aken, Y. Gogotsi, D. J. Wesolowski, H. L. Liu, D. E. Jiang and J. Z. Wu, Enhancing the Capacitive Performance of Electric Double-Layer Capacitors with Ionic Liquid Mixtures, *ACS Energy Lett.*, **2016**, *1*, 21-26.

109. R. Costa, C. M. Pereira and A. Fernando Silva, Structural ordering transitions in ionic liquids mixtures, *Electrochem. Commun.*, **2015**, *57*, 10-13.

110. D. J. V. A. dos Santos and M. N. D. S. Cordeiro, Effect of replacing [NTf$_2$] by [PF$_6$] anion on the [BMIm][NTf$_2$] ionic liquid confined by gold, *Mol. Simul.*, **2015**, *41*, 455-462.

111. S. Li, G. Feng, P. F. Fulvio, P. C. Hillesheim, C. Liao, S. Dai and P. T. Cummings, Molecular Dynamics Simulation Study of the Capacitive Performance of a Binary Mixture of Ionic Liquids near an Onion-like Carbon Electrode, *J. Phys. Chem. Lett.*, **2012**, *3*, 2465-2469.

112. M. T. Alam, M. M. Islam, T. Okajima and T. Ohsaka, Electrical Double Layer in Mixtures of Room-Temperature Ionic Liquids, *J. Phys. Chem. C.*, **2009**, *113*, 6596-6601.

113. A. Fang and A. Smolyanitsky, Simulation Study of the Capacitance and Charging Mechanisms of Ionic Liquid Mixtures near Carbon Electrodes, *J. Phys. Chem. C.*, **2019**, *123*, 1610-1618.

114. C. Lian, H. Liu and J. Wu, Ionic Liquid Mixture Expands the Potential Window and Capacitance of a Supercapacitor in Tandem, *J. Phys. Chem. C*, **2018**, *122*, 18304-18310.

115.   M. Lexow, F. Maier and H.-P. Steinrück, Ultrathin ionic liquid films on metal surfaces: adsorption, growth, stability and exchange phenomena, *Adv. Phys.: X*, **2020**, *5*, 1761266.

116.   M. Lexow, B. S. J. Heller, G. Partl, R. G. Bhuin, F. Maier and H.-P. Steinrück, Cation Exchange at the Interfaces of Ultrathin Films of Fluorous Ionic Liquids on Ag(111), *Langmuir*, **2019**, *35*, 398-405.

117.   M. Lexow, B. S. J. Heller, F. Maier and H.-P. Steinrück, Anion Exchange at the Liquid/Solid Interface of Ultrathin Ionic Liquid Films on Ag(111), *ChemPhysChem*, **2018**, *19*, 2978-2984.

118.   R. Hayes, N. Borisenko, B. Corr, G. B. Webber, F. Endres and R. Atkin, Effect of dissolved LiCl on the ionic liquid-Au(111) electrical double layer structure, *ChemComm*, **2012**, *48*, 10246-10248.

119.   Z. C. Shi and J. Lipkowski, Chloride adsorption at the Au(111) electrode surface, *J. Electroanal. Chem.*, **1996**, *403*, 225-239.

120.   A. Ejigu and D. A. Walsh, The Role of Adsorbed Ions during Electrocatalysis in Ionic Liquids, *J. Phys. Chem. C.*, **2014**, *118*, 7414-7422.

121.   M. Chu, M. Miller and P. Dutta, Crowding and Anomalous Capacitance at an Electrode–Ionic Liquid Interface Observed Using Operando X-ray Scattering, *ACS Cent. Sci.*, **2016**, *2*, 175-180.

122.   N. Zhang, X.-R. Wang, Y.-X. Yuan, H.-F. Wang, M.-M. Xu, Z.-G. Ren, J.-L. Yao and R.-A. Gu, Probing double layer structure at Au/[BMIm]BF4 interface by molecular length-dependent SERS Stark effect, *J. Electroanal. Chem.*, **2015**, *751*, 137-143.

123.   F. Greco, D. Hemmeter, S. Shin, H.-P. Steinrück and F. Maier, The Effect of Ambient Conditions on the Potential Screening at Ionic Liquid – Electrode Interfaces, *Journal of Ionic Liquids*, **2022**, *2*, 100019.

124.   F. Endres, Ionic Liquids: Solvents for the Electrodeposition of Metals and Semiconductors, *ChemPhysChem*, **2002**, *3*, 144-154.

125.   N. Karimi, M. Zarrabeitia, A. Mariani, D. Gatti, A. Varzi and S. Passerini, Nonfluorinated Ionic Liquid Electrolytes for Lithium Metal Batteries: Ionic Conduction, Electrochemistry, and Interphase Formation, *Adv. Energy Mater.*, **2021**, *11*, 2003521-2003535.

126.   P. Wasserscheid and T. Welton, *Ionic liquids in synthesis*, John Wiley & Sons, 2008.

127.   K. R. Seddon, A. Stark and M.-J. Torres, Influence of chloride, water, and organic solvents on the physical properties of ionic liquids, *Pure Appl. Chem.*, **2000**, *72*, 2275-2287.

128.   C. Ridings, V. Lockett and G. Andersson, Significant changes of the charge distribution at the surface of an ionic liquid due to the presence of small amounts of water, *Phys. Chem. Chem. Phys.*, **2011**, *13*, 21301-21307.

129.   S. Doblinger, T. J. Donati and D. S. Silvester, Effect of Humidity and Impurities on the Electrochemical Window of Ionic Liquids and Its Implications for Electroanalysis, *J. Phys. Chem. C*, **2020**, *124*, 20309-20319.

130. D. S. Silvester and R. G. Compton, Electrochemistry in Room Temperature Ionic Liquids: A Review and Some Possible Applications, *Z. Phys. Chem.*, **2006**, *220*, 1247-1274.

131. P. C. Howlett, E. I. Izgorodina, M. Forsyth and D. R. MacFarlane, Electrochemistry at Negative Potentials in Bis(trifluoromethanesulfonyl)amide Ionic Liquids, *Z. Phys. Chem.*, **2006**, *220*, 1483-1498.

132. G. Feng, X. Jiang, R. Qiao and A. A. Kornyshev, Water in Ionic Liquids at Electrified Interfaces: The Anatomy of Electrosorption, *ACS Nano*, **2014**, *8*, 11685-11694.

133. Y. Zhong, J. Yan, M. Li, L. Chen and B. Mao, The Electric Double Layer in an Ionic Liquid Incorporated with Water Molecules: Atomic Force Microscopy Force Curve Study, *ChemElectroChem*, **2016**, *3*, 2221-2226.

134. H.-W. Cheng, P. Stock, B. Moeremans, T. Baimpos, X. Banquy, F. U. Renner and M. Valtiner, Characterizing the Influence of Water on Charging and Layering at Electrified Ionic-Liquid/Solid Interfaces, *Adv. Mater. Interfaces*, **2015**, *2*, 1500159-1500167.

135. H. Zhao, L. A. Welch and B. E. Koel, Site-blocking effects of preadsorbed H on Pt (1 1 1) probed by 1, 3-butadiene adsorption and reaction, *Surf. Sci.*, **2009**, *603*, 3355-3360.

136. C. D. Vurdu, The Adsorption and Diffusion Manners of Hydrogen Atoms on Pt (100), Pt (110), and Pt (111) Surfaces, *Adv. Condens. Matter Phys.*, **2018**, *2018*, 1-10.

137. A. Foelske-Schmitz, D. Weingarth, A. Wokaun and R. Kötz, Core Level Data of Ionic Liquids: Monitoring Charging by In Situ Electrochemical X-ray Photoelectron Spectroscopy, *ECS Electrochem. Lett.*, **2013**, *2*, H13-H15.

138. M. R. Lukatskaya, B. Dunn and Y. Gogotsi, Multidimensional materials and device architectures for future hybrid energy storage, *Nat. Commun.*, **2016**, *7*, 1-13.

139. H. Wang, M. Yoshio, A. K. Thapa and H. Nakamura, From symmetric AC/AC to asymmetric AC/graphite, a progress in electrochemical capacitors, *J. Power Sources*, **2007**, *169*, 375-380.

140. Y.-G. Wang, Z.-D. Wang and Y.-Y. Xia, An asymmetric supercapacitor using RuO2/TiO2 nanotube composite and activated carbon electrodes, *Electrochim. Acta*, **2005**, *50*, 5641-5646.

141. J. H. Chae and G. Z. Chen, 1.9V aqueous carbon–carbon supercapacitors with unequal electrode capacitances, *Electrochim. Acta*, **2012**, *86*, 248-254.

10. Acknowledgements

In this part of my thesis I would like to acknowledge all the people who have contributed to the results and supported me in these last years.

First, I would like to thank Prof. Dr. Hans-Peter Steinrück for giving me the opportunity to work at the chair of Physical Chemistry II and for his considerable and valuable scientific guidance and mentorship throughout my time at his chair.

Furthermore, I wish to thank Dr. Florian Maier for his endless support, for the fruitful discussions and for always providing new and interesting ideas.

I am really thankful to Dr. Sunghwan Shin for his unlimited assistance, for the countless scientific discussion and for the great time spent working together in the lab.

I also want to thank Prof. Dr. Federico Williams for the fruitful collaboration and for the contagious enthusiasm with which he joined my PhD project.

I would like to express my gratitude to the former, visiting and actual members of the "extended" IL-group for the great working atmosphere as well as for the scientific discussions and their assistance whenever was needed: Afra Gezmis, Benjamin May, Bettina Heller, Damian Rodriguez, Daniel Hemmeter, Florian Rietzler, Inga Niedermaier, Leonhard Winter, Manuel Meusel, Matthias Lexow, Patrick Schreiber, Radha Bhuin, Rajan Adhikari, Simon Jäckel, Stephen Massicot, Timo Talwar, Tomoya Sasaki and Ulrike Paap.

I want to thank Hans-Peter Bäumler, Bernd Kreß, Friedhold Wölfel and the mechanical workshop for their outstanding technical support as well as for repairing and building all kind of devices.

Special thanks go to the whole Physical Chemistry II group for the pleasant working atmosphere.

Last but not least, I would like to thank my parents, my sisters, my partner Françoise and all my friends for always supporting and encouraging me during these years.

11. Appendix

11.1. Appendix to Chapter 3

Figure A1 Electrochemical cell used for the potential screening measurements before filling IL (left) and after filling IL (right).
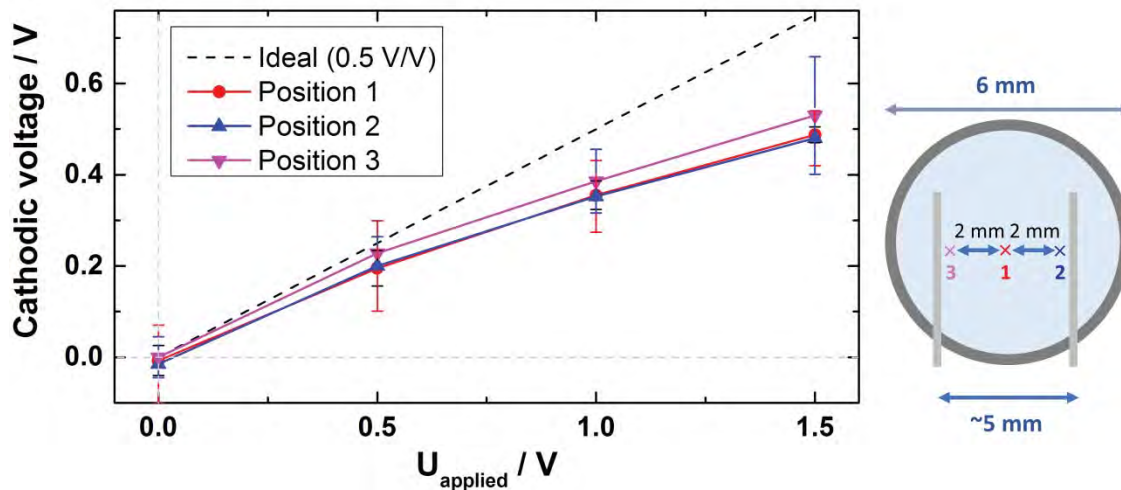
Figure A2 (Left) Cathodic voltage of [C₁C₁Im][Tf₂N] at different probing positions between Pt electrodes. (Right) Schematic sketch of XPS probing positions. In case of an ohmic drop between the electrodes, the potential of the IL should change depending on the position, with the XPS peak shifting accordingly. Our data show that the XP peaks did not change depending on the probing positions, which implies that no ohmic drop exists between the electrodes.
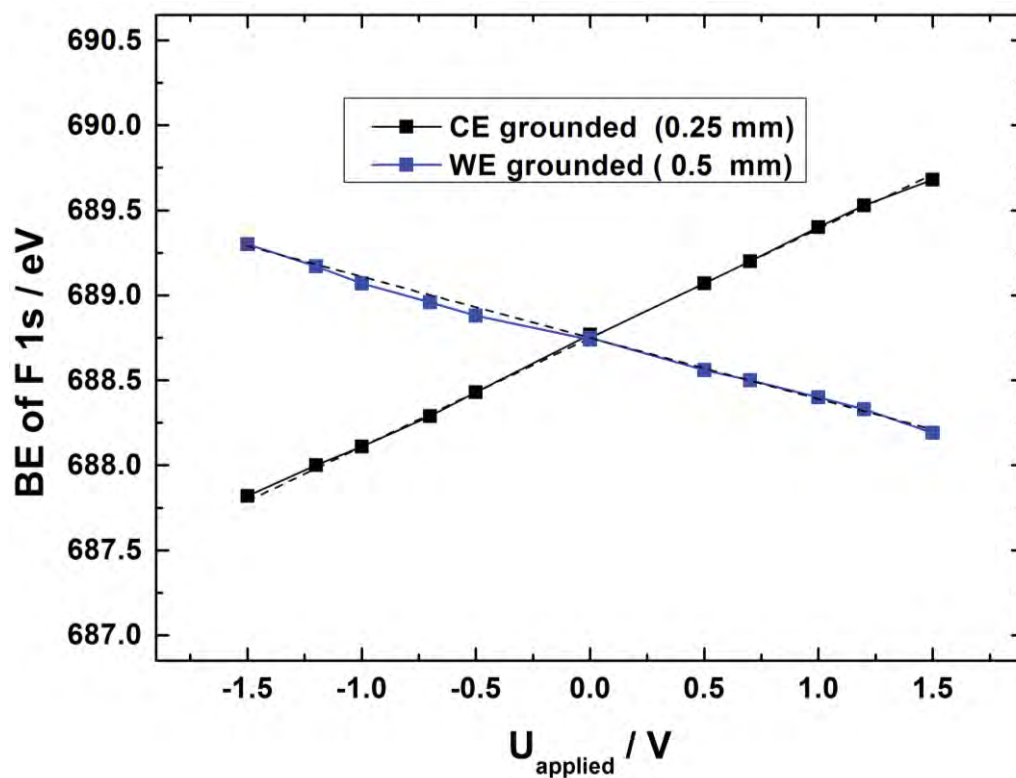
Figure A3 BE of F 1s in [C₁C₁Im][Tf₂N] with different size Au electrodes. CE: 0.25 mm diameter, WE: 0.5 mm diameter. The linear fittings are indicated as dashed lines with a 0.64 eV/V slope for CE grounded and a −0.36 eV/V for WE grounded. According to a parallel plate capacitor model, the capacitance of the EDL is proportional to the surface area of the electrode and the potential screening is inversely proportional to the surface area of the electrodes. The expected slopes from this model are 0.67 eV/V and −0.33 eV/V, respectively. Our results coincide with the predicted values within less than 10% error
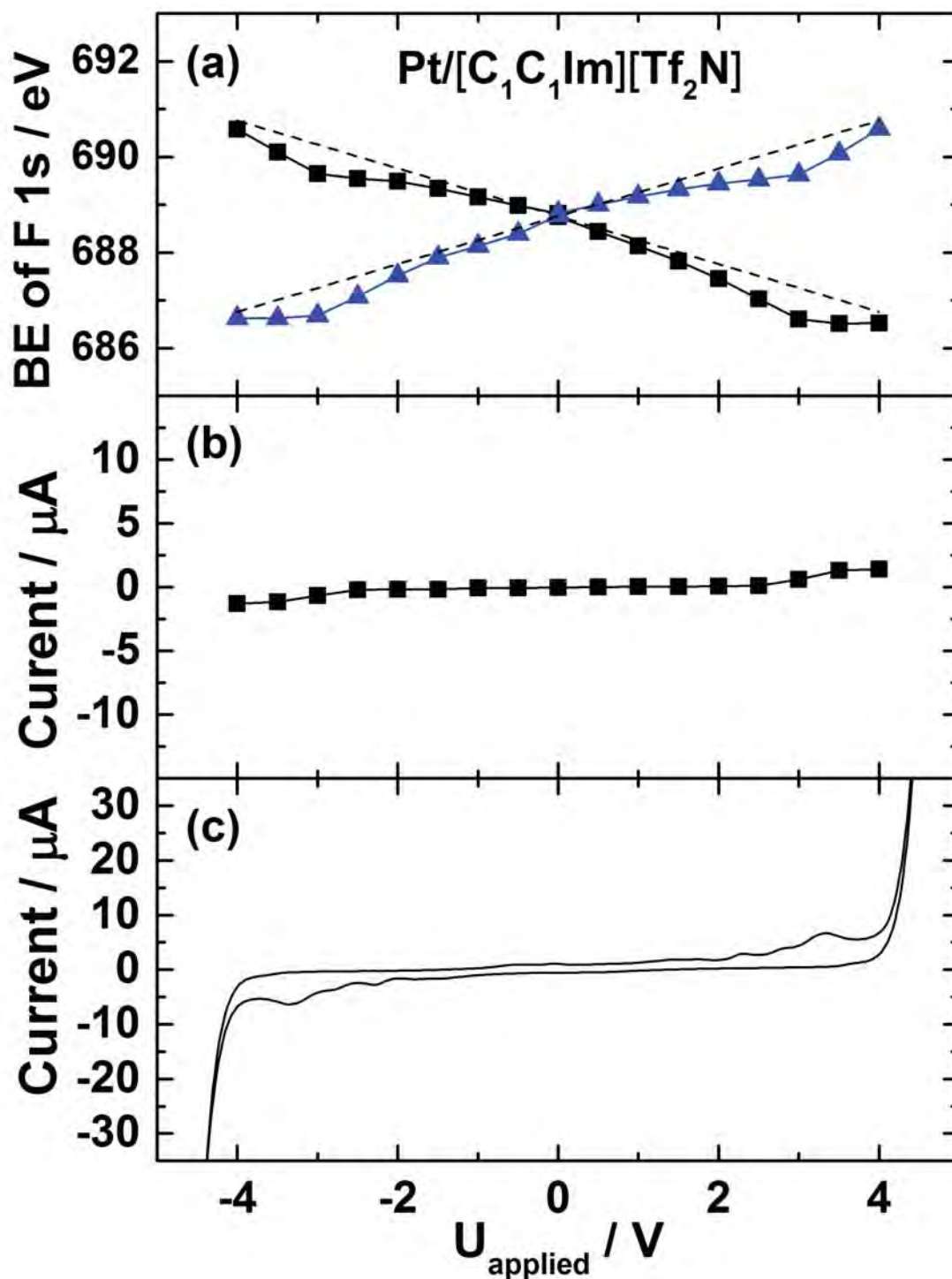
Figure A4 (a) BE of F 1s in [C₁C₁Im][Tf₂N] XP spectra according to $U_{applied}$ in the cases of a Pt WE-grounded (d=0.3 mm) (black square) and a Pt CE-grounded (d=0.3 mm) (blue triangle) setups. The ideal lines are indicated as dashed lines. (b) Residual current at a constant $U_{applied}$ during the XPS measurement. (c) Potential sweep measurement. The ramping rate is 50 mV/s.
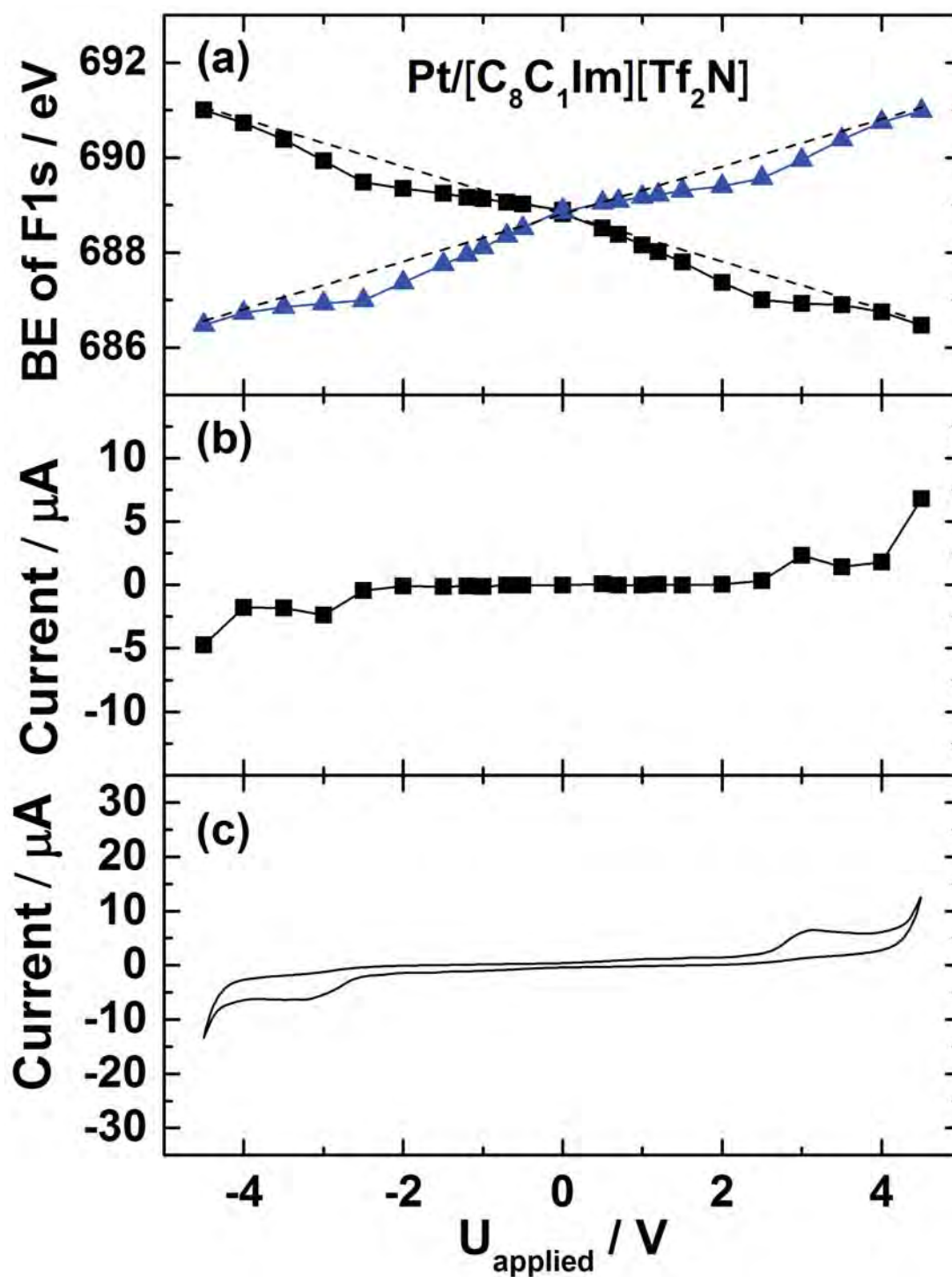
Figure A5 (a) BE of F 1s in [C$_8$C$_1$Im][Tf$_2$N] XP spectra according to U$_{applied}$ in the cases of a Pt WE-grounded (d=0.3 mm) (black square) and a Pt CE-grounded (d=0.3 mm) (blue triangle) setups. The ideal lines are indicated as dashed lines. (b) Residual current at a constant U$_{applied}$ during the XPS measurement. (c) Potential sweep measurement. The ramping rate is 50 mV/s.
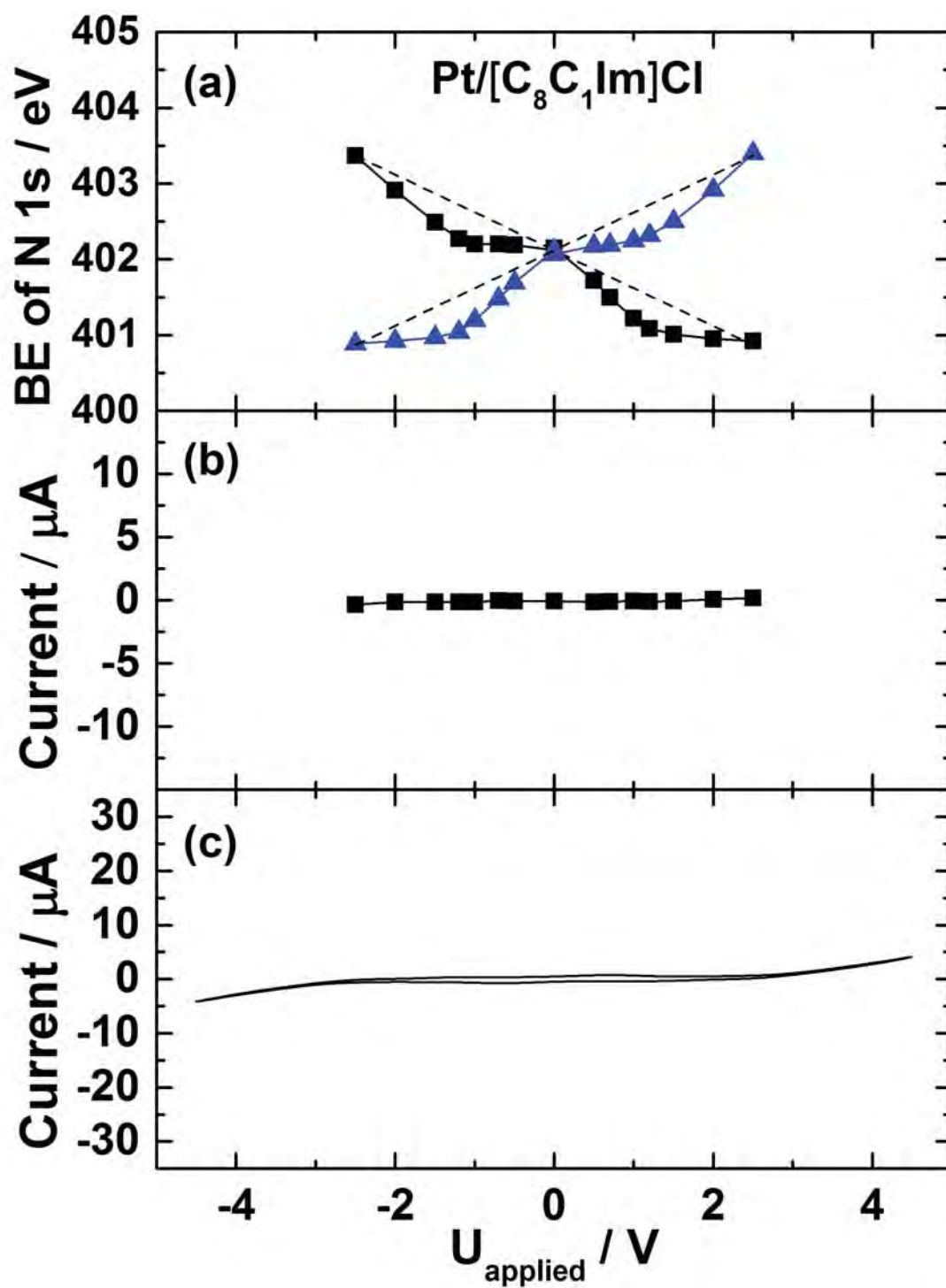
Figure A6 a) BE of N 1s in [C₈C₁Im]Cl XP spectra according to U_applied in the cases of a Pt WE-grounded (d=0.3 mm) (black square) and a Pt CE-grounded (d=0.3 mm) (blue triangle) setups. The ideal lines are indicated as dashed lines. (b) Residual current at a constant U_applied during the XPS measurement. (c) Potential sweep measurement. The ramping rate is 50 mV/s.
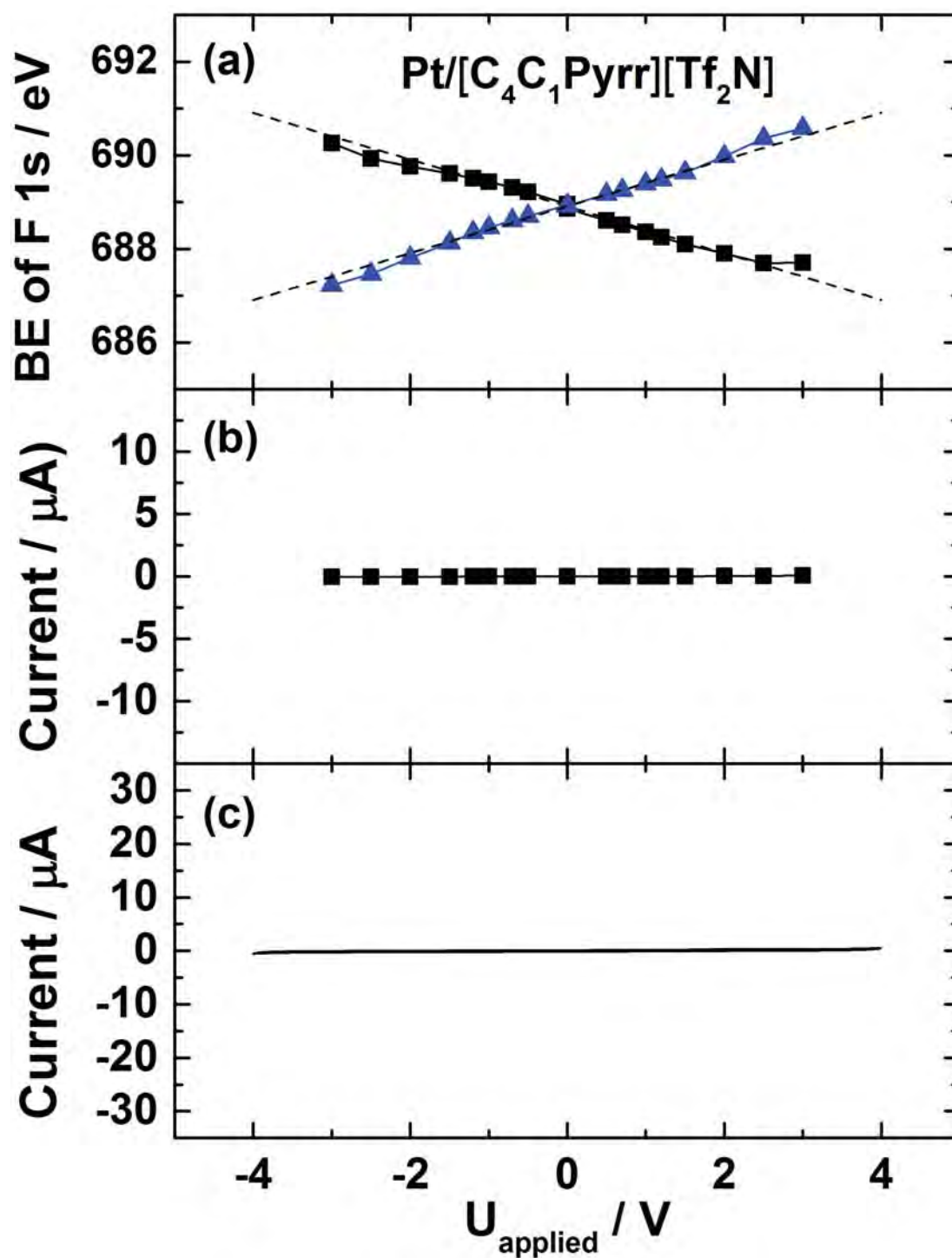
Figure A7 BE of F 1s in [C₄C₁Pyrr][Tf₂N] XP spectra according to $U_{applied}$ in the cases of a Pt WE-grounded (d=0.3 mm) (black square) and a Pt CE-grounded (d=0.3 mm) (blue triangle) setups. The ideal lines are indicated as dashed lines. (b) Residual current at a constant $U_{applied}$ during the XPS measurement. (c) Potential sweep measurement. The ramping rate is 50 mV/s.
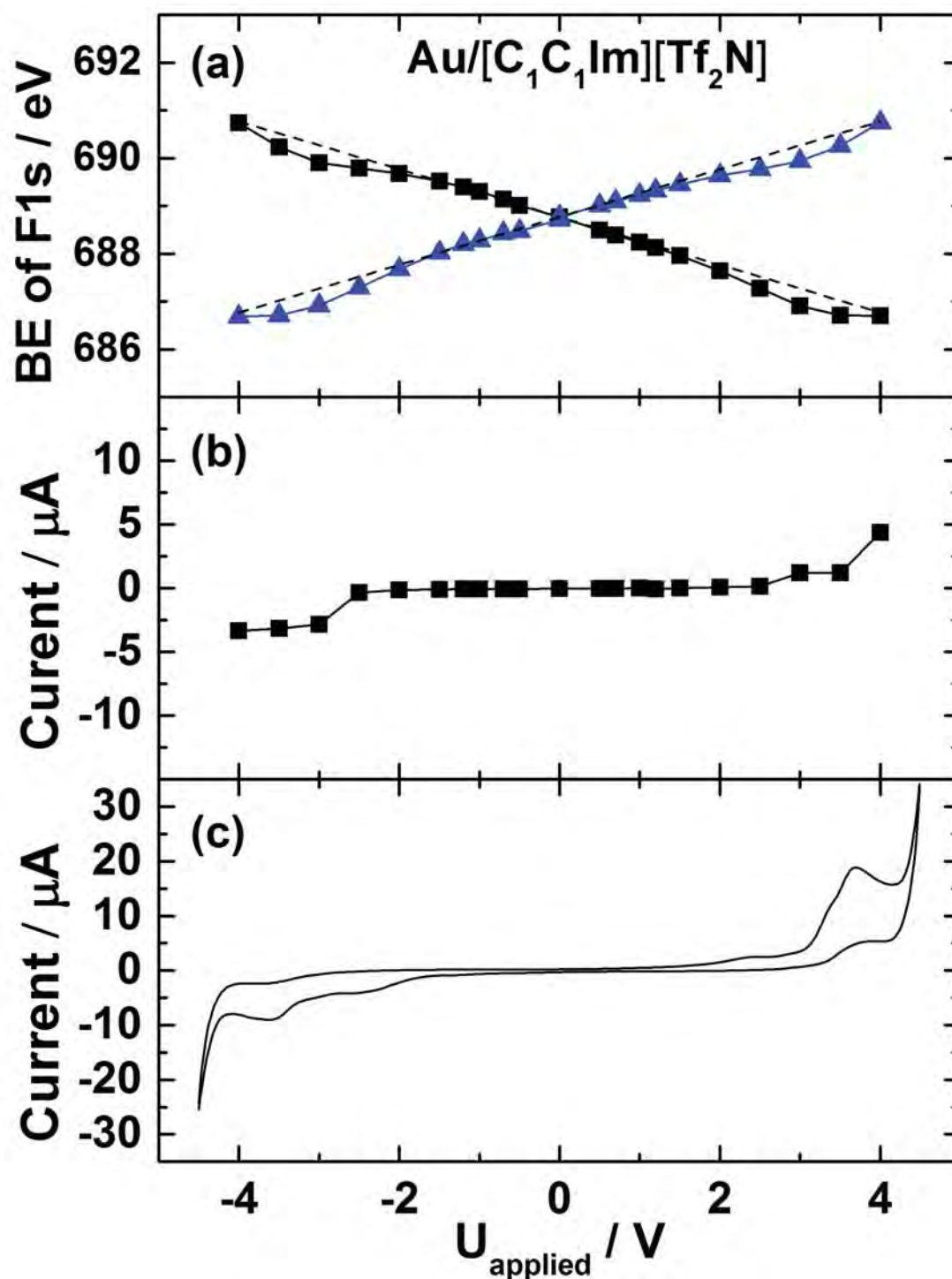
Figure A8 (a) BE of F 1s in $[C_1C_1Im][Tf_2N]$ XP spectra according to $U_{applied}$ in the cases of an Au WE-grounded (d=0.25 mm) (black square) and an Au CE-grounded (d=0.25 mm) (blue triangle) setups. The ideal lines are indicated as dashed lines. (b) Residual current at a constant $U_{applied}$ during the XPS measurement. (c) Potential sweep measurement. The ramping rate is 50 mV/s.
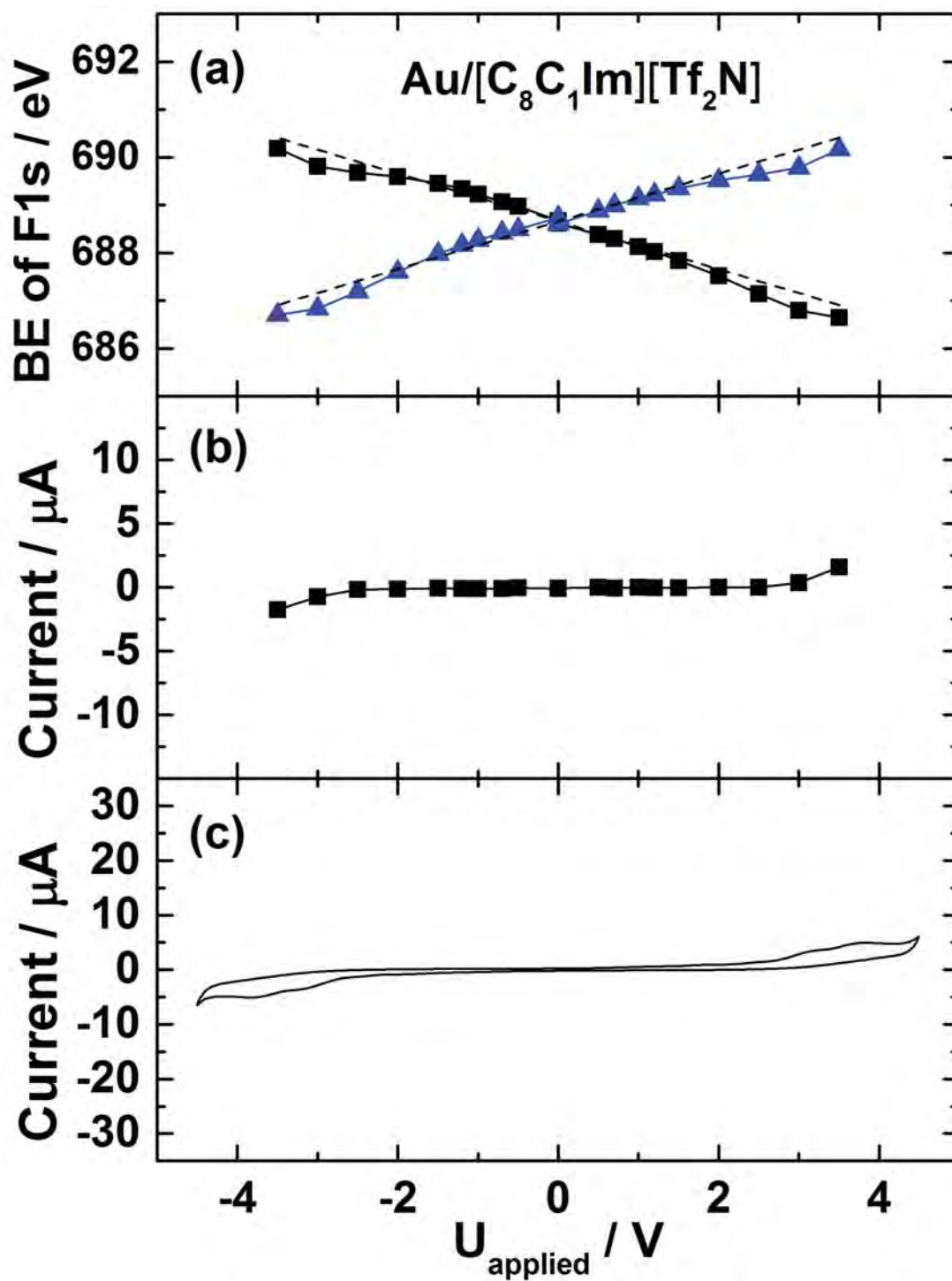
Figure A9 (a) BE of F 1s in [C₈C₁Im][Tf₂N] XP spectra according to $U_{applied}$ in the cases of an Au WE-grounded (d=0.25 mm) (black square) and an Au CE-grounded (d=0.25 mm) (blue triangle) setups. The ideal lines are indicated as dashed lines. (b) Residual current at a constant $U_{applied}$ during the XPS measurement. (c) Potential sweep measurement. The ramping rate is 50 mV/s.
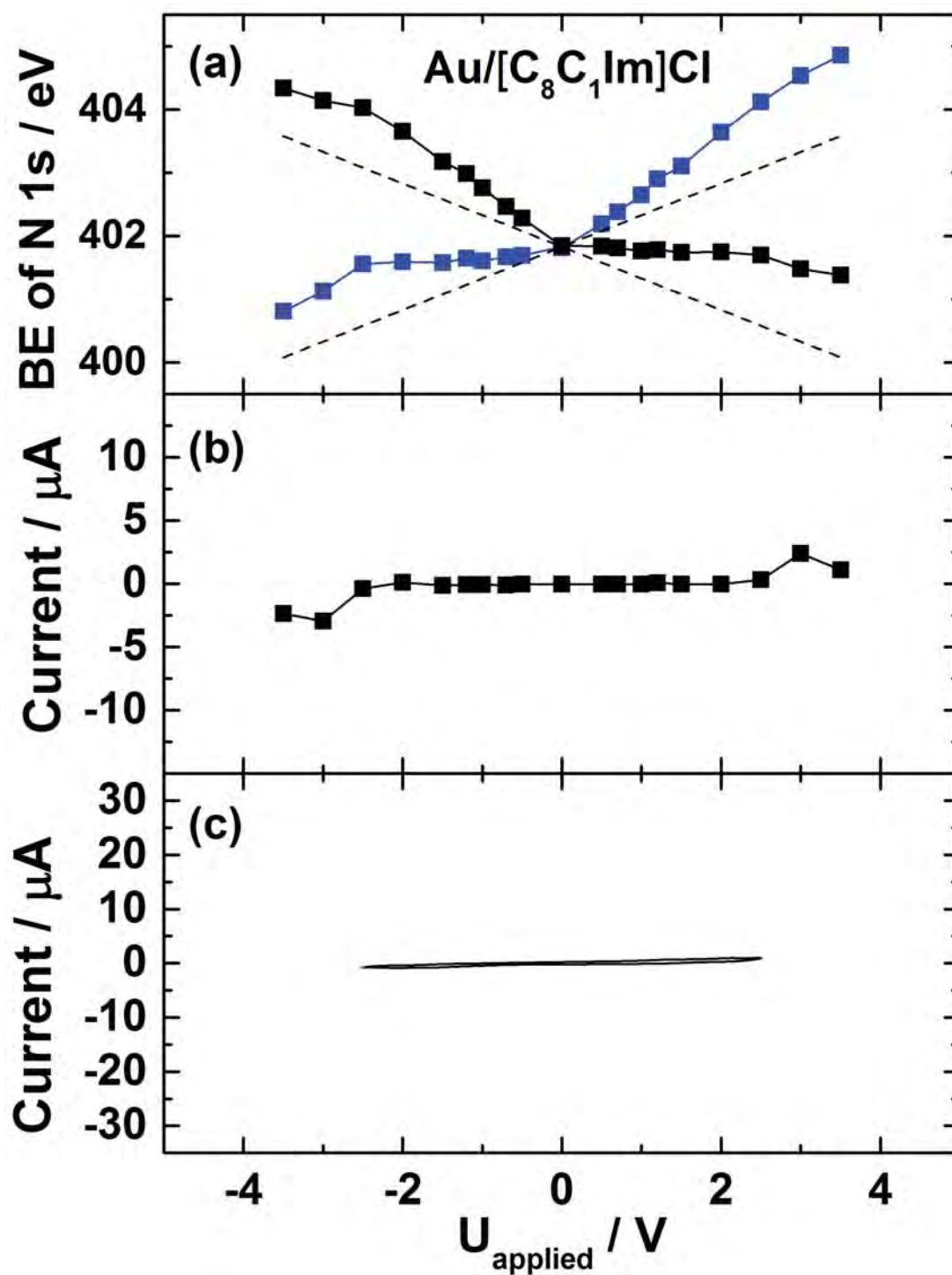
Figure A10 (a) BE of N 1s in [C$_8$C$_1$Im]Cl XP spectra according to U$_{applied}$ in the cases of an Au WE-grounded (d=0.25 mm) (black square) and an Au CE-grounded (d=0.25 mm) (blue triangle) setups. The ideal lines are indicated as dashed lines. (b) Residual current at a constant U$_{applied}$ during the XPS measurement. (c) Potential sweep measurement. The ramping rate is 50 mV/s.
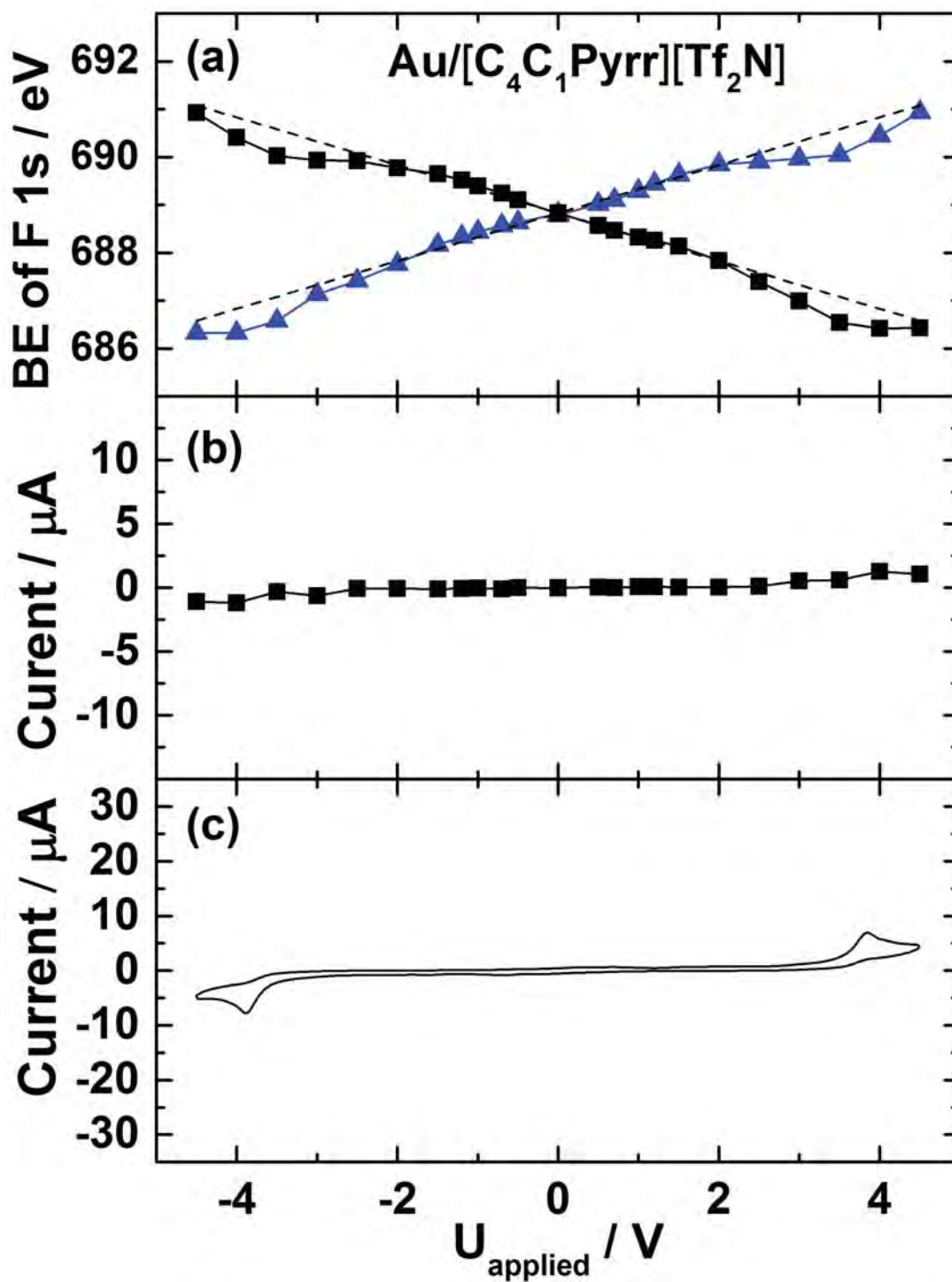
Figure A11 (a) BE of F 1s in [C₄C₁Pyrr][Tf₂N] XP spectra according to $U_{applied}$ in the cases of an Au WE-grounded (d=0.25 mm) (black square) and an Au CE-grounded (d=0.25 mm) (blue triangle) setups. The ideal lines are indicated as dashed lines. (b) Residual current at a constant $U_{applied}$ during the XPS measurement. (c) Potential sweep measurement. The ramping rate is 50 mV/s.

11.2. Appendix to Chapter 4

In the following, we show the experimental data collected during the potential screening measurements. The data were obtained with a symmetric two-electrode electrochemical cell setup comprising two wires of identical metal (ϕ= 0.25 mm for Au, and ϕ=0.30 mm for Pt) as electrodes with identical contact area to the electrolyte. At a specific applied cell voltage, $U_{applied}$, the potential screening at the anode and cathode is determined through the binding energy shift of IL-related core level signals at the IL/vacuum interface by XPS (that is, F 1s for all systems containing more than 10 mol% $[C_8C_1Im][Tf_2N]$, N 1s for the rest).

Measurements were performed for different mixtures of $[C_8C_1Im][Tf_2N]$ and $[C_8C_1Im]Cl$, denoted as $[C_8C_1Im][Tf_2N]_xCl_{1-x}$, with Au and Pt electrodes; see Figures A13-A27. In each case, the binding energy of the F 1s (or N 1s) core level vs applied potential is shown in (a) for applied cell voltages of −2 V to +2 V, with the working electrode (WE) grounded (black squares) and the counter-electrode (CE) grounded (blue triangles). The dashed lines indicate the ideal behavior, that is, equal potential drops at the anode/cathode interfaces (±0.5 eV/V). Also shown is the corresponding residual current during the XPS measurements (b), as measured at constant external voltages applied. The residual currents are estimated by averaging the current of each chronoamperogramm after 60 s at a constant voltage applied. The chronoamperometric measurements of $[C_8C_1Im][Tf_2N]_xCl_{1-x}$ (x = 0.01) with Au electrodes are shown in Figure A12. A rapid decrease of current is observed within 1 s, which originates from the capacitive charging process during the EDL formation. After applying the voltage, we waited for 60 s before starting the XPS measurement. The negligible residual currents of typically well below 0.2 µA confirm the absence of faradaic processes and an equilibrium state during XPS (note that the remaining ±0.4 µA current of the ±2 V curves shown in Figure A12 is due to leakage or parasitic currents in some of our electrochemical cells. Notably, for pure $[C_8C_1Im]Cl$ no such current is present (see Figure A20)).

For each studied mixture, the quantitative analysis of all IL-related core levels is shown in a separate Table (Tables A1-A15). Thereby, the experimental mol% is determined by the weighted amount of the two ILs in the mixtures, and the XPS mol% is obtained by the ratio of the areas of the Cl 2p and F 1s peaks. The nominal and experimental ratios are given in number of atoms of the various elements in the IL mixture.
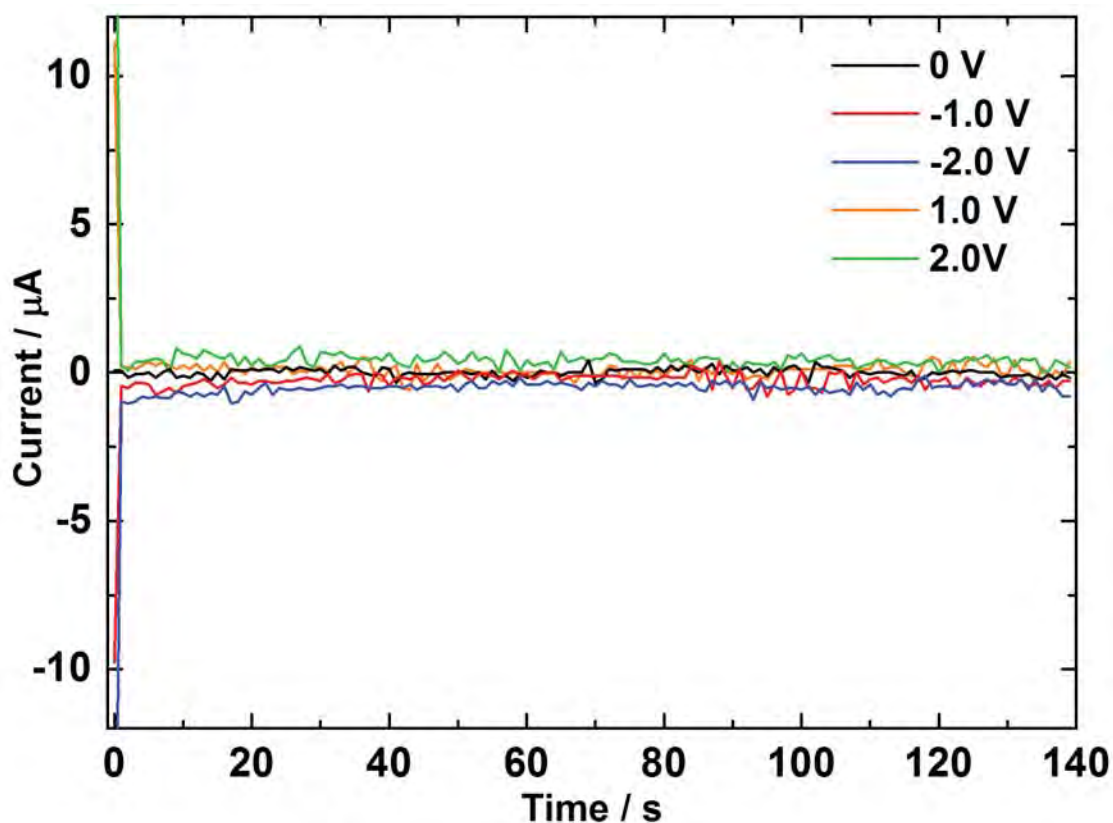
Figure A12. Current between Au electrodes in $[C_8C_1Im][Tf_2N]_xCl_{1-x}$ (x = 0.01) with a constant applied potential. The charging current for an EDL formation decreased rapidly within 1 s. All XPS measurements were started after the EDL formation and the residual current during the measurement was less than 0.2 μA; note that for this specific cell a residual leakage current of ±0.4 μA was present at the highest voltage of ±2V.

$[C_8C_1Im][Tf_2N]_xCl_{1-x}$ (x = 1.0) on Au electrodes
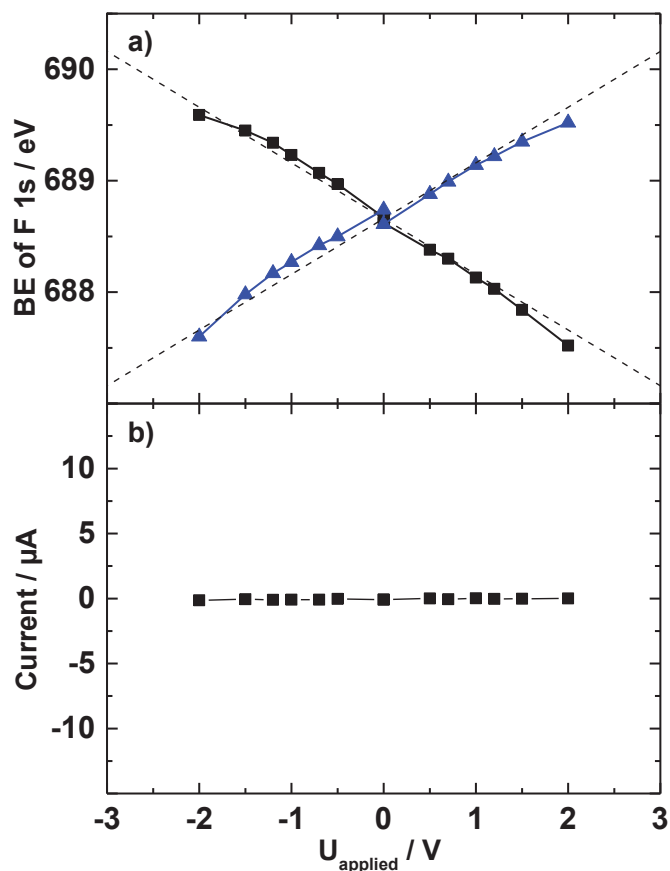
Figure A13 (a) Data for $[C_8C_1Im][Tf_2N]_xCl_{1-x}$ (x = 1) on Au. (b) Residual current during the XPS measurements at constant external voltages applied.

Table A1 Quantitative analysis of the XP spectra of $[C_8C_1Im][Tf_2N]_xCl_{1-x}$ (x = 1) on Au.

	$[C_8C_1Im][Tf_2N]_xCl_{1-x}$ (x = 1.0)									
Ions	$[C_8C_1Im]^+$				$[Tf_2N]^-$					Cl^-
Exp. mol %					100					0
XPS mol %										
XPS regions	N 1s N_{Im}	C 1s C_2	C 1s C_{het}	C 1s C_{alk}	F 1s F_{Tf2N}	O 1s O_{Tf2N}	N 1s N_{Tf2N}	C 1s C_{Tf2N}	S 2p S_{Tf2N}	Cl 2p
Nominal ratio	2.0	1.0	4.0	7.0	6.0	4.0	1.0	2.0	2.0	-/-
Exp. ratio	1.9	1.0	4.0	6.8	6.1	4.0	1.0	2.1	1.9	-/-

[C₈C₁Im][Tf₂N]ₓCl₁₋ₓ (x = 0.999) on Au electrodes

$[C_8C_1Im][Tf_2N]_xCl_{1-x}$ (x = 0.999) on Au electrodes
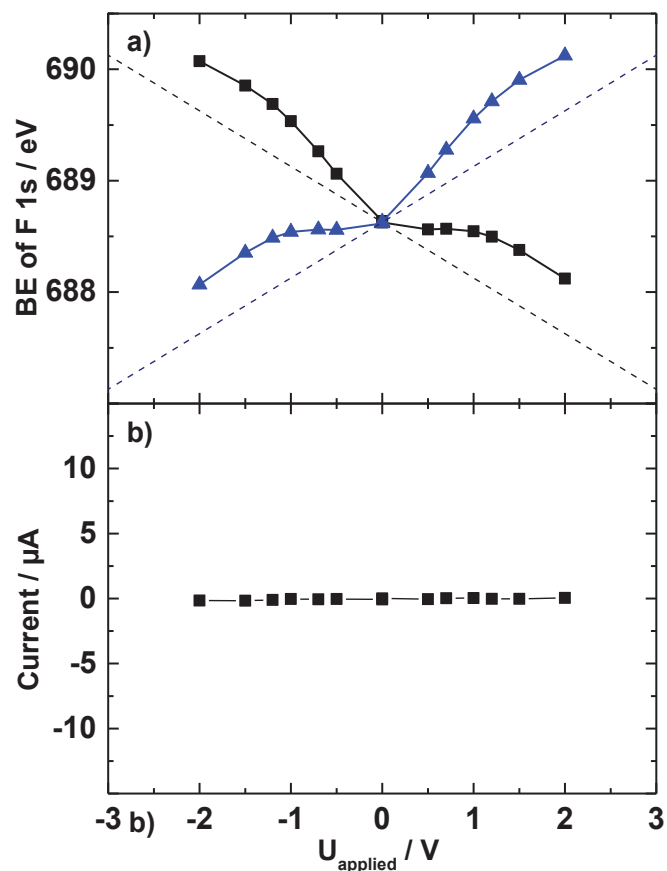
Figure A14 (a) Data for $[C_8C_1Im][Tf_2N]_xCl_{1-x}$ (x = 0.999) on Au. (b) Residual current during the XPS measurements at constant external voltages applied.

Table A2. Quantitative analysis of the XP spectra of $[C_8C_1Im][Tf_2N]_xCl_{1-x}$ (x = 0.999) on Au.

	$[C_8C_1Im][Tf_2N]_xCl_{1-x}$ (x = 0.999)								
Ions	**$[C_8C_1Im]^+$**				**$[Tf_2N]^-$**				**Cl⁻**
Exp. mol %					99.91				0.09
XPS mol %					-/-				-/-
XPS regions	N 1s N_{Im}	C 1s C_2	C 1s C_{het}	C 1s C_{alk}	F 1s F_{Tf2N}	O 1s O_{Tf2N}	N 1s N_{Tf2N}	C 1s C_{Tf2N}	S 2p S_{Tf2N}	Cl 2p
Nominal ratio	2.0	1.0	4.0	7.0	6.0	4.0	1.0	2.0	2.0	0.001
Exp. ratio	2.0	1.0	4.0	6.8	6.1	4.1	1.0	1.9	2.0	-/-

$[C_8C_1Im][Tf_2N]_xCl_{1-x}$ (x = 0.99) on Au electrodes
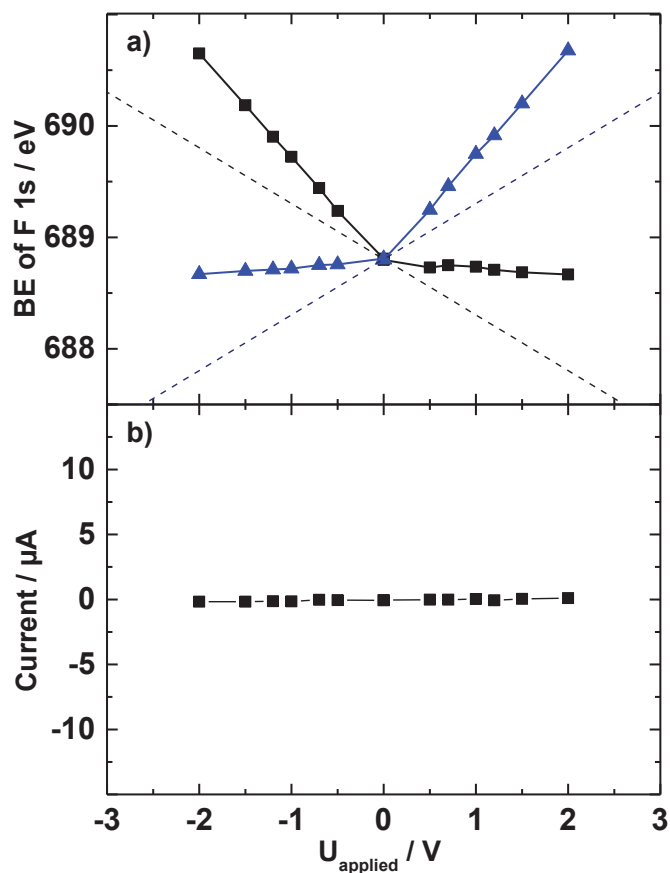
Figure A15 (a) Data for $[C_8C_1Im][Tf_2N]_xCl_{1-x}$ (x = 0.99) on Au. (b) Residual current during the XPS measurements at constant external voltages applied.

Table A3. Quantitative analysis of the XP spectra of $[C_8C_1Im][Tf_2N]_xCl_{1-x}$ (x = 0.99) on Au.

	$[C_8C_1Im][Tf_2N]_xCl_{1-x}$ (x = 0.99)								
Ions	$[C_8C_1Im]^+$				$[Tf_2N]^-$				Cl^-
Exp. mol %					99.0				1.0
XPS mol %					-/-				-/-
XPS regions	N 1s N_{Im}	C 1s C_2	C 1s C_{het}	C 1s C_{alk}	F 1s F_{Tf2N}	O 1s O_{Tf2N}	N 1s N_{Tf2N}	C 1s C_{Tf2N}	S 2p S_{Tf2N}	Cl 2p
Nominal ratio	2.0	1.0	4.0	7.0	6.0	4.0	1.0	2.0	2.0	0.01
Exp. ratio	2.0	1.0	4.0	6.9	6.1	4.1	1.0	2.0	2.0	-/-

[C$_8$C$_1$Im][Tf$_2$N]$_x$Cl$_{1-x}$ (x = 0.9) on Au electrodes
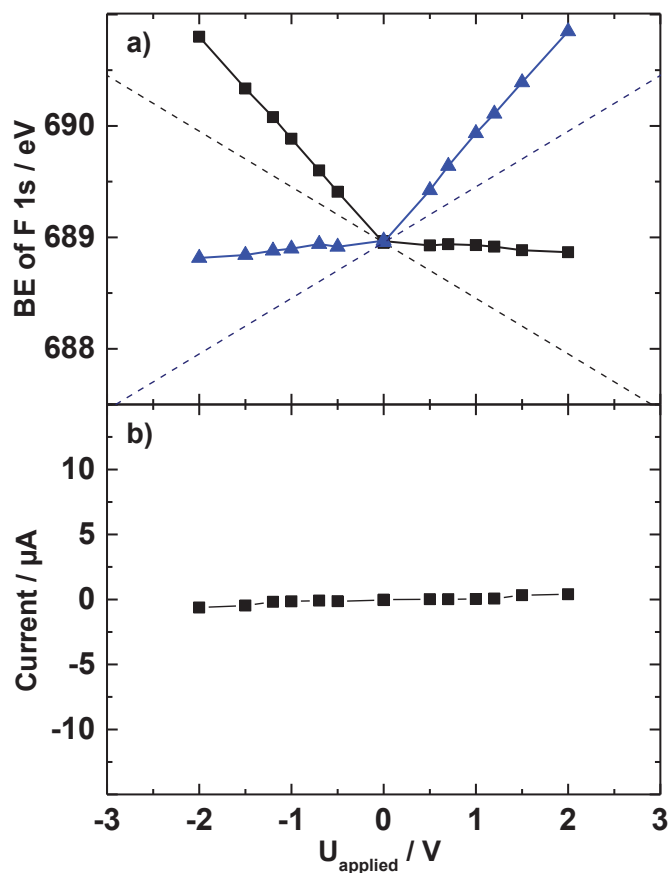
Figure A16 (a) Data for [C$_8$C$_1$Im][Tf$_2$N]$_x$Cl$_{1-x}$ (x = 0.9) on Au. (b) Residual current during the XPS measurements at constant external voltages applied.

Table A4. Quantitative analysis of the XP spectra of [C$_8$C$_1$Im][Tf$_2$N]$_x$Cl$_{1-x}$ (x = 0.9) on Au.

	[C$_8$C$_1$Im][Tf$_2$N]$_x$Cl$_{1-x}$ (x = 0.9)									
Ions	[C$_8$C$_1$Im]$^+$				[Tf$_2$N]$^-$					Cl$^-$
Exp. mol %					90.1					9.9
XPS mol %					90.3					9.7
XPS regions	N 1s N_{Im}	C 1s C_2	C 1s C_{het}	C 1s C_{alk}	F 1s F_{Tf2N}	O 1s O_{Tf2N}	N 1s N_{Tf2N}	C 1s C_{Tf2N}	S 2p S_{Tf2N}	Cl 2p
Nominal ratio	2.0	1.0	4.0	7.0	5.4	3.6	0.9	1.8	1.8	0.1
Exp. ratio	2.0	1.0	4.0	6.9	5.3	3.8	1.0	1.8	1.8	0.1

[C$_8$C$_1$Im][Tf$_2$N]$_x$Cl$_{1-x}$ (x = 0.5) on Au electrodes
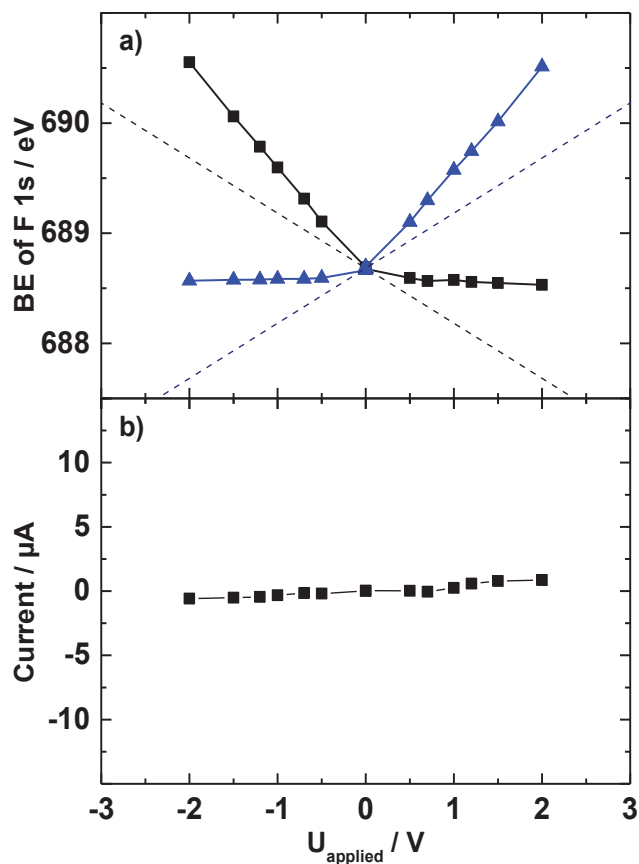
Figure A17 (a) Data for [C$_8$C$_1$Im][Tf$_2$N]$_x$Cl$_{1-x}$ (x = 0.5) on Au. (b) Residual current during the XPS measurements at constant external voltages applied.

Table A5. Quantitative analysis of the XP spectra of [C$_8$C$_1$Im][Tf$_2$N]$_x$Cl$_{1-x}$ (x = 0.5) on Au.

	[C$_8$C$_1$Im][Tf$_2$N]$_x$Cl$_{1-x}$ (x = 0.5)								
Ions	[C$_8$C$_1$Im]$^+$				[Tf$_2$N]$^-$					Cl$^-$
Exp. mol %					49.2					50.8
XPS mol %					51.4					48.6
XPS regions	N 1s N$_{Im}$	C 1s C$_2$	C 1s C$_{het}$	C 1s C$_{alk}$	F 1s F$_{Tf2N}$	O 1s O$_{Tf2N}$	N 1s N$_{Tf2N}$	C 1s C$_{Tf2N}$	S 2p S$_{Tf2N}$	Cl 2p
Nominal ratio	2.0	1.0	4.0	7.0	3.0	2.0	0.5	1.0	1.0	0.5
Exp. ratio	2.0	1.0	3.9	7.1	2.9	2.3	0.6	1.1	1.0	0.5

[C$_8$C$_1$Im][Tf$_2$N]$_x$Cl$_{1-x}$ (x = 0.1) on Au electrodes
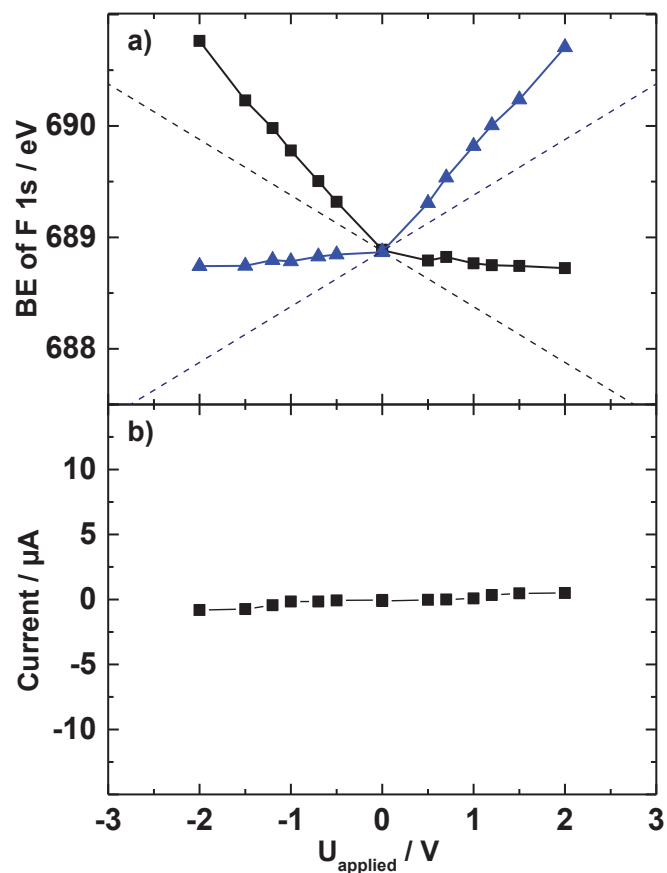
Figure A18 (a) Data for [C$_8$C$_1$Im][Tf$_2$N]$_x$Cl$_{1-x}$ (x = 0.1) on Au. (b) Residual current during the XPS measurements at constant external voltages applied.

Table A6. Quantitative analysis of the XP spectra of [C$_8$C$_1$Im][Tf$_2$N]$_x$Cl$_{1-x}$ (x = 0.1) on Au.

Ions	[C$_8$C$_1$Im]$^+$				[Tf$_2$N]$^-$					Cl$^-$
Exp. mol %					11.0					89
XPS mol %					14.7					85.3
XPS regions	N 1s N$_{Im}$	C 1s C$_2$	C 1s C$_{het}$	C 1s C$_{alk}$	F 1s F$_{Tf2N}$	O 1s O$_{Tf2N}$	N 1s N$_{Tf2N}$	C 1s C$_{Tf2N}$	S 2p S$_{Tf2N}$	Cl 2p
Nominal ratio	2.0	1.0	4.0	7.0	0.6	0.4	0.1	0.2	0.2	0.9
Exp. ratio	1.8	0.9	3.6	6.8	0.8	1.0	0.2	0.3	0.3	0.8

A-18

$[C_8C_1Im][Tf_2N]_xCl_{1-x}$ (x = 0.01) on Au electrodes
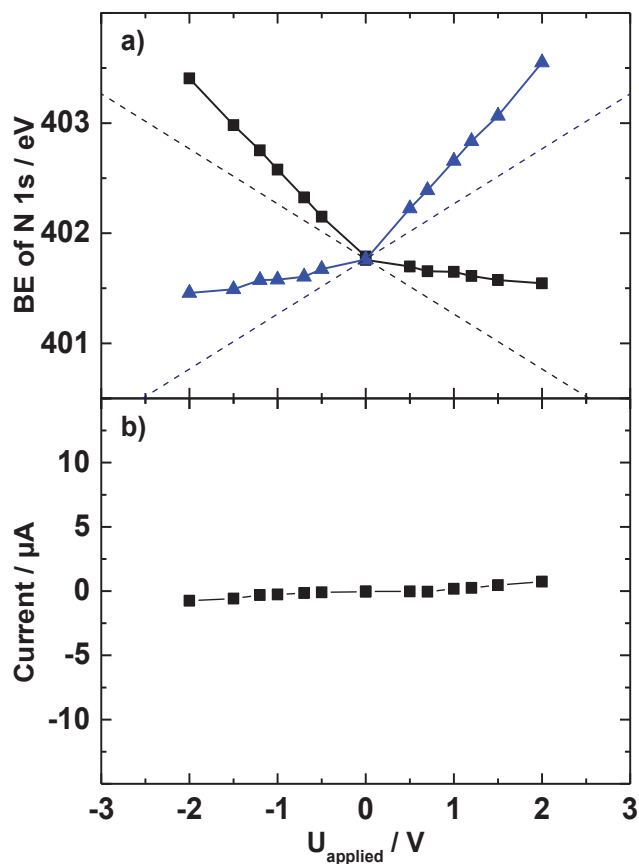
Figure A19 (a) Data for $[C_8C_1Im][Tf_2N]_xCl_{1-x}$ (x = 0.01) on Au. (b) Residual current during the XPS measurements at constant external voltages applied.

Table A7. Quantitative analysis of the XP spectra of $[C_8C_1Im][Tf_2N]_xCl_{1-x}$ (x = 0.01) on Au.

	$[C_8C_1Im][Tf_2N]_xCl_{1-x}$ (x = 0.01)								
Ions	$[C_8C_1Im]^+$				$[Tf_2N]^-$				Cl^-
Exp. mol %					1.3				98.7.
XPS mol %					3.3				96.7
XPS regions	N 1s N_{Im}	C 1s C_2	C 1s C_{het}	C 1s C_{alk}	F 1s F_{Tf2N}	O 1s O_{Tf2N}	N 1s N_{Tf2N}	C 1s C_{Tf2N}	S 2p S_{Tf2N}	Cl 2p
Nominal ratio	2.0	1.0	4.0	7.0	0.06	0.04	-/-	-/-	0.02	0.99
Exp. ratio	2.0	1.0	3.9	7.0	0.19	0.16	-/-	-/-	0.05	0.95

$[C_8C_1Im][Tf_2N]_xCl_{1-x}$ (x = 0) on Au electrodes
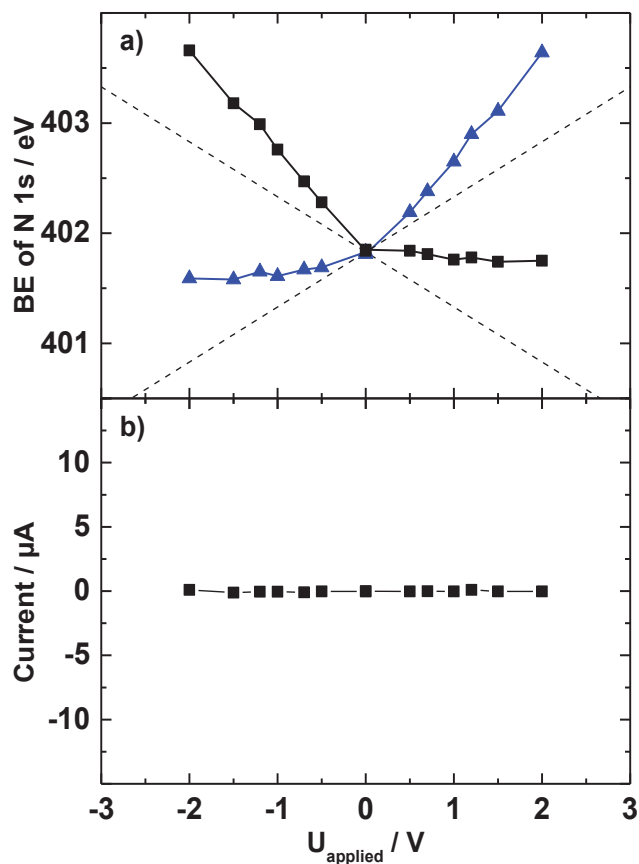
Figure A20 (a) Data for $[C_8C_1Im][Tf_2N]_xCl_{1-x}$ (x = 0) on Au. (b) Residual current during the XPS measurements at constant external voltages applied.

Table A8. Quantitative analysis of the XP spectra of $[C_8C_1Im][Tf_2N]_xCl_{1-x}$ (x = 0) on Au.

	$[C_8C_1Im][Tf_2N]_xCl_{1-x}$ (x = 0)									
Ions	$[C_8C_1Im]^+$				$[Tf_2N]^-$					Cl^-
Exp. mol %					0					100
XPS mol %										
XPS regions	N 1s N_{Im}	C 1s C_2	C 1s C_{het}	C 1s C_{alk}	F 1s F_{Tf2N}	O 1s O_{Tf2N}	N 1s N_{Tf2N}	C 1s C_{Tf2N}	S 2p S_{Tf2N}	Cl 2p
Nominal ratio	2.0	1.0	4.0	7.0	-/-	-/-	-/-	-/-	-/-	1.0
Exp. ratio	1.9	1.0	4.0	7.1	-/-	-/-	-/-	-/-	-/-	1.0

$[C_8C_1Im][Tf_2N]_xCl_{1-x}$ (x = 1.0) on Pt electrodes
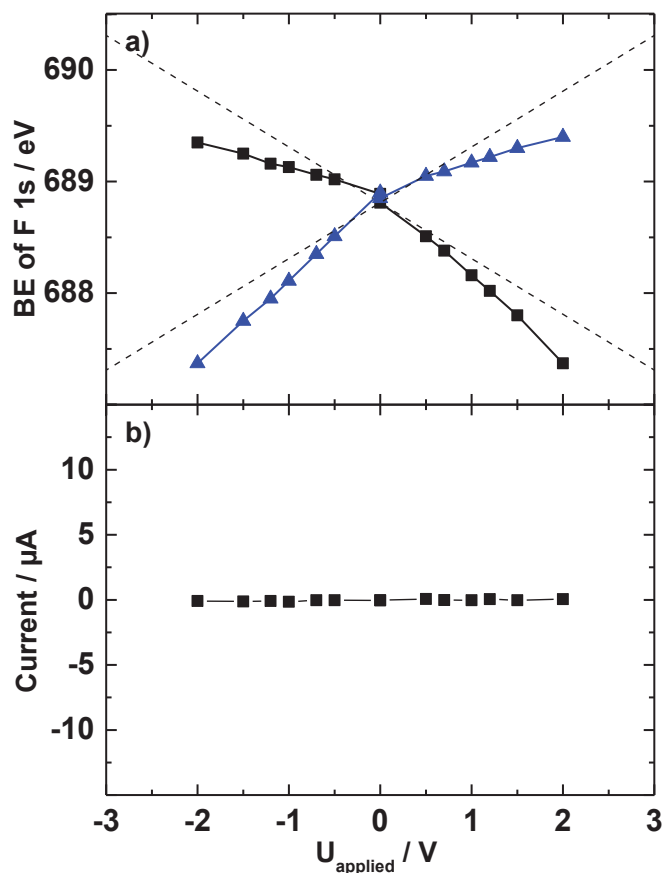
Figure A21 (a) Data for $[C_8C_1Im][Tf_2N]_xCl_{1-x}$ (x = 1.0) on Pt. (b) Residual current during the XPS measurements at constant external voltages applied.

Table A9. Quantitative analysis of the XP spectra of $[C_8C_1Im][Tf_2N]_xCl_{1-x}$ (x = 1.0) on Pt.

	$[C_8C_1Im][Tf_2N]_xCl_{1-x}$ (x = 1.0)									
Ions	$[C_8C_1Im]^+$				$[Tf_2N]^-$					Cl^-
Exp. mol %					100					0
XPS mol %										
XPS regions	N 1s N_{Im}	C 1s C_2	C 1s C_{het}	C 1s C_{alk}	F 1s F_{Tf2N}	O 1s O_{Tf2N}	N 1s N_{Tf2N}	C 1s C_{Tf2N}	S 2p S_{Tf2N}	Cl 2p
Nominal ratio	2.0	1.0	4.0	7.0	6.0	4.0	1.0	2.0	2.0	-/-
Exp. ratio	1.0	1.0	4.0	6.8	6.1	4.1	1.0	2.0	2.1	-/-

[C$_8$C$_1$Im][Tf$_2$N]$_x$Cl$_{1-x}$ (x = 0.99) on Pt electrodes
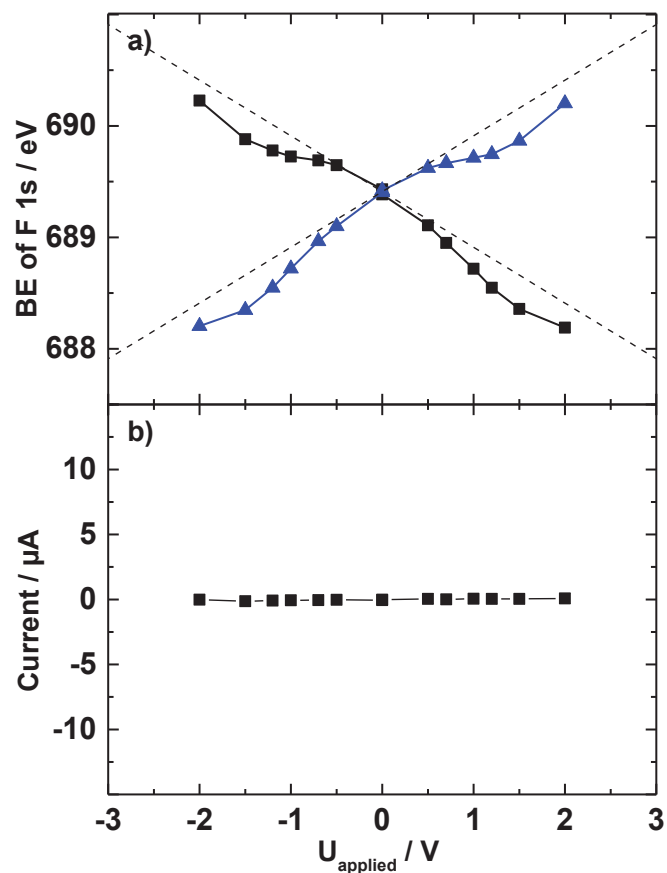
Figure A22 (a) Data for [C$_8$C$_1$Im][Tf$_2$N]$_x$Cl$_{1-x}$ (x = 0.99) on Pt. (b) Residual current during the XPS measurements at constant external voltages applied.

Table A10. Quantitative analysis of the XP spectra of [C$_8$C$_1$Im][Tf$_2$N]$_x$Cl$_{1-x}$ (x = 0.99) on Pt.

	[C$_8$C$_1$Im][Tf$_2$N]$_x$Cl$_{1-x}$ (x = 0.99)									
Ions	[C$_8$C$_1$Im]$^+$				[Tf$_2$N]$^-$					Cl$^-$
Exp. mol %					99.0					1.0
XPS mol %					-/-					-/-
XPS regions	N 1s N$_{Im}$	C 1s C$_2$	C 1s C$_{het}$	C 1s C$_{alk}$	F 1s F$_{Tf2N}$	O 1s O$_{Tf2N}$	N 1s N$_{Tf2N}$	C 1s C$_{Tf2N}$	S 2p S$_{Tf2N}$	Cl 2p
Nominal ratio	2.0	1.0	4.0	7.0	6.0	4.0	1.0	2.0	2.0	0.01
Exp. ratio	2.0	1.0	4.0	6.9	6.1	4.1	1.0	2.0	2.0	-/-

[C$_8$C$_1$Im][Tf$_2$N]$_x$Cl$_{1-x}$ (x = 0.9) on Pt electrodes
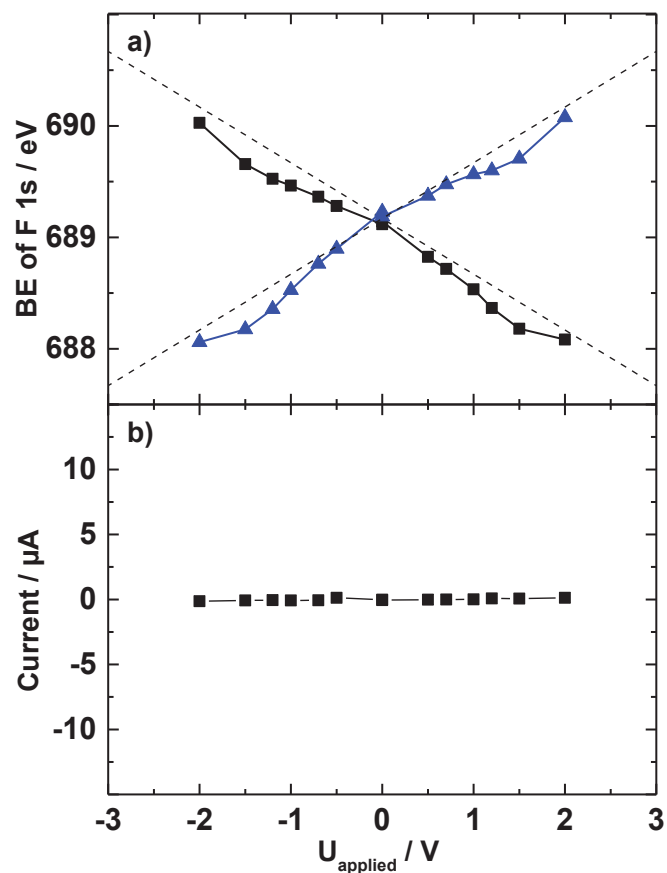
Figure A23 (a) Data for [C$_8$C$_1$Im][Tf$_2$N]$_x$Cl$_{1-x}$ (x = 0.9) on Pt. (b) Residual current during the XPS measurements at constant external voltages applied.

Table A11. Quantitative analysis of the XP spectra of [C$_8$C$_1$Im][Tf$_2$N]$_x$Cl$_{1-x}$ (x = 0.9) on Pt.

	[C$_8$C$_1$Im][Tf$_2$N]$_x$Cl$_{1-x}$ (x = 0.9)								
Ions	[C$_8$C$_1$Im]$^+$				[Tf$_2$N]$^-$				Cl$^-$
Exp. mol %					90.1				9.9
XPS mol %					88.0				12.0
XPS regions	N 1s N_{Im}	C 1s C_2	C 1s C_{het}	C 1s C_{alk}	F 1s F_{Tf2N}	O 1s O_{Tf2N}	N 1s N_{Tf2N}	C 1s C_{Tf2N}	S 2p S_{Tf2N}	Cl 2p
Nominal ratio	2.0	1.0	4.0	7.0	5.4	3.6	0.9	1.8	1.8	0.1
Exp. ratio	1.9	1.0	4.1	6.9	5.1	4.0	0.9	1.7	1.8	0.1

[C$_8$C$_1$Im][Tf$_2$N]$_x$Cl$_{1-x}$ (x = 0.5) on Pt electrodes
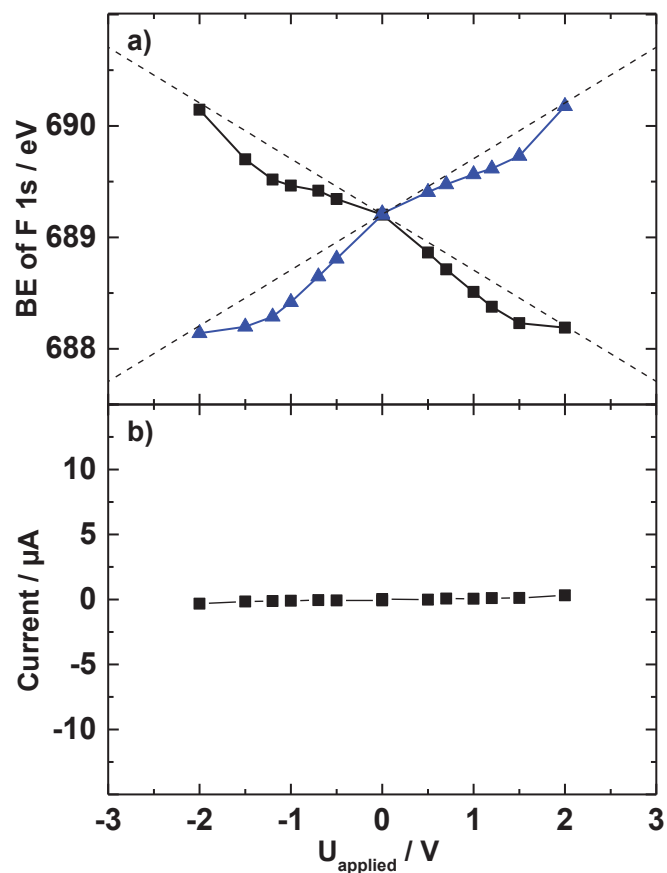
Figure A24 (a) Data for [C$_8$C$_1$Im][Tf$_2$N]$_x$Cl$_{1-x}$ (x = 0.5) on Pt. (b) Residual current during the XPS measurements at constant external voltages applied.

Table A12. Quantitative analysis of the XP spectra of [C$_8$C$_1$Im][Tf$_2$N]$_x$Cl$_{1-x}$ (x = 0.5) on Pt.

	[C$_8$C$_1$Im][Tf$_2$N]$_x$Cl$_{1-x}$ (x = 0.5)									
Ions	[C$_8$C$_1$Im]$^+$				[Tf$_2$N]$^-$					Cl$^-$
Exp. mol %					50.0					50.0
XPS mol %					44.1					55.9
XPS regions	N 1s N_{Im}	C 1s C_2	C 1s C_{het}	C 1s C_{alk}	F 1s F_{Tf2N}	O 1s O_{Tf2N}	N 1s N_{Tf2N}	C 1s C_{Tf2N}	S 2p S_{Tf2N}	Cl 2p
Nominal ratio	2.0	1.0	4.0	7.0	3.0	2.0	0.5	1.0	1.0	0.5
Exp. ratio	2.0	1.0	4.1	7.1	2.3	2.9	0.5	0.9	0.9	0.5

A-24

$[C_8C_1Im][Tf_2N]_xCl_{1-x}$ (x = 0.1) on Pt electrodes
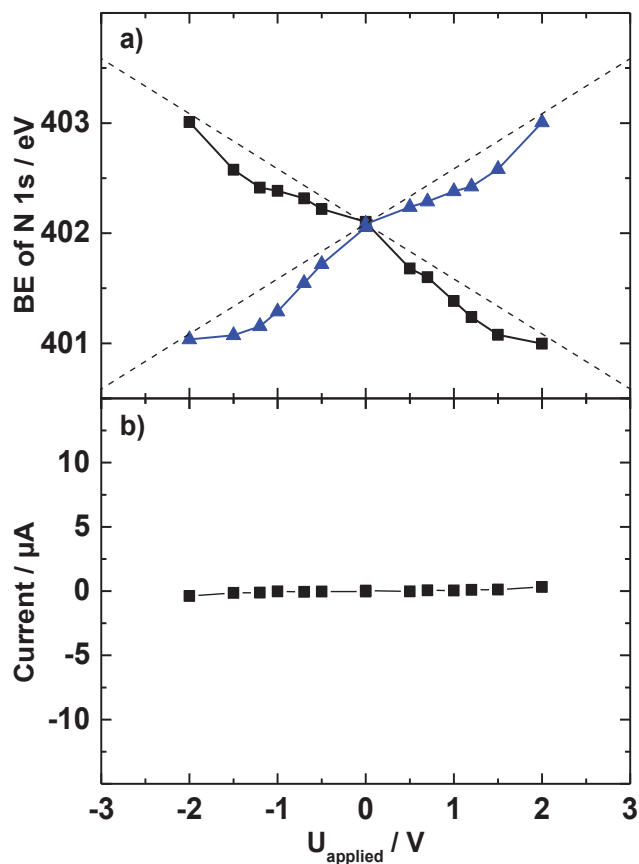
Figure A25 (a) Data for $[C_8C_1Im][Tf_2N]_xCl_{1-x}$ (x = 0.1) on Pt. (b) Residual current during the XPS measurements at constant external voltages applied.

Table A13. Quantitative analysis of the XP spectra of $[C_8C_1Im][Tf_2N]_xCl_{1-x}$ (x = 0.1) on Pt.

	$[C_8C_1Im][Tf_2N]_xCl_{1-x}$ (x = 0.1)								
Ions	$[C_8C_1Im]^+$				$[Tf_2N]^-$					Cl^-
Exp. mol %					11.0					89.0
XPS mol %					10.2					89.8
XPS regions	N 1s N_{Im}	C 1s C_2	C 1s C_{het}	C 1s C_{alk}	F 1s F_{Tf2N}	O 1s O_{Tf2N}	N 1s N_{Tf2N}	C 1s C_{Tf2N}	S 2p S_{Tf2N}	Cl 2p
Nominal ratio	2.0	1.0	4.0	7.0	0.6	0.4	0.1	0.2	0.2	0.9
Exp. ratio	1.9	1.0	4.0	6.9	0.6	0.5	0.1	0.4	0.2	0.9

[C$_8$C$_1$Im][Tf$_2$N]$_x$Cl$_{1-x}$ (x = 0.01) on Pt electrodes
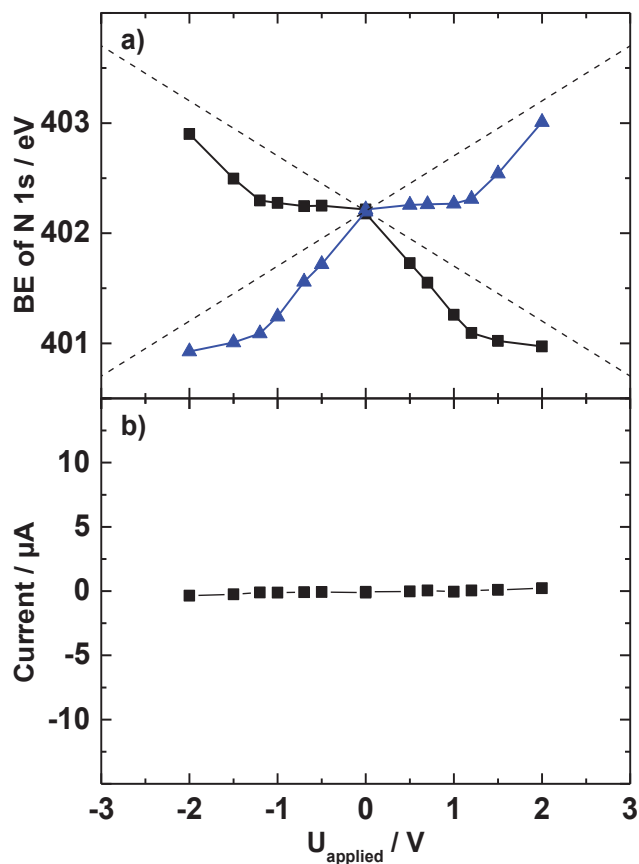
Figure A26 (a) Data for [C$_8$C$_1$Im][Tf$_2$N]$_x$Cl$_{1-x}$ (x = 0.01) on Pt. (b) Residual current during the XPS measurements at constant external voltages applied.

Table A14. Quantitative analysis of the XP spectra of [C$_8$C$_1$Im][Tf$_2$N]$_x$Cl$_{1-x}$ (x = 0.01) on Pt.

	[C$_8$C$_1$Im][Tf$_2$N]$_x$Cl$_{1-x}$ (x = 0.01)									
Ions	[C$_8$C$_1$Im]$^+$				[Tf$_2$N]$^-$					Cl$^-$
Exp. mol %					1.3					98.7
XPS mol %					2.5					97.5
XPS regions	N 1s N_{Im}	C 1s C_2	C 1s C_{het}	C 1s C_{alk}	F 1s F_{Tf2N}	O 1s O_{Tf2N}	N 1s N_{Tf2N}	C 1s C_{Tf2N}	S 2p S_{Tf2N}	Cl 2p
Nominal ratio	2.0	1.0	4.0	7.0	0.06	0.04	-/-	-/-	0.02	0.99
Exp. ratio	2.0	1.0	4.0	6.9	0.15	0.11	-/-	-/-	0.05	0.96

[C$_8$C$_1$Im][Tf$_2$N]$_x$Cl$_{1-x}$ (x = 0), on Pt electrodes
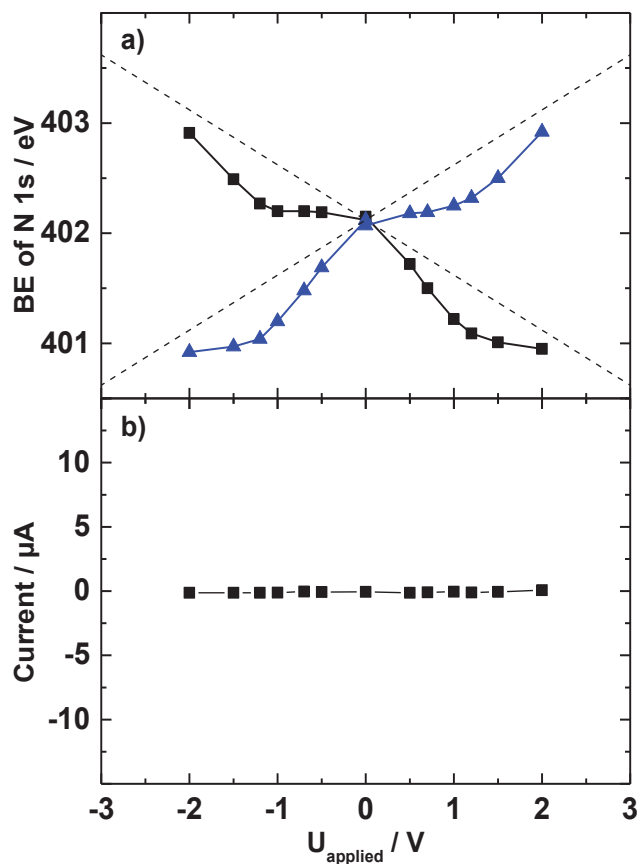
Figure A27 (a) Data for [C$_8$C$_1$Im][Tf$_2$N]$_x$Cl$_{1-x}$ (x = 0) on Pt. (b) Residual current during the XPS measurements at constant external voltages applied.

Table A15. Quantitative analysis of the XP spectra of [C$_8$C$_1$Im][Tf$_2$N]$_x$Cl$_{1-x}$ (x = 0) on Pt.

	[C$_8$C$_1$Im][Tf$_2$N]$_x$Cl$_{1-x}$ (x = 0)									
Ions	[C$_8$C$_1$Im]$^+$				[Tf$_2$N]$^-$					Cl$^-$
Exp. mol %							0			100
XPS mol %										
XPS regions	N 1s N_{Im}	C 1s C_2	C 1s C_{het}	C 1s C_{alk}	F 1s F_{Tf2N}	O 1s O_{Tf2N}	N 1s N_{Tf2N}	C 1s C_{Tf2N}	S 2p S_{Tf2N}	Cl 2p
Nominal ratio	2.0	1.0	4.0	7.0	-/-	-/-	-/-	-/-	-/-	1.0
Exp. ratio	2.0	1.0	4.0	7.0	-/-	-/-	-/-	-/-	-/-	1.0

11.3. Appendix to Chapter 5

11.3.1. Set up

The potential screening measurements in N_2 atmosphere and air were performed with the set-up shown in Figure A28. A constant voltage $U_{applied}$ was applied to two identical electrodes (Pt or Au, same length and diameter), which were connected to the counter electrode (CE) and working electrode (WE) plugs of the potentiostat. A high resistance multimeter (V; ~10 GΩ) was used to measure the voltage V_{ref} between a 3rd reference electrode (Pt) and the CE (or WE).
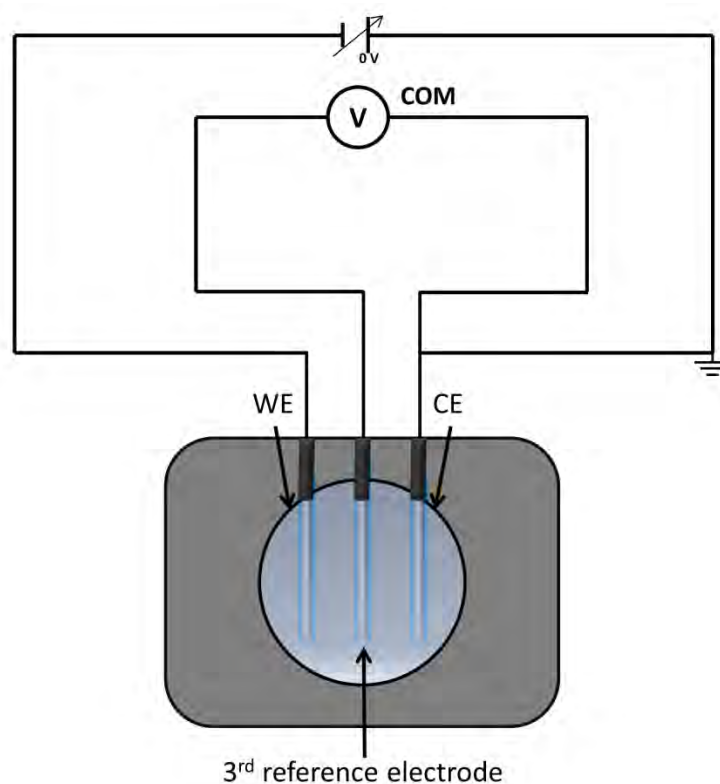
Figure A28 Sketch of the electrochemical cell used for the potential screening measurements in N_2 and air.

11.3.2. Time-Dependent PS Measurements

Figure A29 shows the air-tight box used to perform the measurements in N_2 atmosphere and air. The inlet and outlet pipes (1 and 2) allow for a constant flow of high purity N_2 during the measurements performed in N_2 atmosphere. The sample stage (3) is equipped with three spring contacts with which the electrodes are connected to the potentiostat and the multimeter through a feedthrough (4).

A constant N_2 flow was kept for 10 minutes before starting the measurements in N_2 atmosphere. The voltage steps (grey trace in Figures A30 to A33) had a duration of 139 s each and upon completion, a voltage of 0 V was applied for 10 minutes before starting with the next voltage steps. To perform the measurements in air, the air-tight box was opened and exposed to atmospheric air before applying the voltage steps. In all measuring environments (N_2 and air, and also for XPS in UHV), the voltage steps were always applied following the same order: 1) WE grounded (or COM) positive steps; WE grounded (or COM) negative steps; CE grounded (or COM) positive steps; CE grounded (or COM) negative steps. All the ΔV_{ref} curves in Figures A30 to A33 show fast changes after the voltage step, which then flatten over time at constant values. Therefore, all the cathodic voltage values reported in the main manuscript are taken after ~130 s to ensure that equilibrium at the interface is reached.
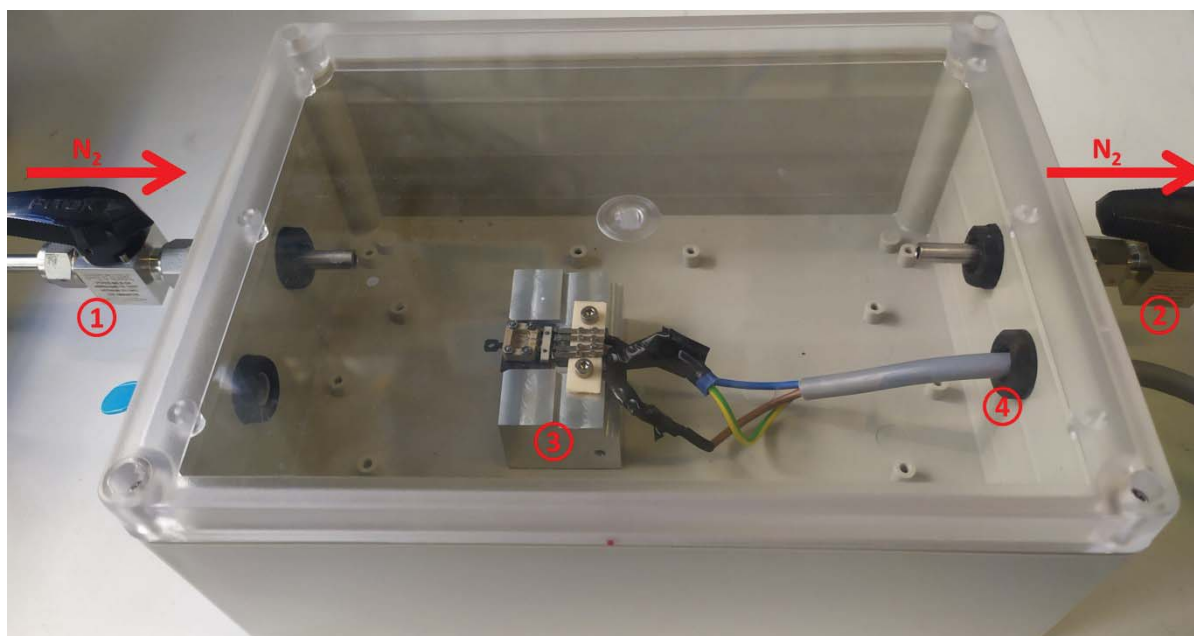
Figure A29 Air-tight box used to perform the measurements in N2 atmosphere and air (numbers, see text).

[C₈C₁Im]Cl with 2 Au electrodes
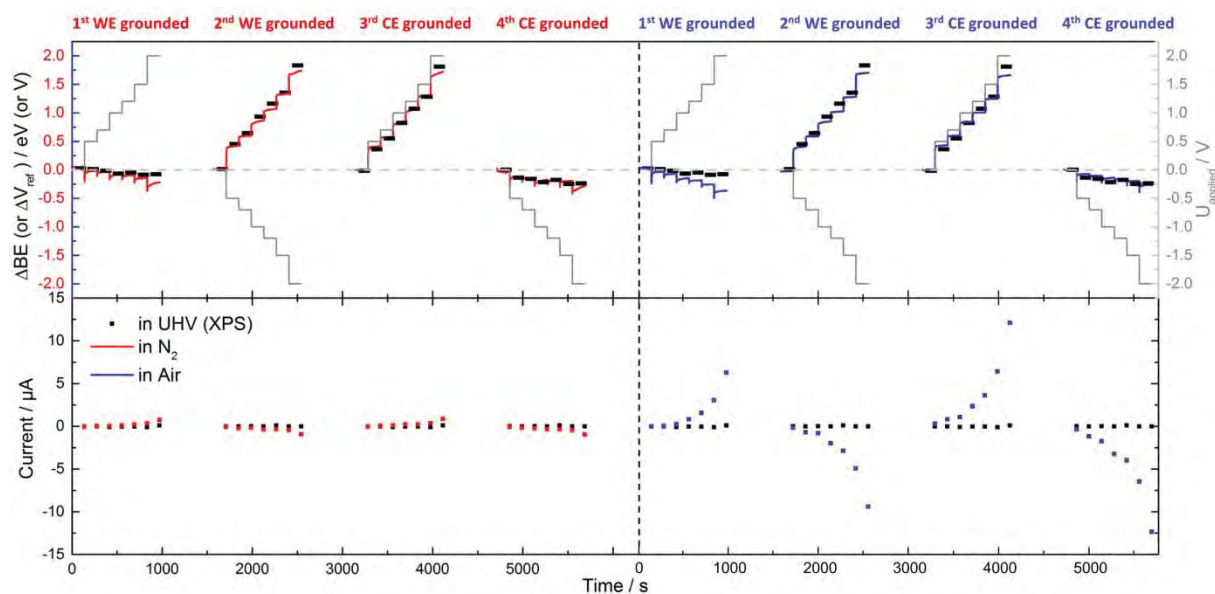
Figure A30 Top: Time-dependent measurement of PS curves of [C₈C₁Im]Cl with Au electrodes recorded in UHV by XPS (black), N₂ atmosphere (red) and air (blue). The applied voltage profiles are shown as grey traces. Bottom: Averaged current recorded during the measurements for [C₈C₁Im]Cl with Au electrodes.

[C₈C₁Im]Cl with 2 Pt electrodes
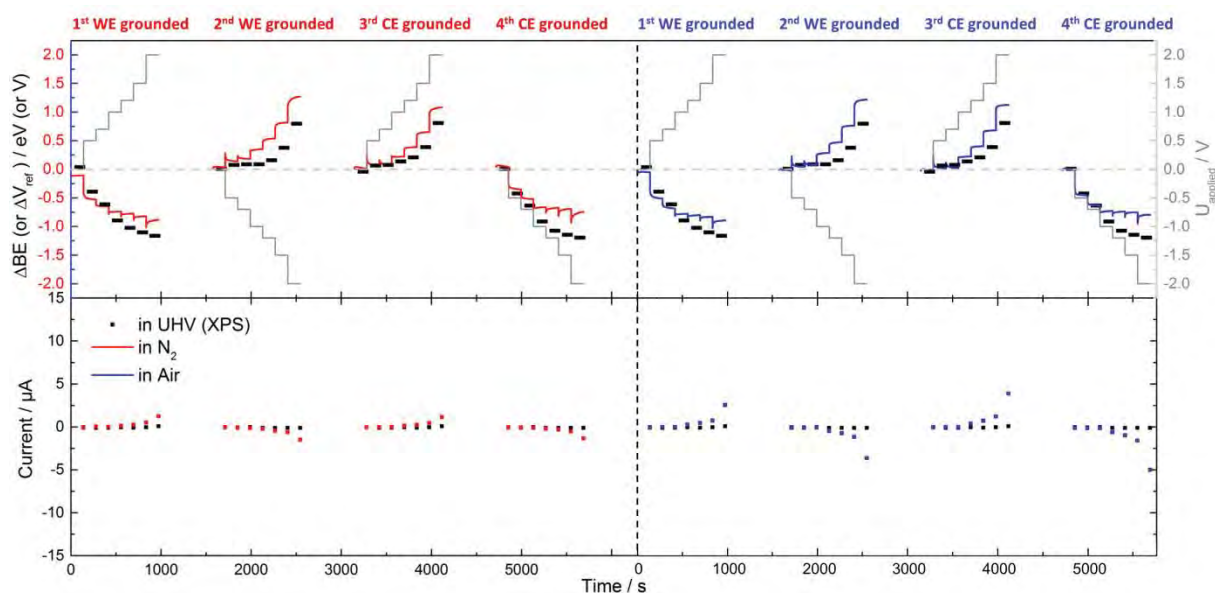
Figure A31 Top: Time-dependent measurement of PS curves of [C₈C₁Im]Cl with Pt electrodes recorded in UHV by XPS (black), N₂ atmosphere (red) and air (blue). The applied voltage profiles are shown as grey traces. Bottom: Averaged current recorded during the measurements for [C₈C₁Im]Cl with Pt electrodes.

A-30

[C$_8$C$_1$Im][Tf$_2$N] with 2 Au electrodes
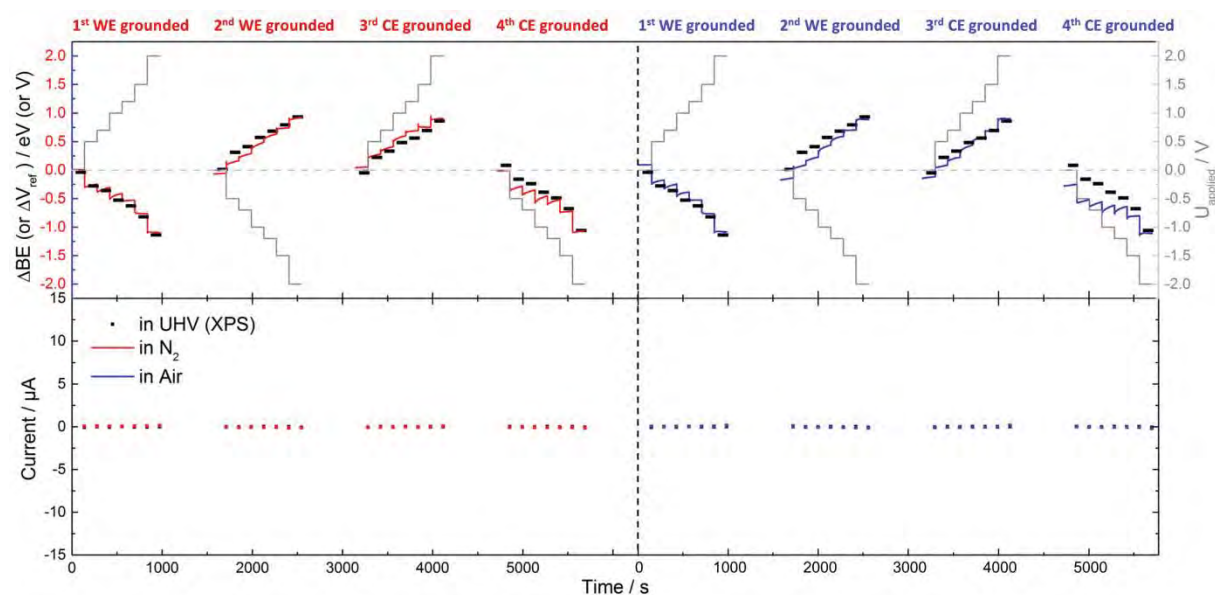
Figure A32 Top: Time-dependent measurement of PS curves of [C$_8$C$_1$Im][Tf$_2$N] with Au electrodes recorded in UHV by XPS (black), N$_2$ atmosphere (red) and air (blue). The applied voltage profiles are shown as grey traces. Bottom: Averaged current recorded during the measurements for [C$_8$C$_1$Im][Tf$_2$N] with Au electrodes.

[C$_8$C$_1$Im][Tf$_2$N] with 2 Pt electrodes
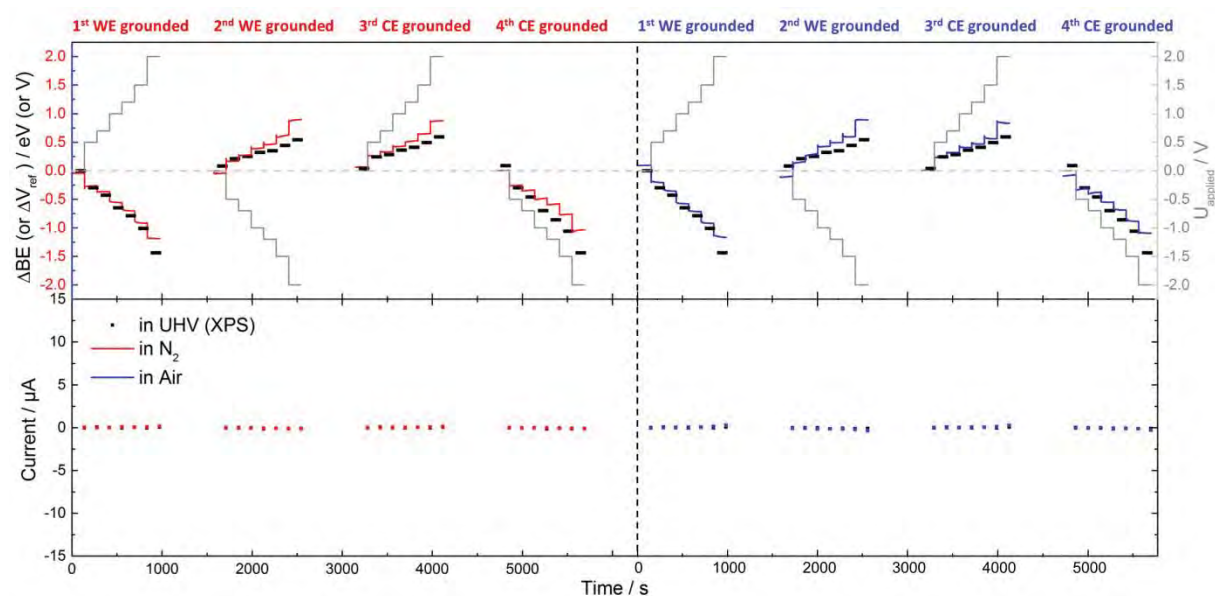
Figure A33 Top: Time-dependent measurement of PS curves of [C$_8$C$_1$Im][Tf$_2$N] with Pt electrodes recorded in UHV by XPS (black), N$_2$ atmosphere (red) and air (blue). The applied voltage profiles are shown as grey traces. Bottom: Averaged current recorded during the measurements for [C$_8$C$_1$Im][Tf$_2$N] with Pt electrodes.